TÉCNICO LISBOA

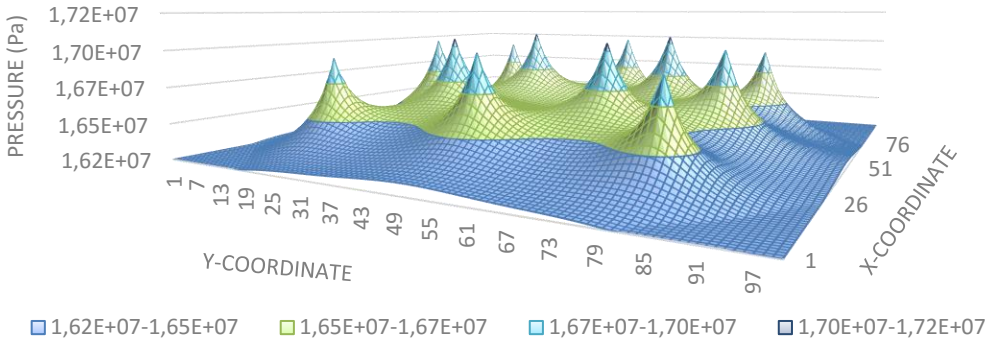

Modelling and Simulation of a Saline Aquifer for CO_2 Injection and Storage

Daniela Carla Moreira de Souza

Thesis to obtain the Master of Science Degree in

Chemical Engineering

Supervisors: Prof. Carla Isabel Costa Pinheiro
Di.-Ing. José Alfredo Ramos Plasencia

Examination Committee:

Chairperson: Prof. Sebastião Manuel Tavares da Silva Alves
Supervisors: Prof. Carla Isabel Costa Pinheiro
Di.-Ing. José Alfredo Ramos Plasencia
Members of the Commitee: Prof. Maria Cristina da Silva Fernandes

July 2016

Acknowledgments

This work was only possible with the collaboration of several people to whom I would like to express my sincere gratitude.

I'd like to start by thanking my parents and my sister, Sebastião, Luzia and Helen, for all the love and encouragement. To my mom, thank you so much for never ceasing to believe in me. Your uplifting spirit, constant motivation and all the sacrifices that you did for me got me where I am today.

I also like to acknowledge PSE for receiving me with open arms as an intern, providing me with all the tools to succeed in my objectives and for facilitating my stay in London. By participating on the gCCS project, I had the chance to get to know and learn from an incredibly bright group of people, an experience that I will forever hold dear to my heart and recall in my future endeavors. A special appreciation goes to my co-supervisor, Alfredo Ramos, and Adekola Lawal, for all your help, availability, guidance and patience.

I would also like to express my gratitude to my friends and roommates, Mario, Ricardo and Hugo. Thank you for all the help, motivation and, of course, for all the fun times. Being part of the pack made all the difference during my time in London.

I could never thank enough my supervisor, Carla Pinheiro, not only for accepting me as a graduate student but for being comprehensive, supportive and for helping me to persevere. You were present when I needed the most and If it wasn't for you, I would never have had the motivation and inspiration to arrive this far. As you once said to me: "Give me a place where I can stand and I shall move the world" (Arquimedes), you were truly the place where I stood. Thank you very very much!

Abstract

A promising method for reducing the impact of the global warming consists in capturing and sequestering the carbon dioxide (CO_2) into geological formations. Deep saline aquifers are great candidates for sequestration once they offer high storage capacities and worldwide distribution.

In the present work, a 2D Cartesian model of a Saline aquifer was developed in the gPROMS ModelBuilder, to provide a practical tool to study the feasibility of an aquifer for the CO_2 injection and its dynamic behaviour. The Aquifer model simulates the injection of a specified number of dense-phase CO_2 streams into its injection coordinates. The multiphase flow included the application of Darcy's law extension to each phase (CO_2 and water) and implementation of relative permeability correlations.

For validation, the results of simulations of the injection into Johansen formation, obtained the simulator ECLIPSE E100, were accessed. By applying the formation geological data to specify the developed model, results from simulations of two cases of relative permeability, deviate in only 0.18% and 0.24% from the values predicted by ECLIPSE, establishing the model validity. Furthermore, to test its applicability and sensitivity to the geological parameters, simulations were performed with sets of subsurface conditions of possible sequestration scenarios around the world, yielding quite realistic results.

Lastly, a Case Study of the Transmission and Injection sections of a new state of art power plant at Kingsnorth (UK) retrofitted with Carbon Capture and Storage (CCS) was performed. The simulation was successful and the project design constraints were met.

Keywords: saline aquifer, modelling, CO_2 injection, multiphase flow, gPROMS, CCS

Resumo

Um método promissor para reduzir o impacto do aquecimento global consiste na captura e sequestro geológico do dióxido de carbono (CO_2). Os aquíferos salinos são excelentes candidatos para o sequestro, sendo bem distribuídos mundialmente e oferecendo elevadas capacidades de armazenamento.

Neste trabalho, foi desenvolvido no gPROMS ModelBuider, um modelo cartesiano 2D x-y de um Aquífero Salino, uma ferramenta prática no estudo da viabilidade de um aquífero para a injeção de CO_2 e seu comportamento dinâmico. O modelo simula a injeção de um número discriminado de correntes de CO_2, nas correspondentes coordenadas. O fluxo multifásico é descrito por aplicação da extensão da Lei de Darcy à cada fase, CO_2 e água, e curvas de permeabilidade relativa.

Para validação, foram consultados resultados de simulações da injeção na formação Johansen, obtidos com o simulador ECLIPSE E100. Por aplicação de dados do modelo geológico e execução de simulações no modelo desenvolvido, resultados de dois casos de permeabilidade relativa estudados, apresentaram desvios de 0,18% e 0.24% em relação aos obtidos com o Eclipse, estabelecendo sua validade. A fim de testar a aplicabilidade do modelo e a sua sensibilidade aos parâmetros geológicos, foram realizadas simulações, com conjuntos de condições de subsolo de possíveis cenários de sequestro existentes no mundo, obtendo-se resultados bastante realistas.

Por último, realizou-se um case study das secções de Transmissão e Injeção de uma nova central energética em Kingsnorth (RU), adaptada com Captura e Armazenamento de Carbono (CCS). A simulação foi bem-sucedida e as restrições de design do projeto foram satisfeitas.

Keywords: aquífero salino, modelação, injeção do CO_2, fluxo multifásico, gPROMS, CCS

Contents

List of Figures

List of Tables

List of Symbols

Symbols

A	Area	m^2
f_A	Generic function/property	-
F	Mass flowrate	kg/s
$\vec{g}$	Vector of gravitational acceleration	m/s^2
G	Conserved scalar quantity	-
$\vec{H}$	Generic vector quantity	-
k	Intrinsic permeability tensor of the porous media	m^2
k_e	Effective permeability	m^2
k_e	Relative permeability	m^2
m	van Genuchten fitting parameter	-
M	Mass per unit volume	kg/m^3
$\vec{n}$	Outward-pointing vector normal to the surface	-
n	van Genuchten fitting parameter	-
p	Pressure in a fluid phase	Pa
P_b	Bubbling pressure	Pa
P_c	Capillary pressure	Pa
P_0	Strength coefficient (van Genuchten fitting parameter)	Pa
Q	Mass flowrate injected/extracted per unit volume	$kg/m^3 s$
S	Volumetric phase saturation	-
T	Temperature	K
u	Darcy's velocity	m/s
$\overrightarrow{u_s}$	Velocity of control volume $\Gamma_{n_{(t)}}$	m/s
V_b	Bulk volume of a rock	m^3
V_n	Control volume	m^3
V_p	Pore volume of a rock	m^3
x, y, z	Cartesian coordinates	-

Greek symbols

α	van Genuchten fitting parameter	-
λ	Pore-size index for Van Genuchten correlation	-
ϕ	Porosity, volume of void space per unit volume of porous medium	-
∇	Divergence operator	-
$\Gamma_{n_{(t)}}$	Moving element of surface area	m^2
ρ	Mass density	kg/m^3
θ	Dip angle between flow direction and a horizontal line	rad
μ	Dynamic viscosity	$Pa.s$

Subscripts

l	liquid-phase
g	gas-phase
β	Phase index

1. Introduction

The high amount of carbon dioxide (CO_2) released into the atmosphere during the 20th century has led to an increase in the global average temperature of around 0.77 ºC [1]. Analytical models predict that, without CO_2 sequestration, the temperature rise can go up to 4 ºC (Figure 1.1) [2].

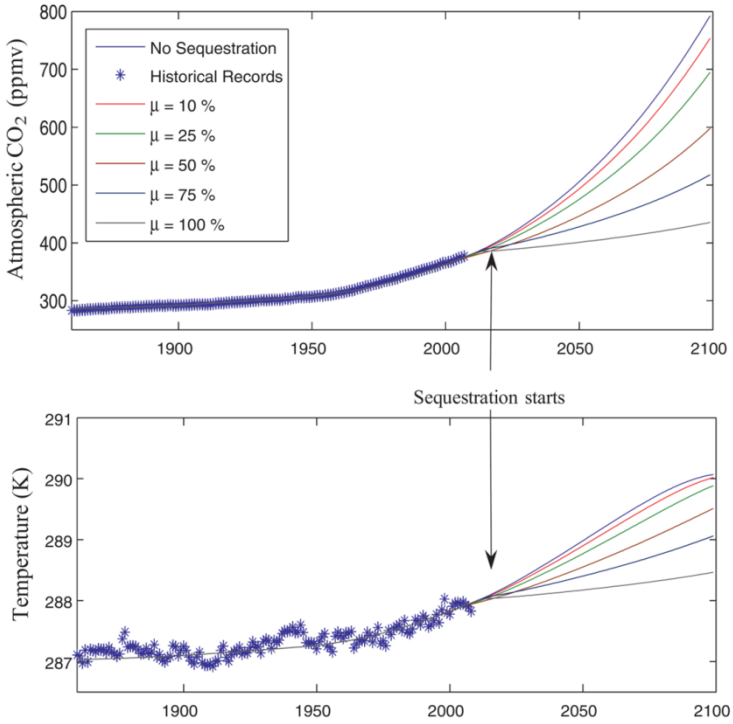

Figure 1.1 – Variations in the levels of atmospheric CO_2 (upper plot) and in the global temperatures (lower plot) obtained from the reduced order coupled analytical model for different rates of sequestration (μ) (after [2])

The mitigation options include the reduction of the energy intensity through efficiency and design improvements, reduction of the carbon intensity by switching to lower carbon content fuels, like natural gas, and to energy sources that operate with zero CO_2 emissions, such as renewable or nuclear energy and natural carbon sequestration, by enhancing the natural sinks for CO_2. It is unlikely that these methods would be sufficient to meet the commitments undertaken in 1997 Kyoto Protocol, thus, to meet the reduction targets, costlier mitigation approaches need to be considered, foremost among them being Carbon Capture and Storage (CCS) [3].

Carbon Capture and Storage consists on the capture of CO_2 emitted from fossil fuels combustion and industrial processes, the major stationary sources of CO_2, the transport to a storage location via ships or pipelines, and long-term isolation from the atmosphere by storing it in geological formations. It's been predicted that CCS will be responsible for 19% of the greenhouse gas reduction solution in 2050 - 9% for industry and transformation and 10% for power generation [4].

1.1. Motivation and objective

The evolution of the energy consumption by fuel type shows that the highest increase in world-wide energy consumption has been, and will continue to be, associated with fossil fuels: oil, coal and natural gas (Figure 1.2). The renewable energies are predicted to grow as well but in a much smaller scale. As for nuclear energy, its growth is expected to be only moderate.

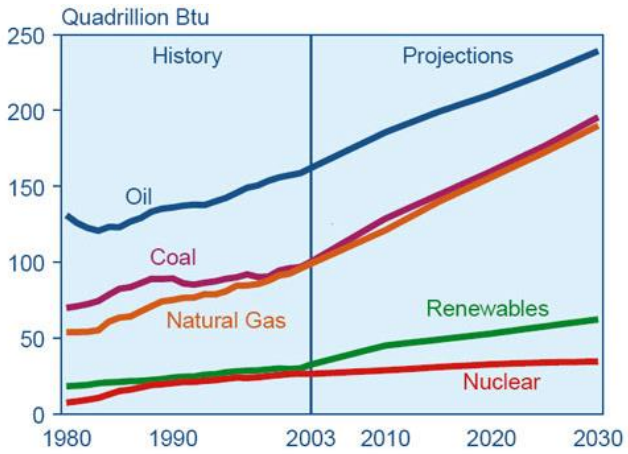

Figure 1.2 – World marketed Energy (1980 - 2030) (after [5])

The zero emission sources growth predictions imply that the use of fossil fuels for power generation and combustion in industrial processes would have to be continued. Nevertheless, with the growing concerns about global warming, the deployment of Carbon Capture and Storage is mandatory. With CCS, the CO_2 emissions are sequestered, being kept away from the atmosphere for hundreds or thousands of years. As a result, the need for restructuring the energy infrastructure and enhancing the security and stability of the energy systems is diminished [6].

The geological formations considered for sequestration comprise depleted oil and gas reservoirs, deep unmineable coal seams and saline aquifers (Figure 1.3). Among them, disposal in deep saline aquifers is highly favourable once they are wide distributed around the world, offers large storage volumes, and the pressure and temperatures regimes on these reservoirs favour the dense-phase injection of CO_2. Also, there is a possibility for enhanced storage through carbonate mineralization on the long term [3].

Hereupon, is possible to recognize that there is a great potential for sequestration of CO_2 into Saline aquifers but, before CCS could be implemented on a commercial scale, answers to safety and performance have to be found. Especially concerned with the acceleration of CCS development, its implementation and the management of the associated risk, the ETI CCS System Modelling Toolkit project was launched in 2011. The project is co-founded by the Energy Technologies Institute, ETI, and aims to create a commercially supported CCS modelling package, that enables the simulation of the operation and design of the whole CCS chain. Between the project participants are E.ON., Rolls-Royce, CO2DeepStore, E4Tech, and Process Systems Enterprise, PSE [7].

PSE represents the modelling expert, not only supplying the modelling platform, gPROMS advanced process modelling platform, but also assisting in the creation of the models and simulation of the operations along the chain [8].

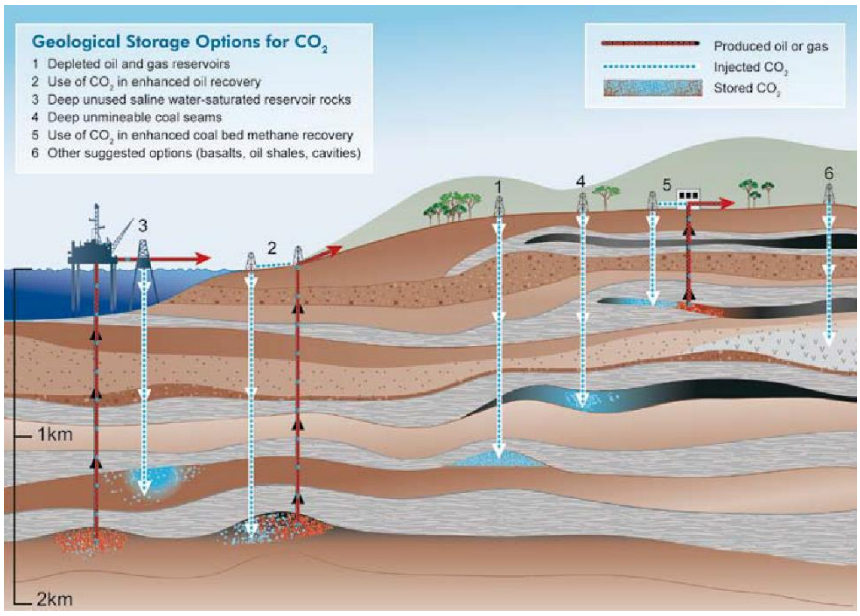

Figure 1.3 – Options available for CO_2 underground storage (after [9])

Taking the discussion above into consideration, a model to simulate the injection of CO_2 into Saline aquifers would constitute a great asset to the existing library of the gCCS modelling Toolkit. Large volumes of CO_2 are expected to be admitted at some aquifers, hence the injection being expected to be performed from more than one well on some projects. Therefore, a 2-Dimensional Cartesian Model of a Saline aquifer, where the carbon dioxide injected is able to migrate at the X and Y directions, will developed in this thesis, with the purpose of simulating the injection into such reservoirs, from a chosen number of wells, and monitoring the dynamic response of the system.

As the sequestering process takes place, the ease at which CO_2 can be injected diminishes. In order to attain a continuous mass flowrate injection, the pressure of the CO_2 stream that arrives at the aquifer from the accompanying CO_2 transport network, will have to increase during the project life. In that sense, another objective of this work will be to study the pressure development in aquifer.

The transport and injection network of CCS projects, i.e. the CO_2 sources and geologic reservoirs, may be spatially dispersed and have to be connected by means of a dedicated chain. The successful coupling of these networks is of upmost importance on deciding the viability of an Injection project, hence another objective of this thesis will be to study the coupling of the reservoir and the distribution network.

1.2. State of Art

Presently, there are many simulation codes that could be used to model injection of CO_2 into geologic formations. A critical comparison of these codes, presented by Class et al., can be found at [10], attesting their capability of simulating in quantitative and realistic detail, the flow and transport processes that would accompany geologic sequestration. Here, a brief overview of some of the compared models that have been applied in the context of CO_2 storage in geologic formation is presented:

COORES

IFP have developed a code in order to study the CO_2 storage processes from the well to the basin scale, the CO_2 Reservoir Environmental Simulator – COORES. To solve the molar conservation equations, a fully coupled system is linearized using a Newton approach. COORES can simulates the multi-component, three-phase and 3D fluid flow in heterogeneous porous media with a structured or unstructured grid.

ELSA

The code Estimating Leakage Semi-Analytically (ELSA) was developed at Princeton University. The code objective is uniquely addresses the challenge of providing quantitative estimates of fluid distribution and leakage rates in systems involving a sedimentary succession of multiple aquifers and aquitards, penetrated by an arbitrary number of abandoned wells. The modelling framework involves vertically integrated sharp-interface equations within each aquifer, coupled with local well models which consider full 3D flow in the well vicinity.

ECLIPSE

ECLIPSE is a simulation tool extensively used in the oil and gas industry. It comprises two software packages. The first, ECLIPSE Black Oil (E100), is a fully implicit, three-phase, 3D, general-purpose black oil simulator. The second, ECLIPSE Compositional (E300) is a compositional simulator with a cubic equation of state, pressure-dependent permeability values and black oil fluid treatment. Different incorporated speciation routines such as CO2STORE and GASWAT have been implemented in E300 research to handle CO_2 solubility in water and be applied to the geological sequestration problem.

TOUGH2

TOUGH stands for “Transport Of Unsaturated Groundwater and Heat”. It consists on a suite of software codes, developed at the Lawrence Berkeley National Laboratory (LBNL) in the early 1980s, focusing on geothermal reservoir engineering. From the family of multi-dimensional numerical models, TOUGH2 is the simulator used for the multi-phase flow of fluids and heat in porous and fractured media. When used together with the fluid property module "ECO2N", TOUGH2 is able to model the non-isothermal multiphase flow in the system H_2O - NaCl - CO_2, hence solve problems related to the CO2 sequestration in geological formations.

To describe non-isothermal multiphase flow in fractured porous media, a multi-phase approach is employed, accounting for the movement of gaseous and liquid phases, their transport of latent and sensible heat, and phase transitions between liquid and vapour. In TOUGH2, the fluid flow in both liquid and gaseous phases occur according to Darcy's law and the interference between the phases is represented by means of relative permeability functions. The code also accounts with heat transport, by conduction (with thermal conductivity dependent on water saturation), convection, and binary diffusion, which includes both sensible and latent heat [11].

The majority of the previous works in the reservoir modelling for CO_2 injection have been done employing TOUGH2 with the physical properties modelled with the equation of state package ECO_2 [12].

1.3. Structure of the thesis

The present thesis is organized in seven chapters. Chapter 2 offers a background review of the different aspects of the CCS chain, with a special focus on the Injection Section of the chain and the potential for the CO_2 geological sequestration in saline aquifers.

In chapter 3, the main governing equations underlying the multiphase flow in porous media are presented, as well as the description of the mathematical model of a Saline aquifer and the main assumptions and simplifications behind its implementation. Chapter 4 presents the implementation of the model on the gPROMS model builder platform and, on the 5th chapter, the developed model is tested and evaluated. Chapter 6 presents a case study scenario of the transport and injection section of a new state of art power plant retrofitted with CCS in Kingsnorth, UK.

On the 7th and final chapter, the main results and conclusions are introduced together with some thoughts on further work.

2. Background

2.1. Carbon Capture and Storage

CCS is an important part of the portfolio of decarbonisation options. The CCS chain can be decomposed in three essential stages: Capture, Transport and Storage.

2.1.1. Capture

The purpose of CO_2 capture is to obtain a concentrated stream from the combustion exhaust gas, so that it can be readily transported to a CO_2 storage site. As previously discussed, the main CO_2 emissions are originated from industrial processes on large centralized sources like power plants and large industries. Those represent the main target for CO_2 capture and storage ([13], [14]). As the largest contribution to CO_2 emissions has been associated with the burning of fossil fuel, particularly in electricity production, and the global tendency is not about to change (Figure 1.2), three capture processes has been developed to capture CO_2 from power plants that use coal or gas. These are:

- **Post-combustion capture**: In this process, the CO_2 is separated from the flue gas produced by combustion of a primary fuel (coal, natural gas, oil or biomass) in air (Figure 2.1);

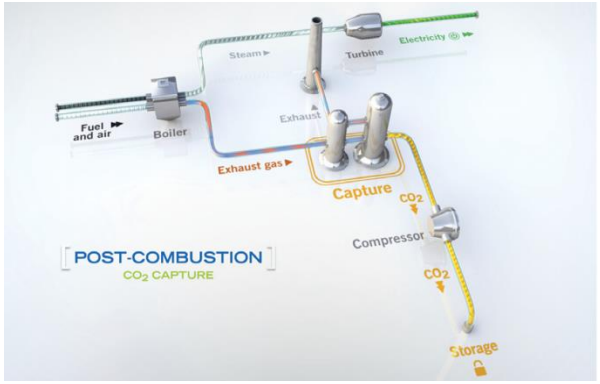

Figure 2.1 – Post- combustion Capture (after [15])

- **Pre-combustion capture**: In the pre-combustion systems, the primary fuel is firstly processed in a reactor to produce separate streams of CO_2 and H_2. The destiny of the CO_2 rich stream is capture and the H_2-rich stream is used as a fuel (Figure 2.2);

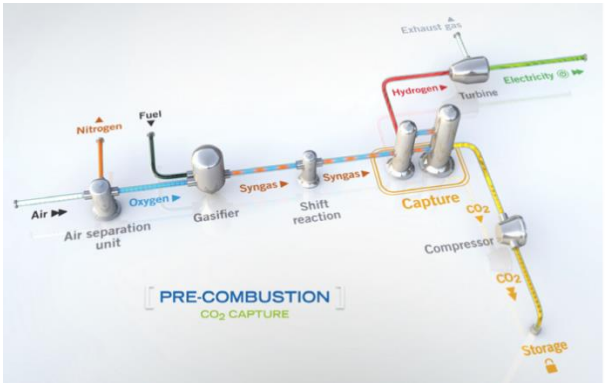

Figure 2.2 – Pre-combustion Capture (after [15])

- **Oxy-fuel:** This technology consists in the combustion of the fuel using oxygen instead of air. The flue gas produced is mainly composed by H_2O and CO_2, being readily captured (Figure 2.3)

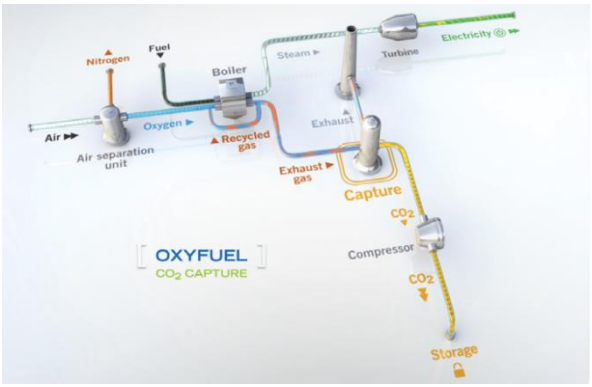

Figure 2.3 – Oxyfuel Combustion (after [15])

2.1.2. Transport

The transport stage links CO_2 sources and storage sites. After being captured, the CO_2 is compressed, making it easier to transport and store. Afterwards, it is transported to a suitable storage site. CO_2 has already been transported by pipeline, ship and by road tanker primarily for use in industry or to recover more oil and gas from oil and gas fields. Yet, the scale of transportation required for widespread deployment of CCS is far more significant than at present, and will demand the transportation of CO_2 in a dense phase [13].

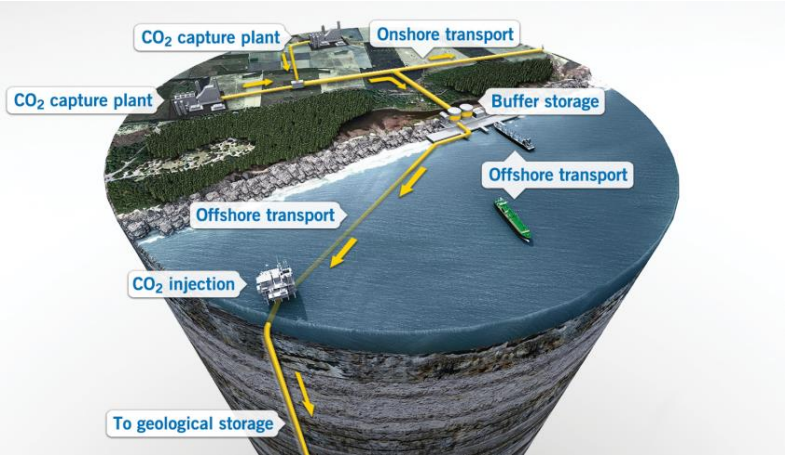

Figure 2.4 – Transport Stage Overview (after [16])

2.1.3. Injection and Storage

The final stage of CCS consists in the CO_2 injection into deep underground rock formations. A common characteristic to the appropriate storage sites is the presence of a very-low-permeability or impermeable rock such as shale or salt beds, known as a seal or cap rock, above them. The cap-rock and the trapping mechanisms prevent the CO_2 from returning to the surface.

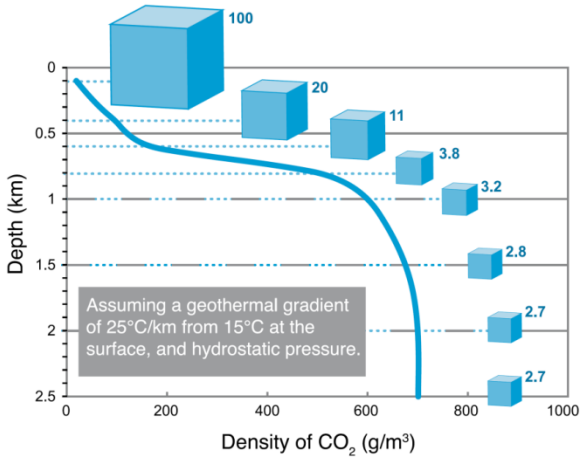

Figure 2.5 – CO_2 density variation with depth (after [9])

Depending on the rate that temperature increases with depth (geothermal gradient), the density of CO_2 will increase with depth, Figure 2.5. At depths of about 800 m or greater, CO_2 will be in a dense supercritical state the temperature and pressure keep it with a liquid-like density that enhances the efficiency of the utilization of underground storage [9].

When CO_2 is injected into a saline aquifer, it displaces saline formation water and then migrates buoyantly upwards, because it is less dense than the water. After injection, carbon dioxide can remain trapped underground by virtue of a number of mechanisms, such as: trapping the under the cap-rock; retention as an immobile phase trapped in the pore spaces of the storage formation; dissolution in the in situ formation fluids; and/or adsorption into organic matter in coal and shale. Additionally, it may be trapped by reacting with the minerals in the storage formation and cap-rock to produce carbonate minerals [9].

Ultimately, CO_2 becomes less mobile over time as a result of the trapping mechanisms discussed, further lowering the prospect of leakage and therefore increasing the storage security (Figure 2.6).

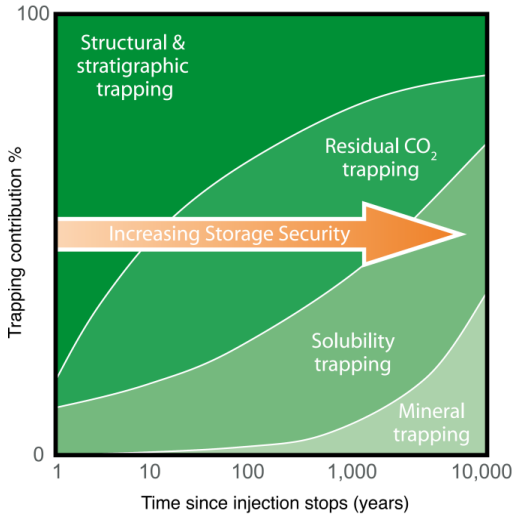

Figure 2.6 – Trapping mechanism and storage security (after [9])

Geological storage of CO_2 is in practice today beneath the North Sea, where nearly 1 Mton CO_2 has been successfully injected annually at Sleipner since 1996 and in Algeria at the In-Salah gas field.

Carbon dioxide has also been injected underground for Enhanced Oil Recovery (EOR). One such example is Weyburn Carbon Sequestration Project, in Saskatchewan, Canada.

Once CO_2 injection has taken place, a range of sensing and monitoring technologies are used to monitor the CO_2 movement and transformation within the rock formations. Monitoring, reporting and verification processes are important for the project performance management and to assure the public and regulators that the CO_2 is safely stored [13].

Ultimately, the cost of geological storage of CO_2 is highly site-specific, depending on factors such as the depth of the storage formation, the number of wells needed for injection and whether the project is onshore or offshore [9].

2.2. Characteristics of Reservoir rocks

The properties of the sedimentary rocks govern their physical and chemical properties, hence the fate of the carbon dioxide stored in them. Therefore, before describing the mathematical model formulation behind the simulation of the problem of CO_2 injection, the discussion of some of these properties is compulsory.

Sedimentary rocks are formed from accumulations of loose sand and muddy detritus, derived from breakdown of older rocks and brought together and sorted by water or wind. From hydrogeological point of view, these sedimentary rocks can be classified as three different types:

- **Aquifers,** into which water can be injected or from which water can be pumped such as sandstone and limestone**;**
- **Aquitards,** such as shales, into which water cannot be injected, but through which movement of water occurs over geological periods of time;
- **Aquicludes**, such as salt beds, that are barriers to water movement.

2.2.1. Porosity

The majority of rock and soils contains a certain percentage of empty spaces which may be occupied by fluids (liquids and/or gases). The ratio between the volume not occupied by solid framework and the bulk volume of a rock is a fundamental property the media recognized as porosity, $\emptyset\ (-)$:

$$\emptyset = \frac{V_p}{V_b} \tag{2.1}$$

where $V_p\ (m^3)$stands for the porous volume and $V_b\ (m^3)$,for the bulk volume of the rock. The porosity is a property of the rock measured in the absence of flow, static property. It is controlled by the variance of the local pore or the grain size distribution.

2.2.2. Permeability

Permeability is also a basic property of the reservoir rocks, measuring their capacity and ability to transmit fluids. It depends on the interconnection between the pores, being strongly influenced by the shape and size of the grains, their organization and the texture of the rock. Unlike porosity, the permeability can only be defined together with the fluid flow, by means of the Darcy's law. While studying

the flow of water through sand filters for purification, Darcy discovered that the fluid flow was directly proportional to the hydraulic gradient. For a simple case of a horizontally oriented rock core subjected to a pressure gradient, the mass flowrate, $F(kg/s)$, will be given by [17]:

$$F = -kA\frac{\rho}{\mu}\frac{dP}{dx} \tag{2.2}$$

with A representing the cross section perpendicular to the flow, $\mu(Pa.s)$ and $\rho(kg/m^3)$ the viscosity and mass density of the fluid occupying the porous space, respectively. dP/dx is the pressure gradient and $k(m^2)$, the intrinsic permeability of the rock, a measure of its ability to conduct the fluid when completely saturated with that fluid.

In the multiphase flow in the subsurface, different phases exist and occupy the pore space at the same time. For a given phase, the presence of the other reduces the flow path. Therefore, another concept has to be introduced, the permeability of a rock to one fluid when only partially saturated, known as phase or effective permeability, $k_e(m^2)$.

The fractional flow of each fluid is determined by its relative permeability, $k_r(-)$**,** the ratio between the effective permeability to a specific fluid divided by some base permeability, usually the absolute or intrinsic permeability. It constitutes a direct measure of the ability of the porous system to conduct one fluid when one or more fluids are present:

$$k_r = \frac{k_e}{k} \tag{2.3}$$

The flow velocity, $\vec{u}\ (m/s)$, is given by the multiphase extension of Darcy's law, evaluated for each phase separately:

$$\overrightarrow{u_\beta} = -k\frac{k_{r\beta}}{\mu_\beta}\left(\vec{\nabla}P_\beta - \rho_\beta\vec{g}\right) \tag{2.4}$$

with k_{r_β} representing the relative permeability of the phase β and $P_\beta(Pa)$ its pressure. Further $\vec{g}$ is the vector of gravitational acceleration.

These flow properties are the composite effect of pore geometry, wettability, fluid distribution, and the fluid saturation of phase β, $S_\beta(-)$, i.e. the ratio between the pore volume occupied by the phase $\beta$and the pore volume available for flow [18].

2.2.3. Rock wettability and capillary pressure

Wettability can be defined as the tendency of one fluid to spread on or to adhere to a solid surface in the presence of other immiscible fluids. Applying this term to CO_2 injection problem, the solid term is the reservoir rock and the fluids are water and CO_2 rich phases, the wetting and non-wetting phases, respectively.

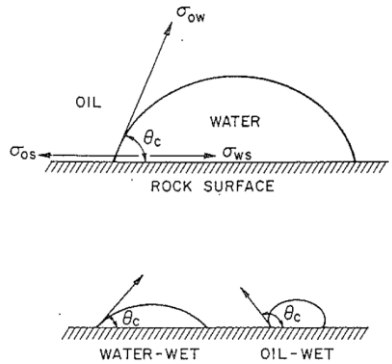

Figure 2.7 – Rock wettability (after [18])

Between two fluids in contact with each other, there is a free interfacial energy, created by the different forces which attract the molecules toward the interior of each phase and those which attract them through the contact surface. The interfacial energy is characterized by the interfacial tension, σ_{ik}, defined as the amount of work needed to separate a surface of unit area of the substances i and k [17]. That's the phenomenon responsible for the water rise in the capillary tube.

The capillary pressure in porous media can be defined as the pressure difference existing across the interface separating two immiscible fluids, one of which wets the surfaces of the rock in preference to another. It is generally expressed as the pressure in the non-wetting phase minus the pressure in the wetting phase. In this case, it will be given by:

$$P_c = P_{CO2} - P_{water} \tag{2.5}$$

In the context of reservoir simulation, P_c reflects the interaction of rock and fluids, being controlled by the pore geometry, interfacial tension and wettability, a basic input for simulation studies [19].

2.2.4. Fluid distribution

The distribution of the wetting and non-wetting phases within the pore spaces do not depend only on the phases saturations but also upon the direction of the saturation change. The term hysteresis is applied to the difference in multiphase rock properties that depends on the direction of saturation change. This direction of saturation change is designated by drainage if the flow results in a decrease in the wetting phase saturation, and imbibition if the flow originate an increase in the wetting phase saturation. In the case of CO_2 injection, the non-wetting phase, CO_2 rich phase, is displacing a wetting-phase, water rich phase, constituting a drainage problem [19].

Furthermore, as the fluid distribution depends on the direction of saturation change so does the capillary pressure. Since the wettability and direction of saturation influence the fluid distribution, it is expected that these factors affect the capillary and relative permeability characteristics similarly.

2.3. Two phase characteristic curves

The constitutive relationships used for the capillary pressure and for the relative permeabilities are necessary to describe the processes that occur during the carbon dioxide injection into geological

formations. There are a number of two phase characteristic curves relating capillary pressure and phase saturation to solve for capillary pressure and relative permeability numerically from two-phase flow experiments. From these characteristic curves, Brooks and Corey ([20], [21] and [22]) and van Genuchten [23] are the most widely assumed in reservoir simulations.

2.3.1. van Genuchten

The van Genuchten curves [23] are the most used set of two-phase characteristic curves. The capillary pressure relationship is given by:

$$P_c = \frac{1}{\alpha}\left[{S_e}^{-1/m} - 1\right]^{1/n} \tag{2.6}$$

where n, α and $m = 1 - (1/n)$ are dimensionless van Genuchten fitting parameters. $S_e(-)$ constitutes the effective phase saturation or:

$$S_e = \frac{S_l - S_{lr}}{1 - S_{lr}} \tag{2.7}$$

where $S_{lr}(-)$ is the residual wetting phase saturation, i.e. the volume of that fluid that is trapped and not available to flow at the porous media.

The relative permeability of the liquid-phase can be predicted from the capillary pressure curve expression using the integral expressions of Mualem [24] or Burdine [25]. For Mualem, the solution for the liquid-phase relative permeability is given by:

$$k_{rl} = {S_e}^{1/2}\left(1 - \left(1 - {S_e}^{1/m}\right)^m\right)^2 \tag{2.8}$$

Parker et al. [26] extended the van Genuchten–Mualem characteristic curves to include the gas-phase relative permeability, or:

$$k_{rg} = (1 - S_e)^{1/2}\left(1 - {S_e}^{1/m}\right)^{2m} \tag{2.9}$$

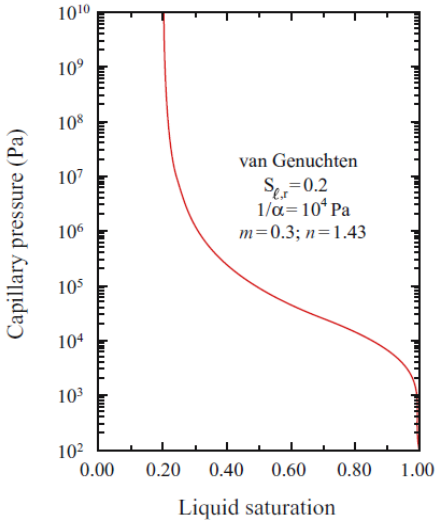

Figure 2.8 – van Genuchten Capillary pressure curves (after [27])

Figure 2.8 show some a generic van Genuchten–Mualem two-phase characteristic curves for some capillary pressure curve, it exhibits unphysical behaviour as the liquid saturation diminishes (gas

saturation increases). For 100% liquid saturation, the capillary pressure is negligible but, as we move towards the liquid residual value ($S_{lr} = 0.2$ in this case), the value of capillary pressure goes to infinity.

For the liquid relative permeability curve, it starts at low values and increases dramatically with increasing liquid saturation and, for the gas-phase curve, it decreases with increasing liquid saturation and is concave down (Figure 2.9).

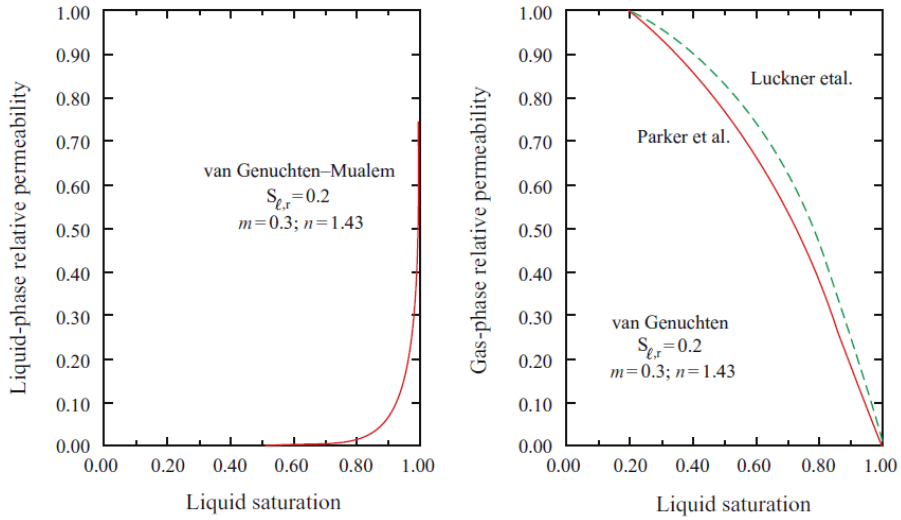

Figure 2.9 – van Genuchten relative permeability curves (after [27])

2.3.2. Brooks and Corey

Brooks and Corey ([20] and [21]) developed another popular set of two-phase characteristic curves. Based on experimental observations, they noticed that the effective saturation is a linear function of capillary pressure on a log-log plot:

$$P_c = \frac{P_b}{S_e^{1/\lambda}} \tag{2.10}$$

where P_b is the bubbling pressure, the extrapolated capillary pressure at full liquid saturation, S_e is the effective saturation (same as van Genuchten expression) and λ is the pore-size index.

Corey used the Burdine [25] theory to derive expressions for the wetting (liquid) and non-wetting (gas) phases [22]:

$$k_{rl} = S_e^{\,4} \tag{2.11}$$

$$k_{rg} = (1 - S_e)^2\left(1 - S_e^{\,2}\right) \tag{2.12}$$

It's important to pinpoint that the Brooks and Corey capillary pressure does not go to zero as the liquid saturation goes to 1.0 because the straight-line fit does not fit the data in this region (Pc < Pb) (Figure 2.10). In contrast, the van Genuchten capillary pressure curve do go to zero as the liquid saturation approaches the unity (Figure 2.8). This behaviour at high liquid saturations is the reason why the van Genuchten capillary pressure characteristic curves are more used than the Brooks and Corey formulation.

The liquid relative permeability curve starts at low values and increases dramatically with increasing liquid saturation and, for the gas-phase, there is a decreases with increasing liquid saturation, being convex (Figure 2.11).

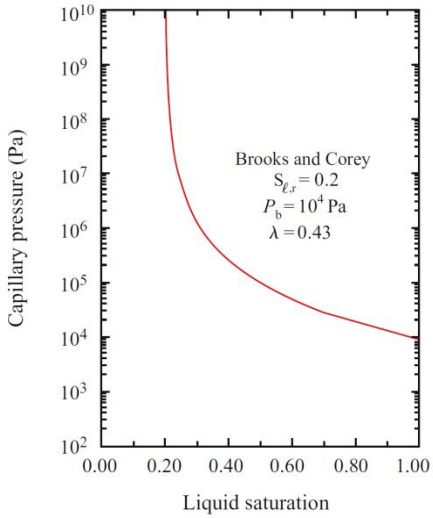

Figure 2.10 – Corey's capillary pressure curves (after [27])

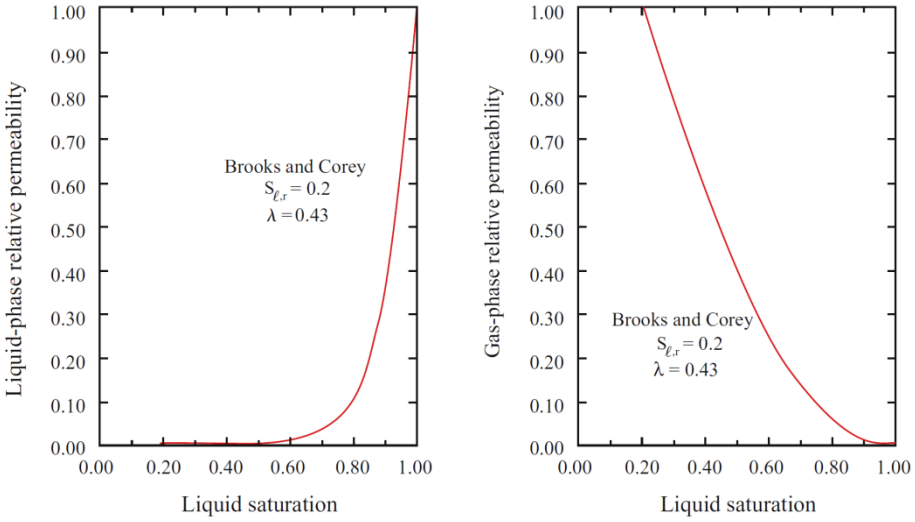

Figure 2.11 – Corey's Relative permeability curves (after [27])

3. Mathematical modelling of a saline aquifer

The saline aquifer reservoir will be modeled by means of mathematical equations. Their main purpose is to represent and predict the physical behavior of the reservoir. Here, the mathematical description of the injection problem will be introduced, together with the assumptions and simplifications behind the implementation.

3.1. Governing equations

The fundamental principle behind the description of flow in a porous medium is the conservation of mass. The motion of fluid causes a change in the amount of its components present at any location with varying compositions through the porous medium. For that reason, the first topic to be approached is the description of the flow mechanisms that may contribute to the transport of each component.

The main physical mechanisms that can come into play in the transport are:

- **convection** or advection, phenomenon in which dissolved components are carried along by the movement of fluid displacement;
- **diffusion**, physical phenomenon linked to the random motions of molecules that act to reduce any sharp concentration gradients that may exist;
- **dispersion**, mixing phenomenon linked to small-scale random variations in flow velocity inside the porous media that cause sharp fronts to spread.

By reviewing the CO_2 trapping mechanisms and their impact on the storage security (Figure 2.6), one can perceive that the Structural and Stratigraphic trapping and the Residual trapping are the dominant mechanisms after the injection stops. Thus, the effect of chemical reactions, adsorption will not be included in the considered model, the chemical partitioning between water and CO_2 in the interface between the phases will be neglected and the concentration of each phase kept constant.

Two fluid phases are considered, an aqueous or water-rich phase, referred to as liquid-phase and a single CO_2-rich phase, referred to as gas-phase. Consequently, the flow mechanism of transport will consist on the multiphase immiscible flow of the liquid- and gas-phases in the porous media, being governed by convection.

For an arbitrary volume V_n of the porous media, bounded by a surface Γ_n, the material balance to the resident phases is given by [28]:

Rate of mass change of phase $\boldsymbol{\beta}$ *in* $\boldsymbol{V_n}$	=	*Net rate of mass inflow of phase* $\boldsymbol{\beta}$ *into* $\boldsymbol{V_n}$	+	*Mass rate of phase* $\boldsymbol{\beta}$ *injected into* $\boldsymbol{V_n}$	−	*Mass rate of phase* $\boldsymbol{\beta}$ *extracted from* $\boldsymbol{V_n}$

Thus, the rate at which the mass of phase β changes in V_n is balanced by its net inflow by convection, and the inflow and outflow arising from injection and extraction processes, respectively.

3.1.1. Accumulation term

The mass of phase β contained in a differential element of volume dV_n, M_β, will be expressed by:

$$M_\beta = \phi \rho_\beta S_\beta dV_n \tag{3.1}$$

where ϕ stands for the porosity of the volume, ρ_β for the mass density of phase β and S_β for the volume saturation of phase β.

The integration of (3.1) gives the total mass of the phase β contained in the control volume V_n:

$$Mass\ of\ phase\ \beta\ in\ V_n = \int_{V_n} \phi \rho_\beta S_\beta dV_n \tag{3.2}$$

Accordingly, the rate of change in the amount of phase β contained in V_n, accumulation term, is given by:

$$Rate\ of\ change\ of\ mass\ of\ phase\ \beta\ in\ V_n = \frac{d}{dt} \int_{V_n} \phi \rho_\beta S_\beta dV_n \tag{3.3}$$

3.1.2. Flux term

Part of the accumulation of phase β in V_n is due to its transport in and out of the control volume. At any differential element of area $d\Gamma$, the convective flux of phase β, $\overrightarrow{J_\beta}$, is given by:

$$Advective\ flow\ of\ phase\ \beta = \overrightarrow{J_\beta} = \rho_\beta \overrightarrow{u_\beta} \tag{3.4}$$

where ρ_β is the mass per unit volume of the phase β and $\overrightarrow{u_\beta}$ it's the Darcy's velocity.

Since the flux vector may not be normal to the surface Γ_n, the component of the flow crossing the element of surface is given by:

$$Mass\ flux\ of\ phase\ \beta = -\vec{n} \cdot \overrightarrow{J_\beta} d\Gamma_n \tag{3.5}$$

where $\vec{n}$ is the outward-pointing vector normal to the surface at the location of the differential element of area, $d\Gamma_n$. The negative sign gives positive accumulation for flow in the opposite direction of the normal vector, meaning flow into the control volume.

The net rate of convective inflow is obtained by the integration of the rate over the full surface, Γ_n:

$$Net\ rate\ of\ inflow\ of\ phase\ \beta\ into\ V_n = -\int_{\Gamma_n} \vec{n} \cdot \overrightarrow{J_\beta} d\Gamma_n \tag{3.6}$$

3.1.3. Injection/ Extraction terms

The main purpose of the injection and extraction terms will to describe the flow of carbon dioxide into the aquifer. Here, this term will be modeled as if there were a creation of mass in a differential element of volume dV_n, i.e. as a source term.

$$Mass\ of\ phase\ \beta\ injected\ into\ V_n = \int_{V_n} Q_{\beta_{injected}} dV_n \tag{3.7}$$

The main purpose of the reservoir model is to simulate the injection of CO_2 into saline aquifers but, by modelling the sink and source terms, applications to different kinds of flow problems could become attainable. Although the study of the extraction goes beyond the purpose of this thesis, as discussed at 1.1, this term will be modelled, as a sink term.

$$Mass\ of\ phase\ \beta\ extracted\ from\ V_n = -\int_{V_n} Q_{\beta_{extracted}} dV_n \tag{3.8}$$

3.1.4. Continuity equation

The approach followed to model the proposed saline aquifer is in agreement with the formulation of the TOUGH codes ([28] [12] [29]). The combination of the terms accumulation, convection, injection and extraction yields an integral material balance for the phase β. For an arbitrary control volume, the material balance comes:

$$\frac{d}{dt}\int_{V_n} M_\beta dV_n = -\int_{\Gamma_n} \overrightarrow{J_\beta}.\vec{n} d\Gamma_n + \int_{V_n} \left(Q_{\beta_{injected}} - Q_{\beta_{extracted}}\right) dV_n \tag{3.9}$$

To understand the spatial distribution of phase β, the continuity equation will be derived. The Reynolds transport theorem states that, for a scalar quantity G that is conserved, in a control volume $V_{(t)}$ that moves with a velocity $\overrightarrow{u_s}$:

$$\frac{d}{dt}\int_{V_{(t)}} G dV_n = \int_{V_{(t)}} \frac{\partial G}{\partial t} dV_n + \int_{\Gamma_{n_{(t)}}} \vec{n}.\overrightarrow{u_s} G d\Gamma_n \tag{3.10}$$

the total rate of change of G in $V_{(t)}$is equal to the summation of the change due to the local rate of change of G (first term on the right side) and the rate of change associated with the surface $\Gamma_{n_{(t)}}$ overtaking G as it moves (second term on the right side). Assuming a stationary control volume, $\overrightarrow{u_s} = 0$, and applying the theorem to the equation (3.9) we arrive to:

$$\int_{V_n} \frac{\partial M_\beta}{\partial t} dV_n = -\int_{\Gamma_n} \overrightarrow{J_\beta}.\vec{n} d\Gamma_n + \int_{V_n} \left(Q_{\beta_{injected}} - Q_{\beta_{extracted}}\right) dV_n \tag{3.11}$$

For a vector quantity $\vec{H}$, the divergence theorem states:

$$\int_{V_n} \vec{\nabla}.\vec{H} dV_n = \int_{\Gamma_n} \vec{n}.\vec{H} d\Gamma \tag{3.12}$$

Applying the divergence theorem to the equation (3.11), the following equation is obtained:

$$\int_{V_n}\left[\frac{\partial M_\beta}{\partial t}dV_n + \vec{\nabla}.\overrightarrow{J_\beta}dV_n + \left(Q_{\beta_{injected}} - Q_{\beta_{extracted}}\right)dV_n\right] = 0 \quad (3.13)$$

If the integral in equation (3.13) is to be zero for any choice of the control volume, its integrand must be identically zero everywhere. As previously discussed, the injection term will be translated as a source, given by the mass flowrate of the CO_2 that leaves the coupled transport system for sequestration, $q_{\beta_{injected}}$. The final form of the continuity equation that will be applied at this model implementation is obtained:

$$\frac{\partial \phi \rho_\beta S_\beta}{\partial t} + \vec{\nabla}.\left(\rho_\beta \overrightarrow{u_\beta}\right) + \left(F_{\beta_{injected}} - F_{\beta_{extracted}}\right) = 0 \quad (3.14)$$

3.1.5. Closure relations

In order to completely specify the flow problem and solve the system of balance equations, a sufficient number of relations have to be provided, so that all unknowns can be determined. This closure will be accomplished by the following additional functions, relations and equations of state (EOS).

Gas-phase density

$$\rho_{GAS} = f(P\ , T) \quad (3.15)$$

Liquid-phase density

$$\rho_{LIQUID} = f(P\ , T) \quad (3.16)$$

Gas-phase viscosity:

$$\mu_{GAS} = f(P\ , T) \quad (3.17)$$

Liquid-phase viscosity:

$$\mu_{LIQUID} = f(P\ , T) \quad (3.18)$$

Gas-phase relative permeability:

$$k_{r_g} = f(S_l) \quad (3.19)$$

Liquid-phase relative permeability:

$$k_{r_l} = f(S_l) \quad (3.20)$$

Capillary pressure:

$$P_C \ = P_g - P_l = f(S_l) \quad (3.21)$$

Phase saturations summation equal to unit:

$$\sum S_\beta = 1 \quad (3.22)$$

3.2. Model Implementation method

Equation (3.9) is used as the starting point to derive the finite differences and the integral finite difference (IFD) method by Narasimhan and Witherspoon will be employed to discretize the mass balance [30]. The volume integrals are therefore approximated by a volume average:

$$\int_{V_n} M_\beta dV = V_n M_{\beta n} \tag{3.23}$$

where $M_{\beta n}$ represent the average value of M_β over V_n.

The surface integrals are given by the discrete sum of averages over the surface elements surrounding the volume element. For two consecutive grid elements n and m, they are given by:

$$\int_{\Gamma_n} \overrightarrow{J_\beta}.\vec{n}d\Gamma = \sum_m j_{nm}A_{nm} \tag{3.24}$$

where A_{nm} correspond to the surface area between the grid elements n and m. j_{nm} is the average value of the (inward) normal component of $\overrightarrow{J_\beta}$ over A_{nm}.

According to the geometry adopted to describe the system, with appropriate volume and surface area averages taken in equation (3.9), a set of first-order ordinary differential equations in time will be obtained:

$$\frac{\partial M_\beta}{\partial t} = \frac{1}{V_n}\sum_m {j_\beta}_{nm}A_{nm} + +{F_\beta}_{injected_{(n)}} - {F_\beta}_{extractied_{(n)}} \tag{3.25}$$

The individual phase fluxes terms, ${j_\beta}_{nm}$, will be given in terms of average variables or parameters, represented here by the subscripts nm. These quantities are evaluated at the interface between consecutive volume elements V_n and V_m using a suitable averaging technique.

When modelling the multiphase flow in composite (layered) media, discontinuous permeability changes can occur at the boundaries between different units. For single-phase flow, the appropriate interface weighting scheme for absolute permeability is harmonic weighting. For two-phase flow, the problem of relative permeability weighting arises. It has been established that, for transient flow problems in homogeneous media, relative permeability must be upstream weighted, otherwise the phase fronts may be propagated with erroneous speed [31]. Studies at the Lawrence Berkeley National Laboratory have shown that, for transient two-phase problems in composite media, both absolute and relative permeability must be fully upstream weighted to avoid the possibility of gross errors [29]. They have also concluded that there is no single averaging technique. Although the study of the weighing technique influence on the flow goes beyond the scope of this thesis work, its value is recognized by implementing harmonic, logarithm and arithmetic weighting options.

The finite difference approximation of the basic Darcy flux, representative of the advective flux is given by:

$${j_\beta}_{nm} = -{\rho_\beta}_{nm}k_{nm}\left[\frac{k_{r\beta}}{\mu_\beta}\right]_{nm}\left[\frac{{P_\beta}_n - {P_\beta}_m}{D_{nm}} - {\rho_\beta}_{nm}g\,sin(\theta)\right] \tag{3.26}$$

where D_{nm} is the distance between the points where the pressure is evaluated, g represents the component of gravitational acceleration in the direction from m to n, and θ is the dip angle measured between flow direction and a horizontal line.

The gPROMS ModelBuilder is used for the implementation of the model and the accumulation of mass will be evaluated recurring to the explicit time derivatives. The reservoir will be modelled in Cartesian coordinates, with the flow calculated in the interface between the grid elements in the x-

direction and y-direction. The user has the freedom to specify the number of elements composing the geological grid but it's important to denote that this number will be limited by the computational effort.

4. Model Implementation at gPROMS

4.1. Model description

Model type: dynamic

The aquifer model is a dynamic model that aims to describe the pressure changes experienced by a saline aquifer when it's subjected to an injection of CO_2. The number of inlet streams is a dynamic variable describing the injection terms.

4.1.1. Inlets

- A dynamic number of CapturedCO2 inlet ports representing the connection with injection wells.

4.1.2. Outlets

- Not applicable.

4.1.3. Degrees of freedom

A degree of freedom analysis showed that the following specifications are required:

- Inlet streams conditions (T, F, w).

4.1.4. Initial Conditions

The user will have to provide as many initial conditions as the number of differential equations. The variables to be assigned initial values will be:

- Initial pressure of reservoir;
- Initial volume saturation of liquid-phase.

4.2. Model Specification Dialog

The following options will be available in the model Specification Dialog:

4.2.1. Specification Mode: Standard

Option	Choices
Specification mode	Advanced, Standard

«

4.2.2. Specification Mode: Advanced

Option	Choices
Injection Flowrate	Specified, Not specified
Physical properties calculation	Multiflash, Literature correlation
Directional Permeability	Isotropic, Anisotropic
Media deformability	Inactive, Pressure dependant
Capillary Pressure	Negligible, van Genuchten correlation
Relative permeability correlation	Corey, van Genuchten, Continuous fitted Corey Linear relation
Interface averaging	Harmonic mean, Arithmetic mean, Logarithmic mean

4.3. Model assumptions

The aquifer model comprehends some simplifications in its formulation. One of them consists in considering it isothermal as its large volume is filled with water previous to injection. Inertial, gravitational, and non-isothermal effects are also neglected. The reservoir will be modelled in Cartesian coordinates and the flow geometry is assumed to be 2-D, in the x and y-axis direction. As the reservoir thickness will be quite small compared to its extension, the pressure gradient in the z-direction will be neglected.

Another important assumption is the homogeneity of the reservoir. The permeability will be, by default, equal in the x and y-direction of flow.

4.4. Nomenclature

Here we present the nomenclature used in the gPROMS implementation.

Table 4.1 – gPROMS model Parameters nomenclature

Symbol	gPROMS name	Definition	Units	Array size
β	Phase	Phase ordered set	-	N_{phases}
C	Components	Component ordered set	-	$N_{components}$
gas_prop	gas_prop	Gas physical properties package	-	-
liquid_prop	liquid_prop	Liquid physical properties package	-	-
$t_{simulation}$	simulation_time_units_in_s	Simulation time unit in seconds	s	-
θ	Alfa	Dip angle between flow direction and horizontal line	rad	-
N_x	no_elements_xdir	Number of discrete elements in x-direction	-	-
N_y	no_elements_ydir	Number of discrete elements in y-direction	-	-
N_{wells}	no_wells	Number of wells	-	-
$well^{flag}$	well_flag	Flag for the presence of well x-coordinate on the (x, y) grid element	-	(N_x, N_y)

Symbol	gPROMS name	Definition	Units	Array size
x_{well}^{flag}	x_well_flag	Flag for the presence of well in x-coordinated element of grid	-	(N_x)
y_{well}^{flag}	y_well_flag	Flag for the presence of well in y-coordinated element of grid	-	(N_y)
x_{well}	x_position_well	Well x-coordinates	-	N_{wells}
y_{well}	y_position_well	Well x-coordinates	-	N_{wells}
$F_{liquid_{in}}$	F_water_in	Injection flowrate of water	kg/s	-
$F_{gas_{out}}$	F_CO2_out	Extraction flowrate of CO2	kg/s	-
$F_{liquid_{out}}$	F_water_out	Extraction flowrate of water	kg/s	-
k	k0	Intrinsic permeability of porous media	m^2	(N_x, N_y)
k_{well}	k_well	Permeability of the discrete element containing well	m^2	-
k_{0x}	k0x	Permeability of porous media in x-direction	m^2	(N_x, N_y)
k_{0y}	k0y	Permeability of porous media in y-direction	m^2	(N_x, N_y)
c_R	pore_compressibility	Compressibility factor of porous media	Pa^{-1}	-
δ	small_positive_number	Small positive number for numerical stability	-	-
$t_{injection}$	injection_time_in_years	Injection time	years	-
m	m	van Genuchten relative permeability correlation parameter	-	-
S_{lr}	Sgr	Irreducible gas saturation	-	-
S_{gr}	Slr	Irreducible liquid saturation	-	-
S_0	S0	Initial liquid-phase volume saturation	-	(N_x, N_y)
P_0	Po	van Genuchten capillary pressure correlation parameter	Pa	-
λ	Lambda	van Genuchten capillary pressure correlation parameter	-	-
f_{tgh}	f_tgh	parameter for function smoothing	-	-
S_{tgh}	S_tgh	parameter for function smoothing	-	-
Z_{up}	z_domain_boundary_up	Upper boundary	m	-
Z_{down}	z_domain_boundary_down	Lower boundary	m	-
X_{east}	x_domain_boundary_east	East boundary	m	-
X_{west}	x_domain_boundary_west	West boundary	m	-
Y_{north}	y_domain_boundary_north	North boundary	m	-
Y_{south}	y_domain_boundary_south	South boundary	m	-
$well_{\text{radius}}$	well_radius	Thickness of discrete element containing well	m	-
$L_{y\ aquifer}$	y_extension	Reservoir extension in y-direction	m	-
$L_{x\ aquifer}$	x_extension	Reservoir extension in x-direction	m	-

Symbol	gPROMS name	Definition	Units	Array size
$H_{aquifer}$	aquifer_thickness	Vertical thickness of aquifer	-	-
p_0	p0	Initial pressure	-	-
T_0	T0	Initial temperature	-	-
ϕ_0	Porosity0	Initial value of porosity (void fraction)	-	(N_x, N_y)

Table 4.2 – gPROMS model Variables Nomenclature

Symbol	gPROMS name	Definition	Units	Array size
w	w	Mass fraction of components on the (x, y) grid element	-	$(N_{components}, N_x, N_y)$
h_{source}	h_source	Inlet specific enthalpy	J/kg	N_{wells}
p_β	p_phase	Pressure of phase β on the (x, y) grid element	Pa	(N_{phases}, N_x, N_y)
p_{cap}	p_capillary	Capillary pressure on the (x, y) grid element	Pa	(N_x, N_y)
T	Temperature	Temperature on the (x, y) grid element	K	(N_x, N_y)
T_{source}	T_source	Temperature of inlet streams	K	N_{wells}
$w_{injection}$	w_injection	Mass fraction of inlet streams on the (x, y) grid element	-	$(N_{components}, N_{wells}, N_x, N_y)$
S_β	S	Volume saturation of phase β on the (x, y) grid element	-	(N_{phases}, N_x, N_y)
$S_{r\ \beta}$	Sr	Effective saturation of phase β for relative permeability calculation on the (x, y) grid element	-	(N_{phases}, N_x, N_y)
g	g	Gravity acceleration	$kg\ m\ s^{-2}$	-
k_{xx}	k_xx	Average permeability between consecutive grid elements in the x-direction of flow	m^2	$(N_x - 1, N_y)$
k_{yy}	k_yy	Average permeability between consecutive grid elements in the y-direction of flow	m^2	$(N_x, N_y - 1)$
ρ_β	rho	Density of phase β on the (x, y) grid element	kg/m^3	(N_{phases}, N_x, N_y)
μ_β	miu	Viscosity of phase β on the (x, y) grid element	$Pa\ s$	(N_{phases}, N_x, N_y)
$k_{r\beta}$	kr	Relative permeability of phase βon the (x, y) grid element	m^2	(N_{phases}, N_x, N_y)
$\mu_{\beta\ xx}$	miu_xx	Average viscosity between consecutive grid elements in the x-direction of flow	$Pa\ s$	$(N_{phases}, N_x - 1, N_y)$

Symbol	gPROMS name	Definition	Units	Array size
$\rho_{\beta\, xx}$	rho_xx	Average density between consecutive elements in the x-direction of flow	kg/m^3	$(N_{phases}, N_x - 1, N_y)$
$k_{r\beta\, xx}$	kr_xx	Average relative permeability between consecutive grid elements in the x-direction of flow	m^2	$(N_{phases}, N_x - 1, N_y)$
$miu_{\beta\, yy}$	miu_yy	Average viscosity between consecutive grid elements in the x-direction of flow	Pa s	$(N_{phases}, N_x, N_y - 1)$
k_{yy}	k_yy	Average permeability between consecutive grid elements in the y-direction of flow	m^2	$(N_x, N_y - 1)$
$rho_{\beta\, yy}$	rho_yy	Average density between consecutive elements in the y-direction of flow	kg/m^3	$(N_x, N_y - 1)$
$k_{r\beta\, yy}$	kr_yy	Average relative permeability between consecutive grid elements in the y-direction of flow	m^2	$(N_{phases}, N_x, N_y - 1)$
$F_{gas_{in}}$	F_CO2_in	Injection flowrate of CO2	kg/s	$(N_{wells}, N_{x,}\, N_y)$
$j_{xx\beta}$	j_phase_xx	Mass flux in in the x-direction	$kg/m^2 s$	$(N_{phases}, N_x + 1, N_y)$
j_{yy_β}	j_phase_yy	Mass flux in in the y-direction	kg/m^{s2}	$(N_{phases}, N_x, N_{y+1})$
$u_{\beta\, xx}$	u_phase_xx	Darcy's velocity in the x-direction	m/s	$(N_{phases}, N_x$+1, $N_y)$
$u_{\beta\, yy}$	u_phase_yy	Darcy's velocity in the y-direction	m/s	$(N_{phases}, N_x, N_{y+1})$
$M_{\beta\, PUV}$	phase_mass_holdup_PUV	Mass holdup of phase βper unit of volume on the (x, y) grid element	kg/m^3	(N_{phases}, N_x, N_y)
M_β	phase_mass_holdup	Mass holdup of phase β on the (x, y) grid element	kg	(N_{phases}, N_x, N_y)
V_β	phase_volume_holdup	Volume holdup of phase βon the (x, y) grid element	m^3	(N_{phases}, N_x, N_y)
$F_{\beta_{injection}}$	F_injection	Mass flowrate of phase β injected on the (x, y) grid element	kg/s	(N_{phases}, N_x, N_y)
$F_{\beta_{extraction}}$	F_extraction	Mass flowrate of phase β injected on the (x, y) grid element	kg/s	(N_{phases}, N_x, N_y)
A_x	area_normal_to_x	Area normal to x-direction of flow	m^2	(N_y)

Symbol	gPROMS name	Definition	Units	Array size
A_y	area_normal_to_y	Area normal to y-direction of flow	m^2	(N_x)
A_z	area_normal_to_z	Area normal to z-direction of flow	m^2	(N_x, N_y)
V	volume	Ratio between void volume and total volume of the porous media	m^3	(N_x, N_y)
dx	dx	Discrete element thickness in x direction	m	N_y
dy	dy	Discrete element thickness in y direction	m	N_x
dz	dz	Discrete element thickness in z direction	m	-
x_{center}	x-center	Discrete element inner position in x direction	m	N_x
y_{center}	y-center	Discrete element inner position in y direction	m	N_y

4.5. Ports

gPROMS Name	Port type	Dimension	Portset
Inlet	CapturedCO2	N_{wells}	-

4.6. Parameter Specifications

Definition of the physical properties package:

$$\text{gas\_prop} := \text{phys\_prop}^{[\text{Inlet}]} < \text{PROCESS\_FLUID} >$$

$$\text{liquid\_prop} := \text{phys\_prop}^{[\text{Inlet}]} < \text{PURE\_WATER} >$$

Define the gas components;

$\mathscr{C}$**:= C** [Inlet]

Set the simulation time, parameter used for time unit conversion. The default simulation time will be 1 year:

$$t_{Simulation} = 365\frac{days}{year} \times 3600\frac{s}{h} \times 24\frac{h}{day}$$

Set the reservoir boundaries:

$$Z_{down} := 0$$

$$Z_{up} := H_{aquifer}$$

$X_{west} := 0$

$X_{east} := L_{x\ aquifer}$

$Y_{north} := 0$

$Y_{south} := L_{y\ aquifer}$

The default value of the flags will be zero. Their value will be set to 1 for the well index coordinates:

FOR i:=1 TO N_{wells}DO

$\mathrm{x}_{\mathrm{well}}^{\mathrm{flag}}(\mathrm{x}_{\mathrm{well}}(\mathrm{i})) := 1$;

$\mathrm{y}_{\mathrm{well}}^{\mathrm{flag}}(\mathrm{y}_{\mathrm{well}}(\mathrm{i})) := 1$;

$\mathrm{well}^{\mathrm{flag}}(\mathrm{x}_{\mathrm{well}}(\mathrm{i}),\ \mathrm{y}_{\mathrm{well}}(\mathrm{i})) := 1$;

END

4.7. Equations

The continuity equation was implemented for each element of the grid. In gPROMS language, the discrete element variables will be represented as an array with the position given by the indexes (i,j):

$$\frac{1}{t_{simulation}} V_{(i,j)} \frac{\partial M_{\beta\ PUV\,(i,j)}}{\partial t} = j_{xx\beta_{(i,j)}} A_{x(i,j)} - j_{xx\beta_{(i+1,j)}} A_{x(i+1,j)} + j_{yy\beta_{(i,j)}} A_{y(i,j)} - j_{yy\beta_{(i,j+1)}} A_{y(i,j+1)} + F_{\beta_{injection_{(i,j)}}} - F_{\beta_{extraction(i,j)}} \quad (4.1)$$

with β representing the phase for which the balance is performed and (i,j) representing the discrete element x and y indexes. The balances are performed for all discrete elements. The same notation will be used in the following equations.

The flux terms will be defined in each interface between consecutive grid elements. For each direction of flow, it comes:

$$j_{xx\beta_{(i,j)}} = -k_{xx(i-1,j)} \frac{k_{r\beta\,xx(i-1,j)} \rho_{xx\beta_{(i-1,j)}}}{\mu_{\beta\,xx(i-1,j)}} \left(\frac{p_{\beta_{(i,j)}} - p_{\beta_{(i-1,j)}}}{(dx_i + dx_{i-1})/2} \right) \quad (4.2)$$

$$j_{yy\beta_{(i,j)}} = -k_{yy(i,j-1)} \frac{k_{r\beta\,yy(i,j-1)} \rho_{yy\beta_{(i-1,j)}}}{\mu_{\beta\,yy(i,j-1)}} \left(\frac{p_{\beta_{(i,j)}} - p_{\beta_{(i,j-1)}}}{(dy_j + dy_{j-1})/2} \right) \quad (4.3)$$

The holdup variables relation with the volume of media and fluid phase density will be given by the following equations:

$$M_{\beta\ PUV\,(i,j)} = \phi_{(i,j)} S_{\beta_{(i,j)}} \rho_{\beta_{(i,j)}} \quad (4.4)$$

$$M_{\beta_{(i,j)}} = M_{\beta\ PUV\,(i,j)} V_{(i,j)} \quad (4.5)$$

$$V_{\beta_{(i,j)}} = \frac{M_{\beta_{(i,j)}}}{\rho_{\beta_{(i,j)}}} \tag{4.6}$$

$$\sum_{i=1}^{N_x}\sum_{j=1}^{N_y} S_{\beta_{(i,j)}} = 1 \tag{4.7}$$

To evaluate the relative permeability, the following functions were implemented:

Brooks and Corey correlation:

$$S_{r\,liquid_{(i,j)}} = \frac{S_{liquid_{(i,j)}} - S_{lr}}{1 - S_{lr} - S_{gr}} \tag{4.8}$$

$$k_{r\,liquid_{(i,j)}} = S_{r\,liquid_{(i,j)}}{}^{4} \tag{4.9}$$

$$k_{r\,liquid_{(i,j)}} = \left(1 - S_{r\,liquid_{(i,j)}}{}^{2}\right)\left(1 - S_{r\,liquid_{(i,j)}}\right)^{2} \tag{4.10}$$

van Genuchten correlation:

$$S_{r\,liquid_{(i,j)}} = \frac{S_{liquid_{(i,j)}} - S_{lr}}{1 - S_{lr}} \tag{4.11}$$

$$k_{r\,liquid_{(i,j)}} = S_{r\,liquid_{(i,j)}}{}^{1/2}\left(1 - \left(1 - S_{r\,liquid_{(i,j)}}{}^{1/m}\right)^{m}\right)^{2} \tag{4.12}$$

$$k_{r\,gas_{(i,j)}} = \left(1 - S_{r\,liquid_{(i,j)}}\right)^{1/2}\left(1 - S_{r\,liquid_{(i,j)}}{}^{1/m}\right)^{2m} \tag{4.13}$$

The physical properties of the fluid phases that are calculated with the Multiflash foreign object will be defined as follows:

$$\rho_{gas_{(i,j)}} = \text{phys\_prop.VapourDensity}\left(T_{(i,j)}, p_{gas_{(i,j)}}, w_{gas}\right) \tag{4.14}$$

$$\rho_{liquid_{(i,j)}} = \text{phys\_prop.LiquidDensity}\left(T_{(i,j)}, p_{liquid_{(i,j)}}, w_{liquid}\right) \tag{4.15}$$

$$\mu_{gas_{(i,j)}} = \text{phys\_prop.VapourViscosity}\left(T_{(i,j)}, p_{gas_{(i,j)}}, w_{gas}\right) \tag{4.16}$$

$$\mu_{liquid_{(i,j)}} = \text{phys\_prop.LiquidViscosity}\left(T_{(i,j)}, p_{liquid_{(i,j)}}, w_{liquid}\right) \tag{4.17}$$

For the calculation of the capillary pressure, the effective saturation will be given by:

$$S_{m_{(i,j)}} = \frac{S_{liquid_{(i,j)}} - S_{lr}}{1 - S_{lr}} \tag{4.18}$$

As the capillary pressure curve exhibits unphysical behaviour when the liquid saturation approaches its residual value, the maximum value of 1×10^7 Pa will be assumed. For the applicable range though, the van Genuchten correlation will be computed as it follows:

$$p_{cap_{(i,j)}} = -P_0 \left({S_{m_{(i,j)}}}^{-1/\lambda} - 1 \right)^{1-\lambda} \tag{4.19}$$

To calculate the mean properties between consecutive grid elements, the upstream weighting scheme will be employed. The evaluated functions in the x-direction will be, hereby represented by $f_{xx_{(i,j)}}$, and implemented for the density, ρ_{xx}, permeability, k_{xx}, relative permeability, $k_{r_{xx}}$, and viscosity, μ_{xx}.

WHEN harmonic:

$$f_{xx_{(i,j)}} = \frac{f_{(i,j)} f_{(i+1,j)} (dx_{(i)} + dx_{(i+1)})}{\delta + f_{(i,j)} dx_{i+1} + f_{(i+1,j)} dx_{(i)}} \tag{4.20}$$

WHEN arithmetic:

$$f_{xx_{(i,j)}} = \frac{f_{(i,j)} dx_{(i)} + f_{(i+1,j)} dx_{(i+1)}}{\delta + dx_{(i)} + dx_{(i+1)}} \tag{4.21}$$

WHEN logarithmic:

$$f_{xx_{(i,j)}} = \frac{\left(\delta + \frac{log\left(1 - f_{(i+1,j)}\right)}{f_{(i,j)}} \right) + f_{(i+1,j)}}{f_{(i,j)} \left(\delta + \frac{log\left(1 - f_{(i+1,j)}\right)}{f_{(i,j)}} \right)} \tag{4.22}$$

The first and last coordinates of the boundaries of the elements of the grid will be defined by the reservoir dimensions. For the inner interface and centre coordinates, the following equations will be implemented:

$$x_{(i,j)} = x_{(i-1,j)} + dx_{(i-1)} \tag{4.23}$$

$$x_{center_{(i,j)}} = \frac{x_{(i,j)} + x_{(i+1,j)}}{2} \tag{4.24}$$

$$y_{(i,j)} = y_{(i,j-1)} + dy_{(j-1)} \tag{4.25}$$

$$y_{center_{(i,j)}} = \frac{y_{(i,j)} + y_{(i,j+1)}}{2} \tag{4.26}$$

The interfacial areas, normal to the flow, will be given by:

$$A_{x_{(j)}} = dy_j dz \tag{4.27}$$

$$A_{y_{(i)}} = dx_i dz \tag{4.28}$$

By default, the grid elements will be equally spaced but the model can also accommodate proper user defined grid refinements. The user will have the option to include the variation in the pore volume caused by the changes in the pressure gradient. If the pressure dependant porosity is selected, it will be given by the following approximated expression [32]:

$$\phi_{(i,j)} = \phi_{0_{(i,j)}} \left(1 + c_R \left(p_{(i,j)} - {p^0}_{(i,j)} \right) \right) \tag{4.29}$$

4.7.1. Port connections

The variables in each port connection are identified by the symbol for that type of variable and a superscript containing the name of the port in brackets: e.g. $T^{[inlet]}$ is the temperature variable in the port called outlet; in gPROMS language, this would be outlet.T.

FOR i:=1 TO N_{wells}DO

FOR j:=1 TO N_xDO

FOR k:=1 TO N_y DO

$\mathrm{w}^{[\,\mathrm{inlet\ (i)}\,]} = \mathrm{w}(,\mathrm{j},\mathrm{k})$

IF $j = x_{well}(\mathrm{i})$ and $k = y_{well}(\mathrm{i})$ THEN

$\mathrm{F}^{[\,\mathrm{inlet\ (i)}\,]} = F_{gas_{in}}(\,i\,,j\,,k\,)$

ELSE

$0 = F_{gas_{in}}$

END

END

END

$\mathrm{T}^{[\,\mathrm{inlet\ (i)}\,]} = \mathrm{T}_{\mathrm{source}}(i)$

$\mathrm{h}^{[\,\mathrm{inlet\ (i)}\,]} = \mathrm{h}_{\mathrm{source}}(i)$

$\mathrm{T}^{[\,\mathrm{inlet\ (i)}\,]} = \mathrm{p}\big('\mathrm{gas}', \mathrm{x}_{\mathrm{well}}(\mathrm{i}), \mathrm{y}_{\mathrm{well}}(\mathrm{i})\big)$

END

5. Validation and Sensitivity analysis

In order to validate the saline aquifer model, simulations will be performed in this chapter with a set of petrophysical properties of the Johansen formation. The corresponding wellblock pressure was compared with the bottom-hole pressure obtained with simulations of the injection into this formation, performed with the commercial simulator ECLIPSE Black Oil E100. Further studies include a sensitivity analysis to the porosity and permeability, and the simulation of the injection into planned sequestration sites of important CCS projects.

5.1. Model validation

5.1.1. Johansen Formation

The Johansen formation is located in the south-western coast of Norway, being one of the candidate sequestration sites of CO_2 emissions from the future point source at Mongstad. Its depth levels range from 2200-3100 m below sea level, making it ideal for CO_2 storage due to the existing pressure regimes. Figure 5.1 shows its schematic location, within the green curve, the areas for which the seismics are known, within the yellow curve, and the boundaries of the Norwegian sector of the Utsira formation, delimited by the blue line [33].

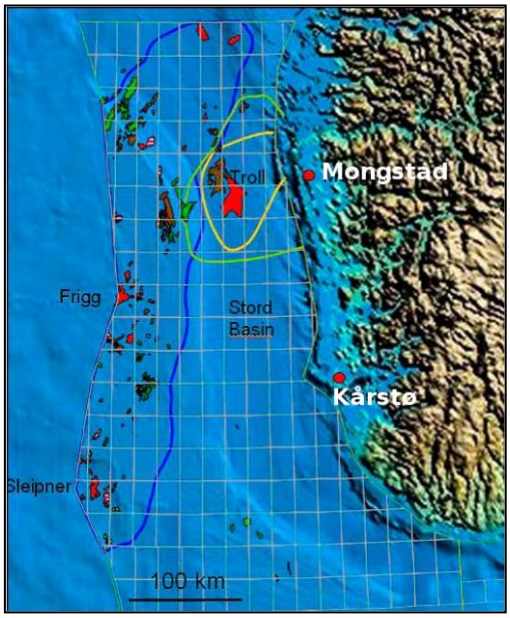

Figure 5.1 – Schematic locations of the Utsira and Johansen formations (after [33])

Eigestad et al. developed a geological model of the Johansen formation, based on available seismic and well data, as part of the "Geological Storage of CO_2: Mathematical Modelling and Risk Analysis" (MatMoRA) project. The model has been published online covering a detailed real data set including geometry, reservoir conditions, petrophysical and fluid data [34]. In addition, simulations of the injection into Johansen were performed using the industry standard black oil simulator Eclipse E100.

Figure 5.2 shows the bottom-hole pressure (BHP) obtained from the numerical simulations with three different sets of boundary conditions: the red curve corresponds to no-flow boundaries with increased pore volumes at boundary cells (BC1), the blue curve to flux/pressure control in boundary cells (BC2) and the green to an aquifer support (BC3). The assumptions behind the formulation of these boundary conditions will not be explained here, being found at [33].

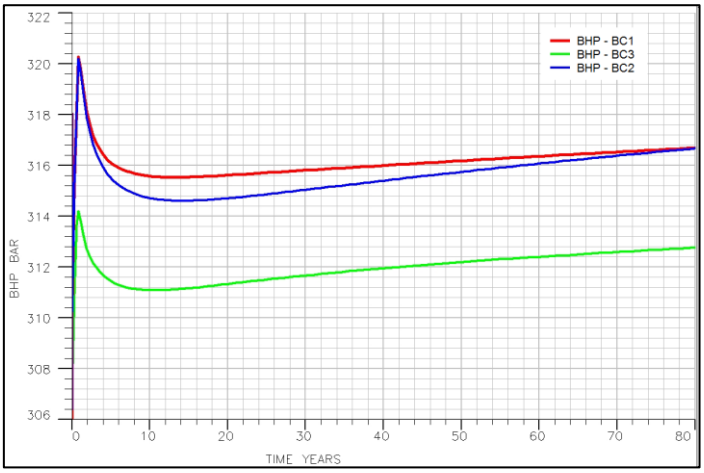

Figure 5.2 – Bottom hole pressure (BHP) versus time for different boundary conditions (after [33])

For all the boundary conditions studied, the BHP pressure experienced initially a sharp transient response, consisting in a rapid pressure increase, followed by a decrease and, after this period, a slow long term increase of the BHP. Using these results as an evaluation basis, the saline aquifer model developed in this thesis was employed to describe this injection problem, with the parameters specified with data from the Johansen dataset.

In addition to considering different boundary conditions in their work, Eigestad et al. also studied the effect of the relative permeability hysteresis. Accordingly, a set of different relative permeability curves was provided. In the saline aquifer formulation, no-flow boundary conditions are employed and the hysteresis effects neglected (chapter 3).

In Figure 5.3, the relative permeability curves predicted by the van Genuchten correlations, eq. (2.8) and (2.9), are plotted against the original curves obtained from the Johansen dataset. The van Genuchten parameter used, m = 0.4 for both phases, was obtained from previous works on CO_2 injection modelling into saline aquifers ([32], [6]).

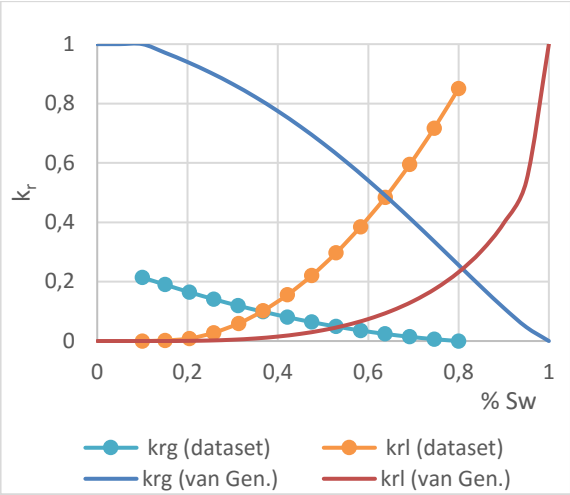

Figure 5.3 – Original kr curves (after [34]) and van Genuchten correlation (m_{gas} = m_{liquid} = 0.4)

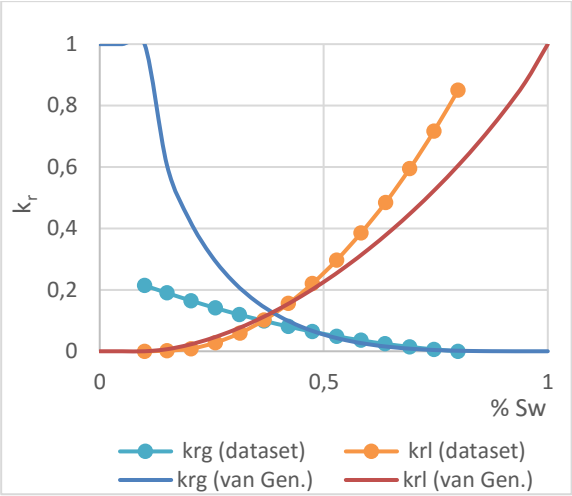

Figure 5.4 – Original kr curves (after [34]) and adjusted van Genuchten correlation (m_{gas} = 1.5 and m_{liquid} = 0.85)

A large discrepancy between the values predicted by the van Genuchten correlation and original permeability curves was observed over the entire range. Thus, the van Genuchten parameter, m, related to the pore distribution, was tuned for each phase (Figure 5.4). Although the discrepancy between the curves is reduced, for the higher water saturation region, van Genuchten correlation still underestimate the original permeability values.

Corey correlation, eq. (2.10) and (2.11), was also implemented and the parameters were also chosen based on previous studies of CO_2 injection ([32], [6]), $n_{gas} = 2$ and $n_{liquid} = 4$. The respective curves (Figure 5.5) show a higher degree of consistency than the van Genuchten. However, in order to reduce the discrepancies, once more a parameter fitting was performed. Analysing the adjusted Corey correlation curve (Figure 5.6), it can be seen that the liquid-phase curve shows a good degree of consistency but, for the gas-phase, in the lower half of water saturation region, the relative permeabilities are largely overestimated.

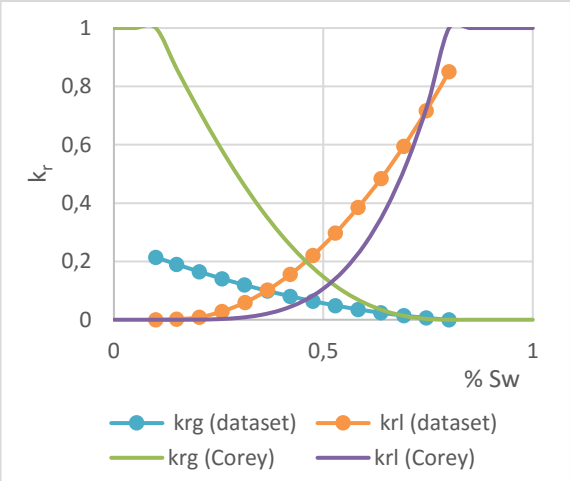

Figure 5.5 – Original kr curves (after [34]) and Corey correlation (n_{gas} = 2 and n_{liquid} = 4)

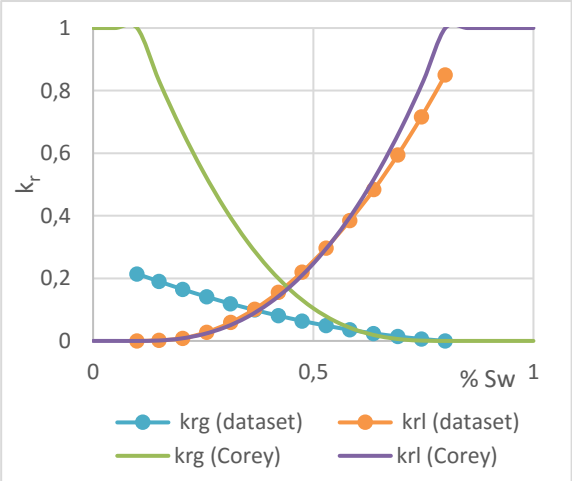

Figure 5.6 – Original kr curves (after [34]) and adjusted Corey correlation (n_{gas} = n_{liquid} = 2.5)

Taking the results above into account, different combinations of relative permeability correlations were employed in the simulations (Table 5.1).

Table 5.1 – Cases of relative permeability employed at the study of the injection into Johansen formation

Case 1: Corey correlations
Case 2: van Genuchten correlations
Case 3: Corey gas- and van Genuchten liquid-phase correlations
Case 4: van Genuchten gas- and Corey liquid-phase correlations

Moreover, there were some characteristics of the Johansen Geological model simulations that were directly assigned to the saline aquifer such as injection flowrate, temperature and the irreducible saturations (Table 5.2).

Table 5.2 – Johansen detailed model and Saline aquifer injection characteristics

Characteristic	**Value** (after [33])
Injection Flowrate	3.5 Mton/year
Temperature	Constant (94 ºC)
Irreducible water saturation	0.1
Irreducible CO_2 saturation	0.2

The physical properties were also taken from the Johansen Data set and the Lookup interpolation method featured on gPROMS Model Builder was implemented at the model to read the fluid system data file. It characterises an immiscible, two-phase isothermal system of water and CO_2 phases. The densities and viscosities were given for 94 ºC and pressure values in the range that exists during the simulation time, (from 230 to 400 bar). Figure 5.7 and Figure 5.8 display the properties for the water- and the CO2-rich phases, respectively.

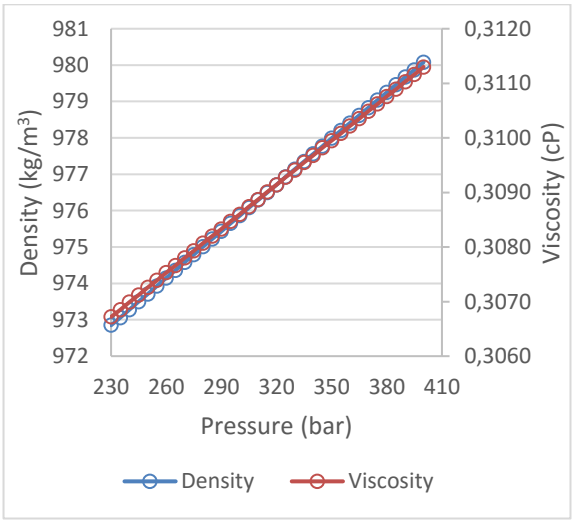

Figure 5.7- Johansen Data Set H_2O PVT properties (94 ºC) (after [34])

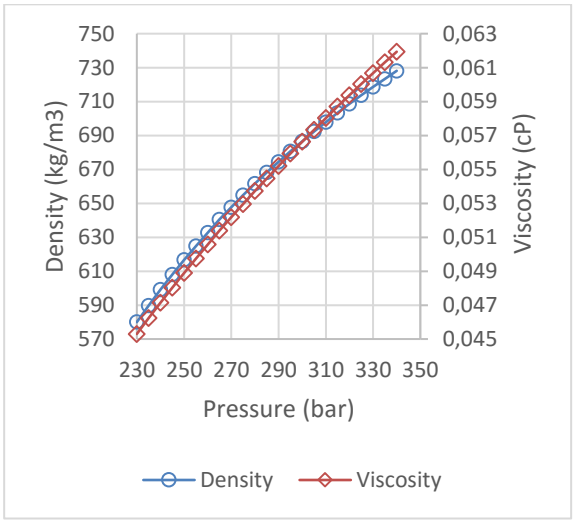

Figure 5.8 – Johansen Data Set CO_2 PVT properties (94 ºC) after [34])

Moreover, on Table 5.3 and Table 5.4, the characteristics of the Geological model simulations performed on Eclipse are presented, together with the correspondent characteristics, adapted to the saline aquifer model.

Table 5.3 – Johansen formation and saline aquifer model specifications

Characteristic	**Johansen Geological Model value** ([33], [34]))	**Saline aquifer model value**
Initial pressure	Hydrostatic equilibrium (250-310 bar)	306 bar
Reservoir thickness	Variable (Average value:100 m)	Uniform (100 m)
Lateral extensions	North-south direction: up to 100 km East-west direction: up to 60 km	60 x 100 km
Flow geometry	3D (x-y-z)	2D (x-y)
Grid characterization	Full-field model: (149x189x16)	(101 x 101)
Grid refinement	Horizontal and vertical refinement	None

Table 5.4 – Johansen formation and saline aquifer model petrophysical properties specifications

Characteristic	**Johansen Geological Model value** (after [33])	**Saline aquifer model value**
Permeability	Isotropic in x-y directions z-direction permeability: 1/10 of x-y directions Average value: 500 mD	Isotropic (500 mD)
Porosity	Average value: 0.25	0.25

5.1.2. Johansen Formation simulations results

The wellblock pressure obtained from the simulations of the injection into Johansen, performed with the developed model, are presented on Figure 5.9. It's important to pinpoint the fact that, on the results presented henceforth, the number of grid elements was limited to 101 in each direction, due to computational constraints.

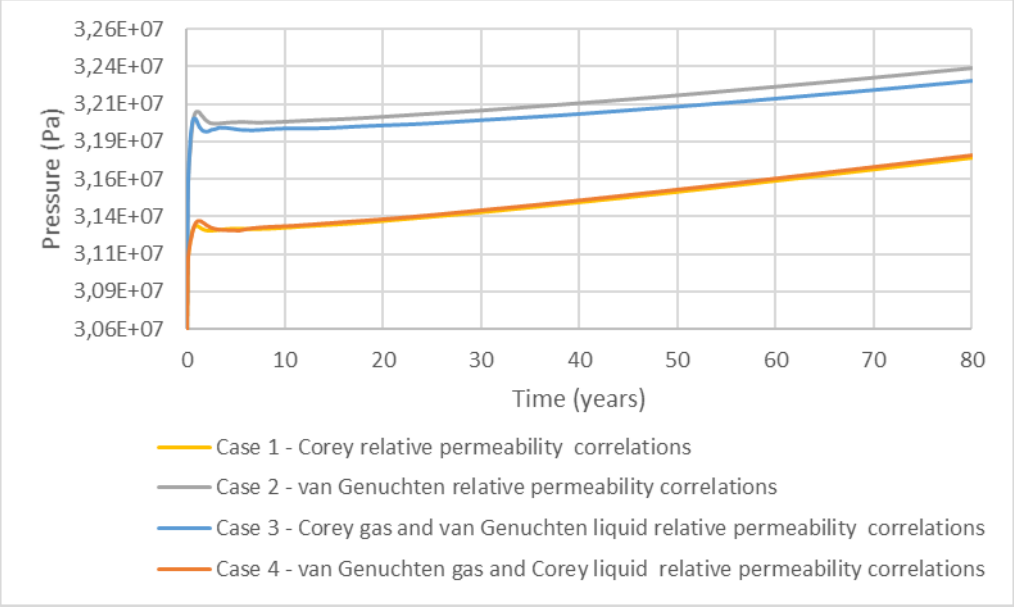

Figure 5.9 – Johansen aquifer wellblock pressure for different sets of relative permeability correlations

For all the combinations of relative permeability cases studied, the response to the injection was analogous to that observed with the Johansen Geological model simulations. On the first years, the pressure underwent a fast substantial increase followed by a decrease and, after this short transient response, a long period of slow growth was seen.

The first transient response and the second phase of increase were respectively not as sharp and sluggish, by the end of 80 years of injection, the wellblock pressure predicted by the Cases 1 and 4, where Brooks and Corey correlation was used in the description of the liquid relative permeability, have fallen over the same range anticipated by the Eclipse simulations (Figure 5.2). In fact, for these cases, the final result deviates only 0.14% from the values predicted by the detailed geological model with the no-flow boundaries condition. On the other hand, for the Cases 2 and 3, where van Genuchten correlation was employed to represent the liquid-phase relative permeability, the initial response was comparable but, after 80 years, the pressure is overestimated by about of 8 bar. Corey formulation is the correlation with a better fit to the Johansen original permeability, being the reason behind the large difference between the wellblock pressure and demonstrating the importance of the relative permeability description.

The pressure buildup is highly dependent on relative permeability representation. Moreover, the grid refinement also plays an important part, particularly on the accuracy of the results and capture of the transient response on the first five years of injection. The effect of the number of grid elements on the pressure build-up was hereby investigated. Figure 5.10 and Figure 5.11 display the effect of the grid refinement on the initial pressure response for the Cases 1 and 4.

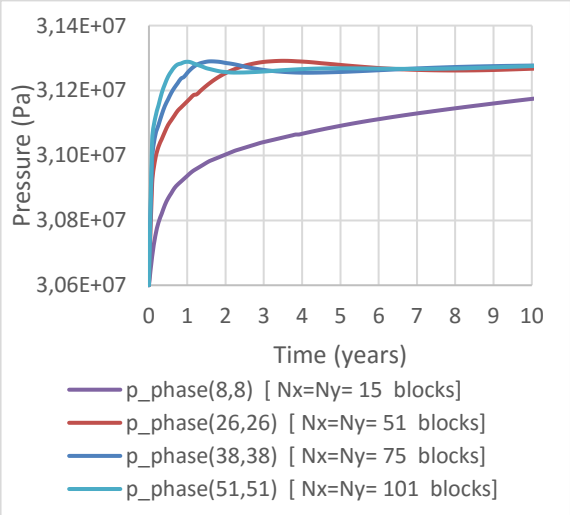

Figure 5.10 – Johansen aquifer grid effect on wellblock pressure analysis for Case 1 (t=10years)

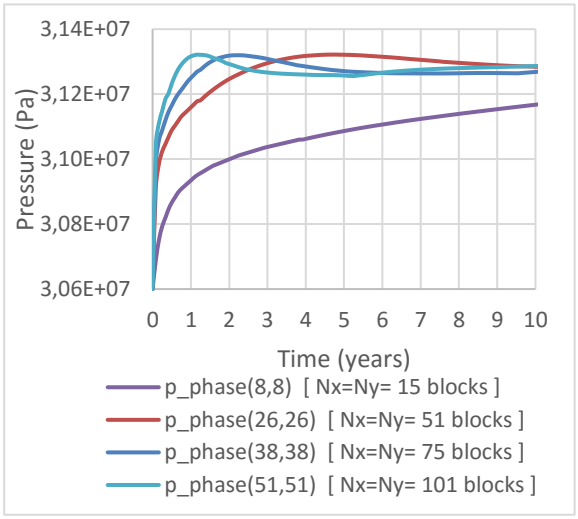

Figure 5.11 – Johansen aquifer grid effect on wellblock pressure analysis for Case 4 (t=10years)

With the grid effect analysis, it was possible to see that the initial wellblock pressure response was as fast and prominent as larger the number of grid elements evaluated. To study this outcome, the mass fluxes were evaluated in the x-direction taking the east face of the wellblock and the N_x= N_y=101 and N_x= N_y=51 grid cases (Figure 5.12 and Figure 5.13). The gas-phase was nearly immobile in the early beginning when, in parallel, the liquid was rapidly pushed out of the wellblock. The grid refinement ruled the length of the initial period, once there was a delay on the response of approximately two years.

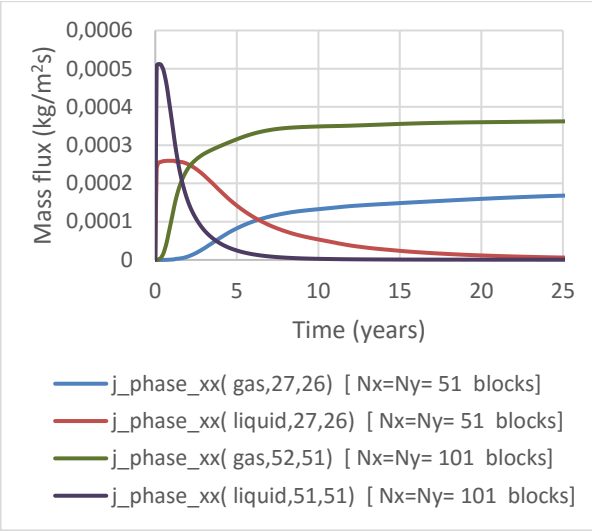

Figure 5.12 – Johansen aquifer mass fluxes at the east face of wellblock analysis for Case 1

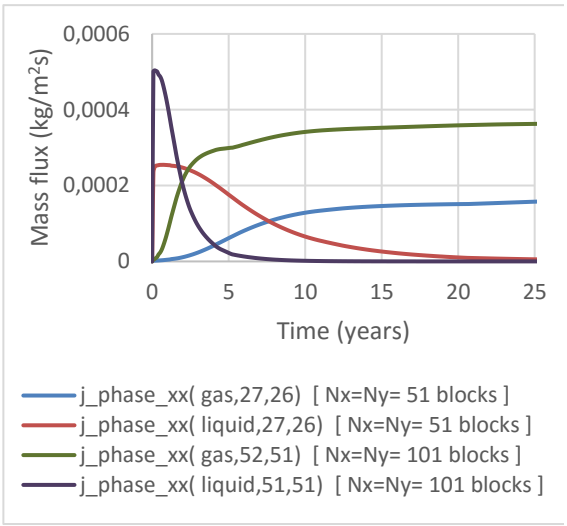

Figure 5.13 – Johansen aquifer mass fluxes at the east face of wellblock analysis for Case 4

The volume saturation dependant relative permeability grounds the mass fluxes behaviour (Figure 5.14 and Figure 5.12). Before the injection begins, the gas-phase is only found in the residual form in the aquifer. Accordingly, its low relative permeability will hinder its movement while the wellblock liquid-phase relative permeability assumes its maximum value, explaining the instantaneous movement of the liquid-phase. The CO_2 accumulation in the wellblock aids the gas-phase saturation growth and, accordingly, its relative permeability, launching the CO_2 movement to the surrounding grid elements. The combination of increasing relative permeability and installed pressure gradient between the wellblock and surrounding grid elements underlies the small decrease watched in the pressure.

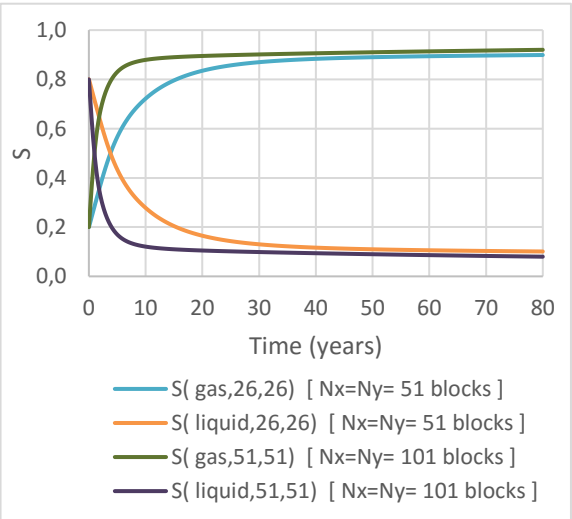

Figure 5.14 – Johansen aquifer wellblock volume saturations analysis for Case 1

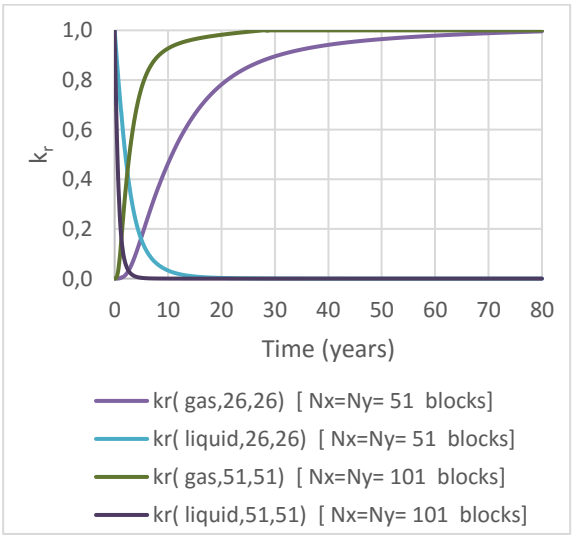

Figure 5.15 – Johansen aquifer wellblock relative permeabilities analysis for Case 1

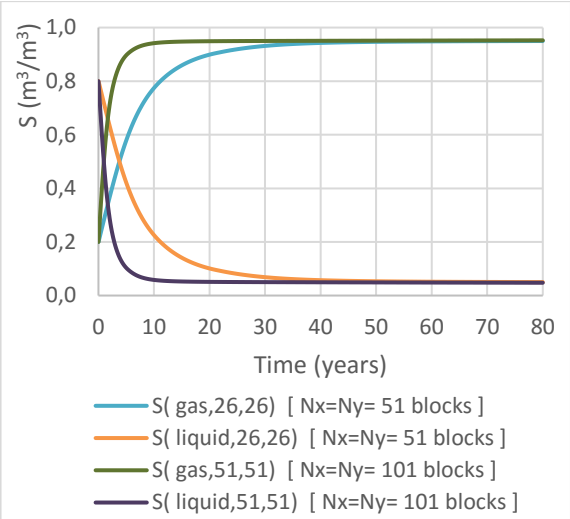

Figure 5.16 – Johansen aquifer wellblock volume saturation analysis for Case 4

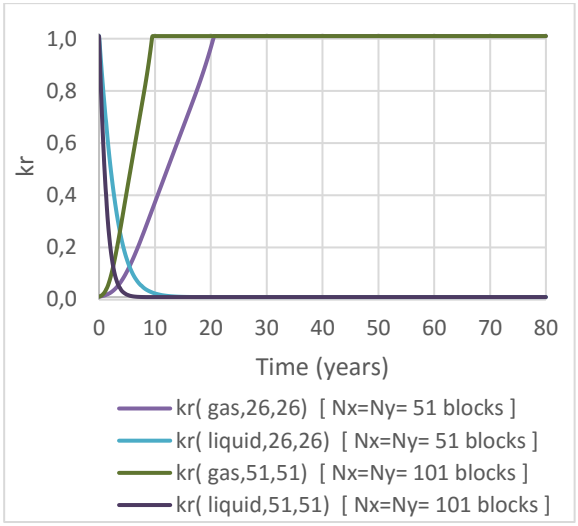

Figure 5.17 – Johansen aquifer wellblock relative permeabilities analysis for Case 4

In the long term, all the simulations performed with different number of discrete elements have given rise to coherent results that fall into the same range of the ones obtained with eclipse. Therefore, among the fundamental differences between the models, the difference between the initial responses are essentially governed by the grid refinement effects. Nevertheless, the curve shapes and the long term convergence demonstrate a fair degree of consistency between both models.

A final look will be given to the pressure distribution at the aquifer (Figure 5.18 and Figure 5.19). At the end of 10 years, the pressure perturbation caused by the CO_2 injection is mainly focused in the near wellblock area and the cone shaped pressure distribution is slightly distorted in the x-direction, showing a faster disturbance spread. This trend is observed because the Johansen aquifer dimensions are distinct (Table 5.3). After 80 years, the whole reservoir extension has been affected by the CO_2 injection, with an increase of 6 bar at the y-direction boundaries, the furthest away from the wellblock. Also, the pressure distribution cone is considerably more widespread and distorted in the x-direction, reaching the respective boundaries.

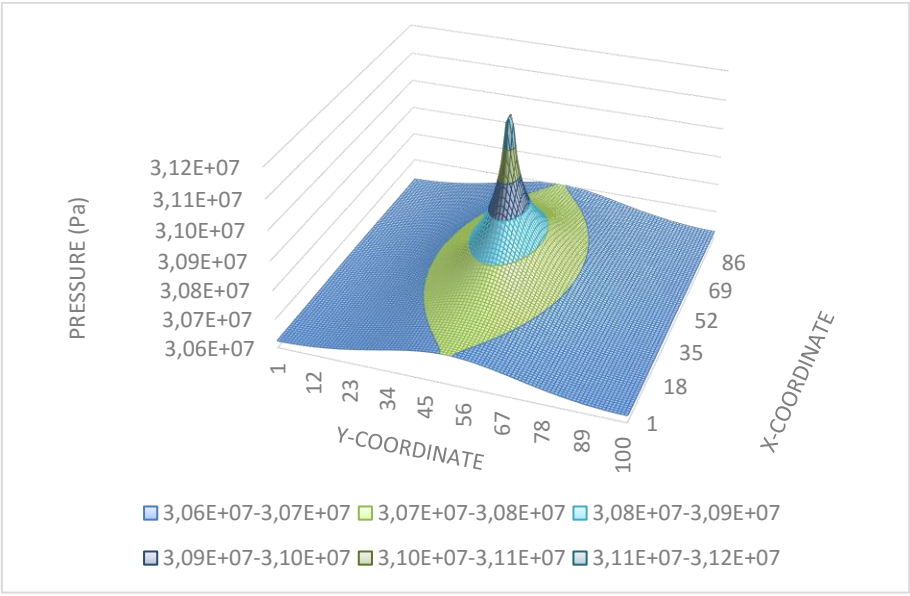

Figure 5.18 – Pressure distribution in the Johansen formation after 10 years of injection for Case 1

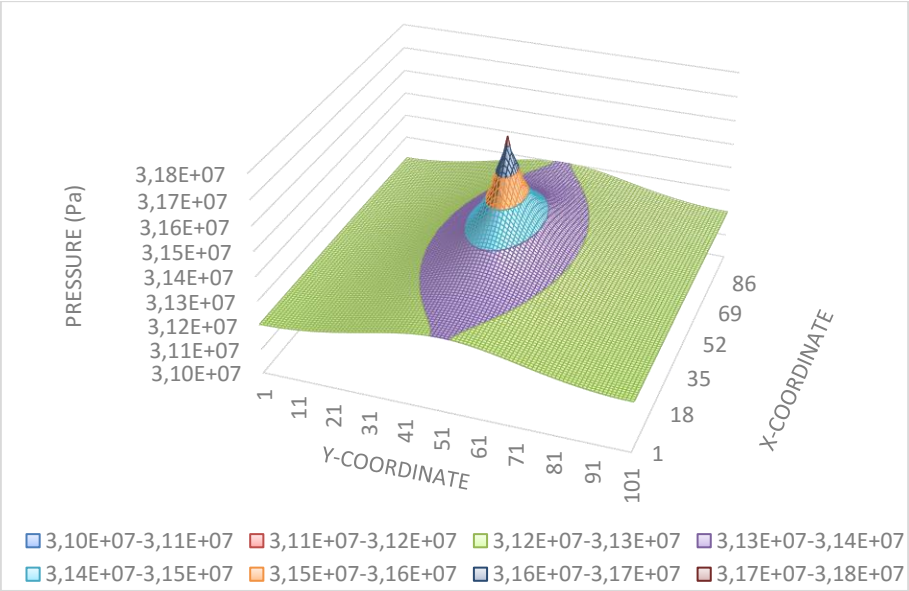

Figure 5.19 – Pressure distribution in the Johansen formation after 80 years of injection for Case 1

5.2. Model applicability and sensitivity analysis

The petrophysical properties of the reservoir heavily affect the flow characteristics, hence the CO_2 and pressure distributions. Thus, in this subsection, a sensitivity analysis will be performed to the main parameters that influence it, namely the permeability and porosity. The basic model specifications required to perform the sensitivity analysis simulations were grounded on earlier studies of CO_2 injection modelling ([32], [35]), being summarized in Table 5.5 and Table 5.6.

Table 5.5 – Sensitivity analysis simulations specifications

Property	**Value**		**Unity**
Physical properties	Multiflash		-
Simulation time	60 x 60 x 364 x 24		s
Injection time	30		years
Initial pressure	120		bar
Temperature	Reservoir CO_2 stream	45	º C
Injection flowrate	100		kg/s
Relative permeability correlation	van Genuchten		
	S_{lr}	0.30	-
	S_{gr}	0.05	-
	m	0.46	-
Media deformability	Pressure dependant		-
	Pore compressibility	4.50E-10	Pa^{-1}

Table 5.6 – Sensitivity analysis grid configuration

Variable	Property	Value	Unity
Grid configuration	N_x x N_y	75 x 75	elements
	N_{wells}	1	-
	(x_{well} , y_{well})	(38, 38)	-
Extension in x and y directions	100		km

To establish the range over which the petrophysical properties vary, basins suitable for CO_2 sequestration were investigated. A report of work on practical injections projects for CO_2 issued by the Scottish Centre for Carbon Capture and Storage was accessed [9]. It featured important petrophysical properties of the sequestration sites including formation depth, permeability, porosity and also the planned rates of injection. The majority of the aquifers considered by the CCS projects exhibited porosities greater to 10%, with a maximum of 37% at Sleipner. As for the permeabilities, the most part of the commercial scale projects presented considerable permeabilities, 5000 mD at Sleipner, as well as very low ones, 5 mD at In Salah. Thus, the sensitivity analysis simulation settings were chosen in accordance. The porosity and permeability sensitivity analysis simulation settings are displayed on Table 5.7 and Table 5.8, respectively.

Table 5.7 – Porosity sensitivity analysis simulations settings

Variable	Value	Unity
Intrinsic permeability	500	mD
Porosity	0.12 / 0.2 / 0.25 / 0.3 / 0.35	-

Table 5.8 – Permeability sensitivity analysis simulations settings

Variable	Value	Unity
Intrinsic permeability	10 / 50 / 500 / 5000	mD
Porosity	0.25	-

5.2.1. Porosity sensitivity analysis

The wellblock pressures obtained for the porosity sensitivity analysis cases simulations are depicted in Figure 5.20. For the first 5 years, the wellblock pressure showed a similar development trend, with little dependence on the porosity for all the cases studied. Nevertheless, after this first period, the wellblock pressure starts to diverge with a rate of growth inversely proportional to the studied porosity values.

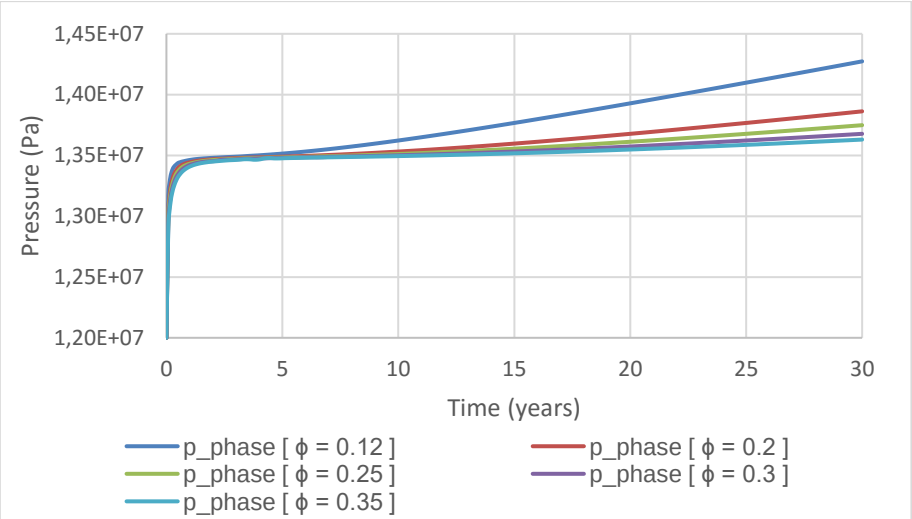

Figure 5.20 – Wellblock pressure for porosity sensitivity analysis

For all the studied cases, a pressure increase of about 12% was seen at the end of the first year (Table 5.9). A second period of growth followed, with a pressure rise far more distinct between the cases. For the smaller porosity studied (ϕ = 0.12), an increase of 6.0% was seen when, for the higher porosity case (ϕ = 0.35), the increase was significantly smaller, only 1.6%. For a better understanding, the mass fluxes in the x-direction were evaluated at the east face of the wellblock (Figure 5.21).

Table 5.9 – Porosity sensitivity analysis wellblock pressure results

Variable	$\phi = 0.12$	$\phi = 0.20$	$\phi = 0.25$	$\phi = 0.30$	$\phi = 0.35$
$P_{t=1\ year}$ (bar)	134.6	134.5	134.4	134.3	134.1
Deviation of $P_{t=1\ year}$ from $P_{t=0}$	12.2%	12.1%	12.0%	11.9%	11.8%
$P_{t=30\ years}$ (bar)	142.7	138.6	137.5	136.8	136.3
Deviation of $P_{t=30\ years}$ from $P_{t=1\ year}$	6.0%	3.1%	2.3%	1.9%	1.6%

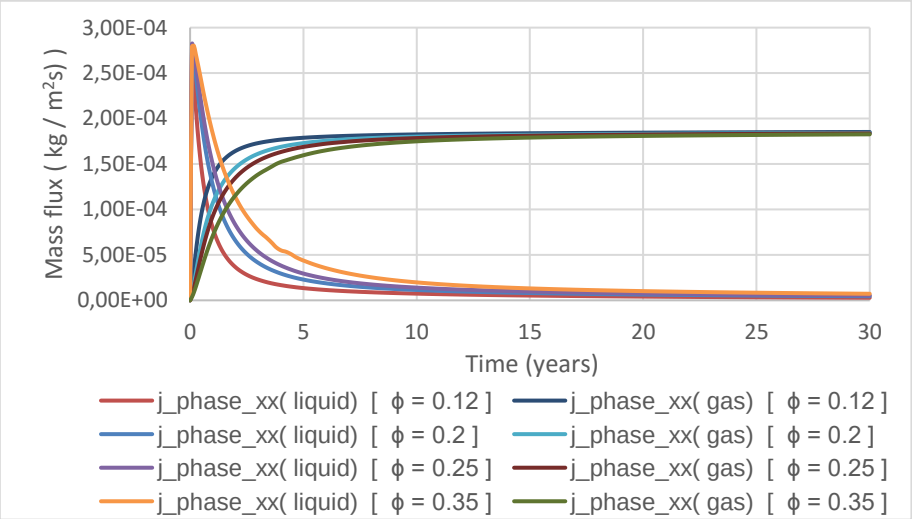

Figure 5.21 – Mass-flux at x-direction at east-face of wellblock for porosity sensitivity analysis

There is a clear difference between the mass fluxes of both phases for the first 5 years. The porosity is directly related to the static storage capacity of an aquifer, hence the initial liquid mass holdup of 21.2 Mton existent on the wellblock for the ϕ =0.12 case and of 61.9 Mton for the ϕ =0.35. Superior liquid-phase mass fluxes are then seen for the higher porosity cases and, more importantly, for the gas-phase, higher fluxes are linked to the smaller porosities. For t=10 years, the sum of the flowrate of the gaseous CO_2 phase that leaves the faces of the wellblock corresponds to 97 kg/s for the ϕ =0.12 case and 93 kg/s for the ϕ =0.35 case. Since the injected mass-flowrate equals 100 kg/s of CO_2, it can be seen that the time that the wellblock fluxes take to stabilize as the perturbation moves towards the surrounding grid blocks is directly related to the porosity.

To assess the perturbation spread, the pressure distribution was evaluated in the x-direction at the end of 5, 10, 20 and 30 years of injection (Figure 5.22 and Figure 5.23).

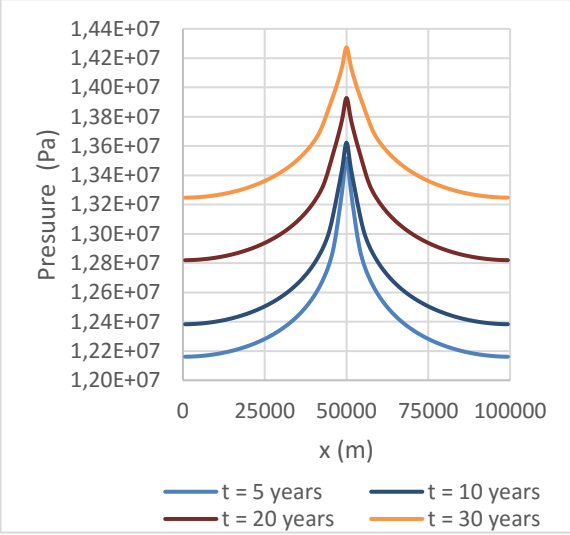

Figure 5.22 – Pressure distribution for ϕ = 0.12

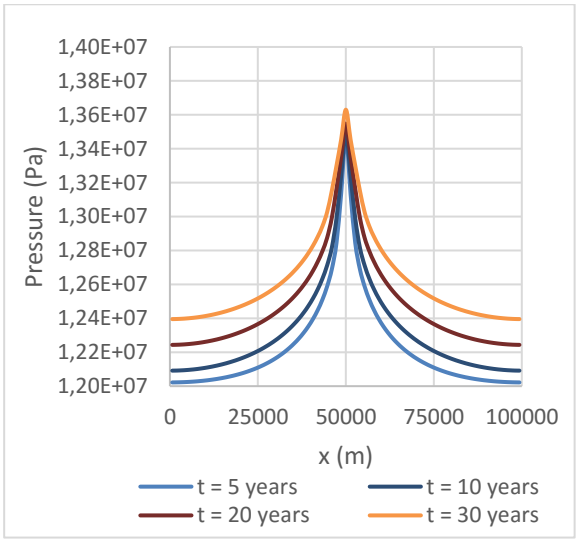

Figure 5.23 – Pressure distribution for ϕ = 0.35

The pressure distributions highlighted the fact that, for the smaller porosity case, the pressure perturbation was quickly transmitted to the whole aquifer extent. As it was previously referred, the porosity is an indicator of the reservoir capacity and once the permeability are equal, to maintain the continuous injection, the pressure has to increase much more significantly, in order to push and compress the resident brine. Hence the global pressure increase that is immediately seen.

Figure 5.21 shows that, for the smaller porosity case (ϕ = 0.12), the wellblock mass fluxes only start to stabilize after 10 years of injection, hence the small wellblock pressure (p_phase(x=50000 m)) difference seen between t=5 and t=10 years of injection. However, after this period, the perturbation spread is more significant once the flowrate of CO_2 leaving the wellblock approaches the steady state. In response, there is a substantial global pressure increase and a greater injection pressure is required. For the higher porosity case (ϕ = 0.35), the fluxes take around 20 years to stabilize, justifying the perturbation focus at the wellblock area, as can be seen on Figure 5.23. Thus, there is not a significant pressure increase in the wellblock between the 1st and 20th years (Figure 5.20), starting to rise again afterwards, as it was previously explained.

5.2.2. Permeability Sensitivity analysis

The wellblock pressure obtained for the permeability sensitivity analysis is showed on Figure 5.24. Unlike what was seen for the porosity (Figure 5.20), there is a large difference between the results, not only in value but also on the development trends. Two periods of growth were detected with opposite dependencies on the permeability. An abrupt rise is seen at the beginning of injection, by the end of the first year with growths of 66%, 15% and 6% identified for the 50 mD, 500 mD and 5000 mD cases, respectively (Table 5.10), showing rates of growth inversely proportional to the permeability. Inversely, at the years that follow, an increase of 2% is observed for the smallest permeability case (50 mD), 2.3% for the intermediate (500 mD) and 4.7% for the highest (5000 mD).

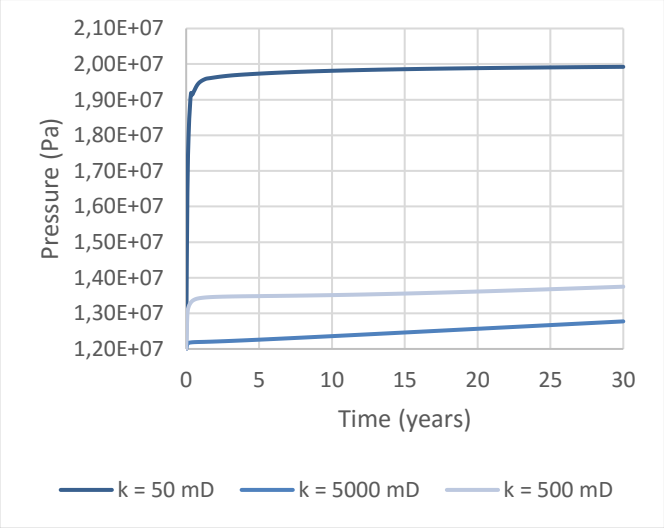

Figure 5.24 - Wellblock pressure for permeability sensitivity analysis

Table 5.10 – Permeability sensitivity analysis wellblock pressure results

Variable	k = 50 mD	k = 500 mD	k = 5000 mD
$P_{t=1\ year}$ (bar)	195.4	134.4	122.0
Deviation of $P_{t=1\ year}$ from $P_{t=0}$	63%	12%	2%
$P_{t=30\ years}$ (bar)	199.2	137.5	127.7
Deviation of $P_{t=30\ years}$ from $P_{t=1\ year}$	2.0%	2.3%	4.7%

Figure 5.24 showed the pressure response to the injection on the grid element that enclosed the injection/well term (welllock). To evaluate the permeability effect on the global reservoir extension and on the different rates of growth referred above, the pressure distribution in the x-direction was assessed after 5, 10, 20 and 30 years of injection (Figure 5.25 to Figure 5.27).

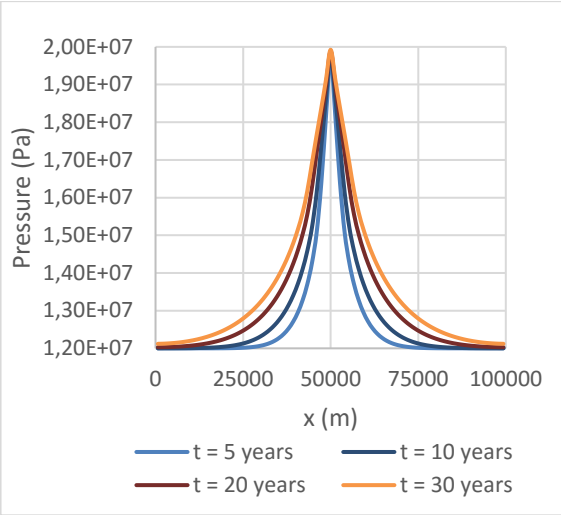

Figure 5.25 – Pressure distribution for k = 50 mD

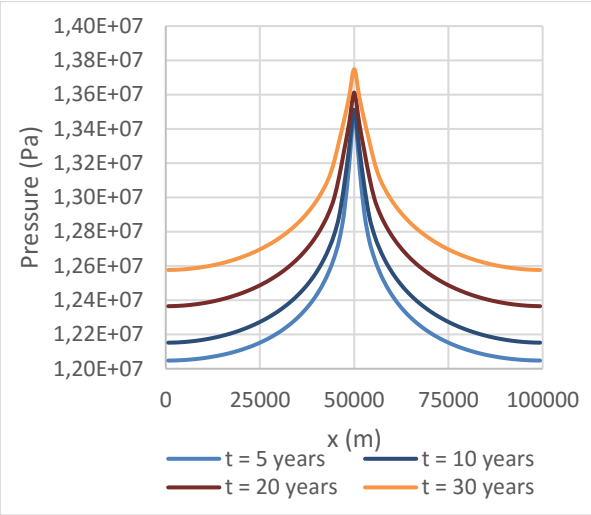

Figure 5.26 – Pressure distribution for k = 500 mD

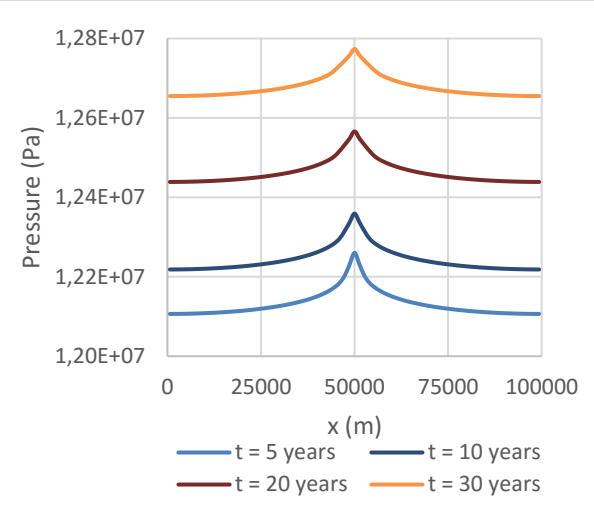

Figure 5.27 – Pressure distribution for k = 5000 mD

The sharpest pressure profile was seen for the lowest permeability case (50 mD) (Figure 5.25), and the perturbation advanced towards the neighbouring grid elements with a simultaneous expansion of the perturbed area. Yet, there were no major pressure rises at the aquifer borders and wellblock.

The perturbation rapidly travelled throughout the aquifer for the 5000 mD case (Figure 5.27), triggering a global pressure increase. Characteristics of both extreme cases were grasped for the intermediate case of 500 mD (Figure 5.26), where a piercing pressure profile, similar to the 50 mD case, was observed for the earlier years but, unlike it, there was a fast perturbation spread, visible at the aquifer boundaries. As the rate of pressure growth at the boundaries was greater than at the centre, a simultaneous flattening of the pressure profile occurred.

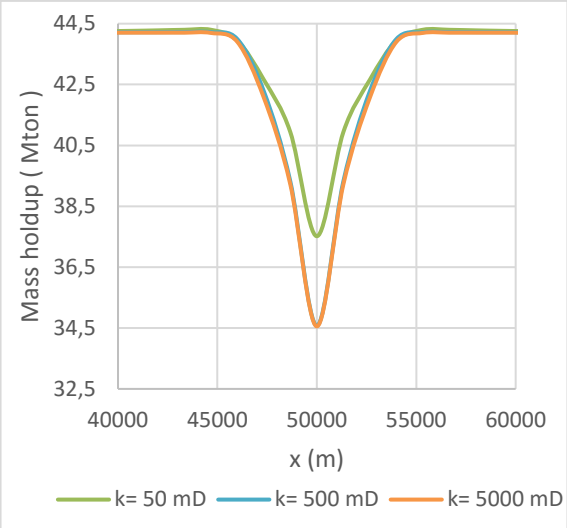

Figure 5.28 – Liquid-phase mass holdup distribution for t=10 years

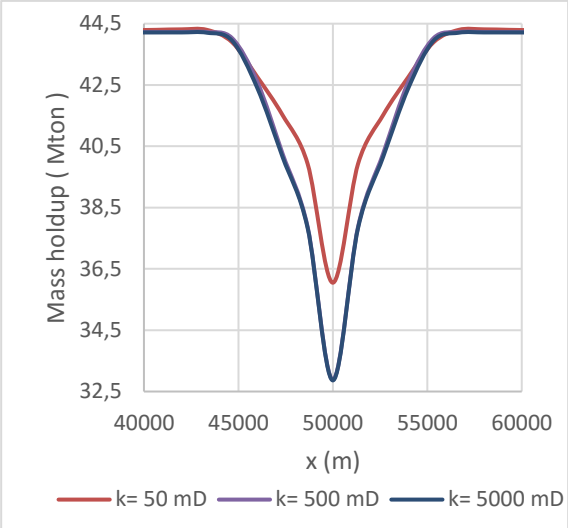

Figure 5.29 – Liquid-phase mass holdup distribution for t=20 years

Figure 5.28 and Figure 5.29 showed a decline of the liquid-phase mass holdup at the wellblock position. The profile widening confirms the movement of water to the surrounding grid elements and, the additional decline of the holdup at the wellblock position, the replacement of the water by the CO_2. The accumulation is noticeably superior for the 50 mD case once, as already referred, there is a greater resistance to flow. However, to distinguish the higher permeability cases and study the wellblock adjacent area occupancy story, a narrower range of the distribution was assessed (Figure 5.30 and Figure 5.31).

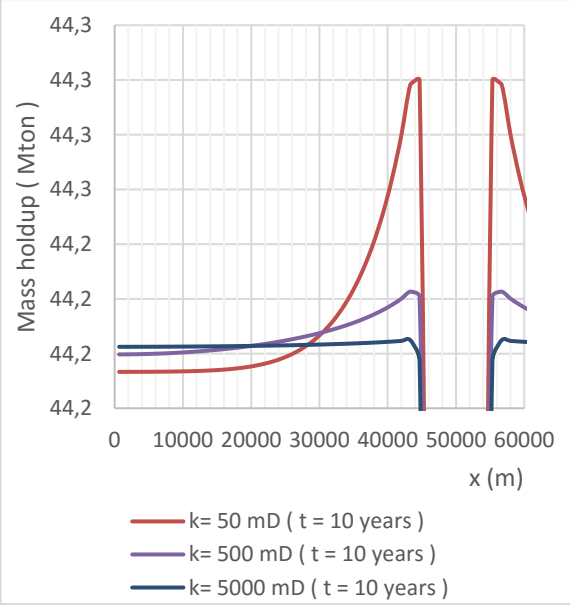

Figure 5.30 – Liquid-phase mass holdup narrower range distribution for t=10 years

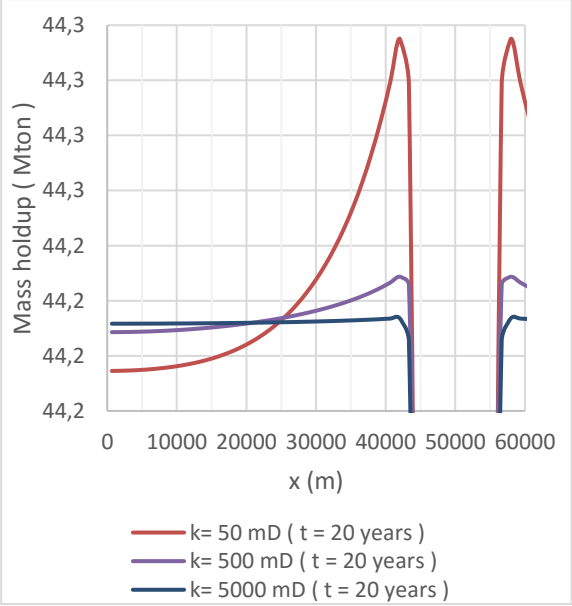

Figure 5.31 – Liquid-phase mass holdup narrower distribution for t=20 years

In addition to the water retention in wellblock being superior, as predicted by the pressure distributions, there is a manifest preferential water accumulation at its vicinity for the lowest permeability case. After 10 years of injection, 44.3 Mton are seen at x=44.667 km, decreasing with the distance from the wellblock to 44.2 Mton. Although there is an expansion of the pointed area towards the boundaries, after 20 years, the mass holdup remains essentially unaffected at x=10 km. Furthermore, the liquid-phase is uniformly distributed for the highest permeability case, with plateaus of 44.20 Mton and 44.21 Mton for t=20 years and t=10 years, respectively. Less marked than the lowest permeability profiles are the intermediate case mass-holdup distributions. Once again, in consequence of the decline of the mass of liquid occupying the wellblock region, a global rise is acknowledged. To finish this analysis, the liquid-phase mass fluxes will be studied, choosing the east face of the wellblock, Figure 5.32.

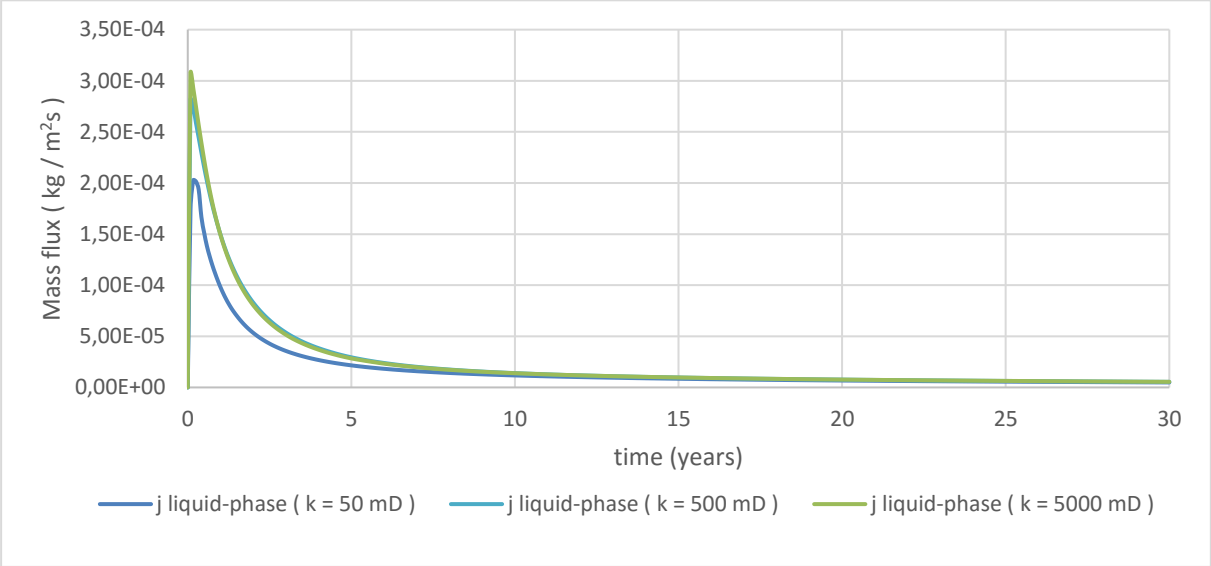

Figure 5.32 – Mass-fluxes at x-direction at east-face of wellblock for permeability sensitivity analysis

Two distinct tendencies were recognised at the wellblock liquid-phase mass fluxes. A sudden rise took place at the first year, for which considerably superior fluxes were attained by the greater permeabilities simulations. Therefore, fast global upsurges of the water mass holdup and pressure were seen for the 500 mD and 5000 mD cases. After reaching the maximum, a smooth decrease of the mass fluxes followed, starting to converge around the 10th year. For the gas-phase, the permeabilities cases studied gave rise to equivalent fluxes, with the mass flowrates leaving the wellblock adding up to approximately 95 kg/s after 10 years, and 98 kg/s after 30. Since 100 kg/s of CO_2 are injected at the wellblock, the mass fluxes nearly reached the steady state. The mass fluxes stabilization observed for both phases confirms the dislocation of the perturbation towards the surrounding grid elements.

5.2.3. Model applicability

To test the applicability of the model, characteristics of the injection sites of the most relevant industrial scale projects where employed in the simulations, one of which has already been demonstrated commercially, the Sleipner Injection Project. The main characteristics of these sequestration sites are summarized in Table 5.11.

Table 5.11 – Injection projects sequestration sites characteristics (after [36])

Project name	**Aquifer depth [m]**	**Permeability [mD]**	**Porosity**	**Aquifer thickness [m]**	**Lithology**
Snohvit	2550	450	0.13	60	Sandstone
Sleipner	1000	5000	0.37	250	Unconsolidated sandstone
Gorgon	2300	25	0.2	500	Sandstone, siltstone

The knowledge of the basins initial pressures and temperatures is essential to determine the physical properties of the fluids. Therefore, once the study did not provide data on the pressure and temperature regimes installed at these aquifers, to estimate them, the depths of the formations were employed and some assumptions made. Based on previous works [28]., the initial pressures were estimated assuming a hydrostatic pressure gradient of 100 bar per kilometre and, the reservoir temperature, with an average temperature gradient of 30 ºC per kilometre. As for the average land surface conditions, the values of 5 ºC and 1 bar were assumed. Table 5.12 displays the estimated values.

Table 5.12 – Injection flowrates, reservoir temperature and initial pressure estimates

Project name	Temperature (ºC)	Initial pressure (bar)	CO_2 injection rate [kg/s]
Snohvit	81.5	256.0	23.1
Sleipner	35.0	101.0	32.4
Gorgon	74.0	231.0	115.7

The remaining settings, common to all simulations, are summarized in Table 5.13. Using the same approach as other studies of CO_2 injection modelling ([32], [35]), van Genuchten correlation was employed to compute the relative permeability. Even though, for some projects, multiple wells are required (Gorgon includes 8 points of injection [36]), here single well injections will be performed for comparison. The wellblock pressure obtained for the simulations of the CO_2 injection projects is displayed in the Figure 5.33 to Figure 5.35.

Table 5.13 – Injection projects simulations specifications

Physical properties	Multiflash	
Simulation time (seconds)	60 x 60 x 364 x 24	
Injection time (years)	30	
Relative permeability correlation	van Genuchten	
	Irreducible liquid saturation	0.2
	Irreducible gas saturation	0.05
	m	0.46
Media deformability	Pressure dependant	
	Pore compressibility (Pa^{-1})	4.50E-10
Grid configuration	N_x x N_y (elements)	75 x 75
	(x_{well} , y_{well})	(38, 38)
Extension in x and y directions (km)	100	

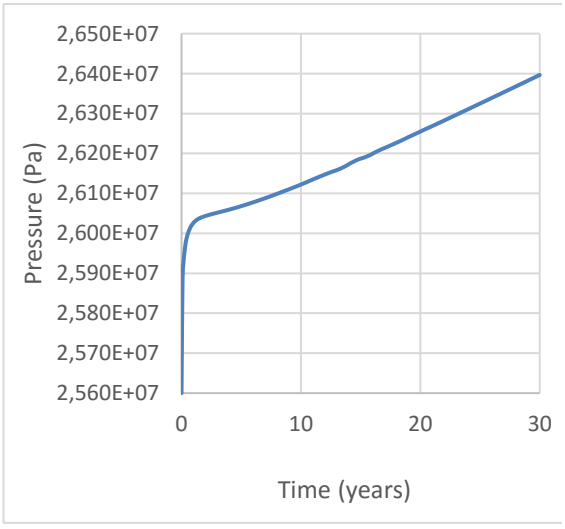

Figure 5.33 – Wellblock pressure for Snohvit project

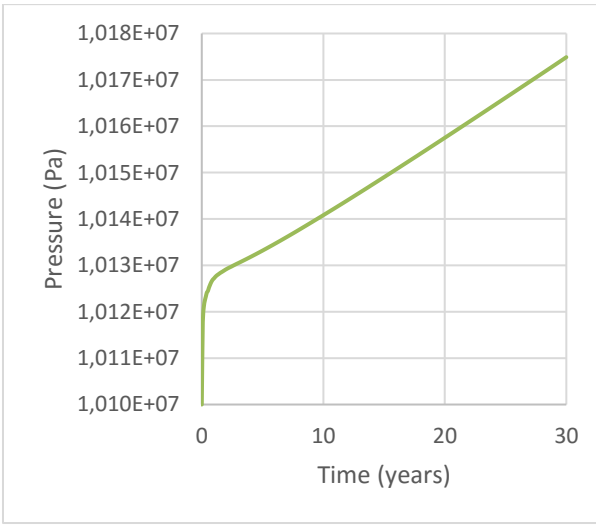

Figure 5.34 – Wellblock pressure for Sleipner project

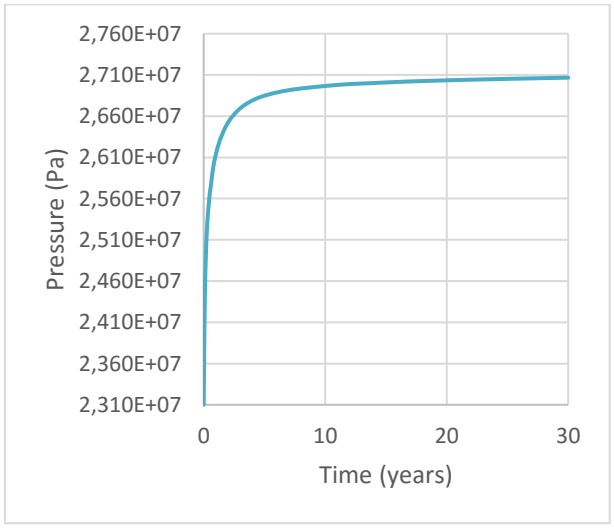

Figure 5.35 – Wellblock pressure for Gorgon project

The initial pressure increase resulting from the injection into Sleipner, Figure 5.34, is about 0.3 bar and, after 30 years of injection, around 0.75 bar, being much smaller than the other projects tested. This injection site has the most suitable characteristics for storing CO_2, the highest porosity and, more importantly, a considerable thickness and permeability and hence the small pressure increase observed. In fact, the results are consistent with a previous study, which previewed no build-up during the first 25 years of the project life [11].

The Snohvit project injection site own the smallest porosity of the investigated formations. Nevertheless, its large permeability underlies the small wellblock pressure increase, of only 1.7% in the first year and 1.4% in the remaining. As for the Gorgon project, its permeability is quite small, 25 mD, but the formation thickness, 500 m, makes it appropriate for injection. The overall pressure increase is the biggest, 17.2% higher than the initial value.

Until now, the mass flowrate relation to the number of injection wells has not been referred, nevertheless, there is a direct relation between both. A large number of wells can help to sustain the continuous injection of large quantities of CO_2 even in low permeability aquifers without exceeding the fracture pressure of the rock. Thus, Gorgon is planning to inject from 8 wells. To investigate the multiwell effect on the pressure build up, this scenario was also tested, using the same settings as the previous simulations (Table 5.13), with the mass flowrate of injection being now distributed evenly between the 8 wells. The chosen grid characterization is displayed in Table 5.14 and the wellblock pressures resulting from this scenario is displayed on Figure 5.36.

Table 5.14 – Gorgon project multiwell injection simulations settings

Grid configuration	N_x x N_y	100 x 100	elements	
	($x_{well}(1)$, $y_{well}(1)$)	(25,25)	($x_{well}(5)$, $y_{well}(5)$)	(50,65)
	($x_{well}(2)$, $y_{well}(2)$)	(25,50)	($x_{well}(6)$, $y_{well}(6)$)	(75,25)
	($x_{well}(3)$, $y_{well}(3)$)	(25,75)	($x_{well}(7)$, $y_{well}(7)$)	(75,50)
	($x_{well}(4)$, $y_{well}(4)$)	(50,35)	($x_{well}(8)$, $y_{well}(8)$)	(75,75)

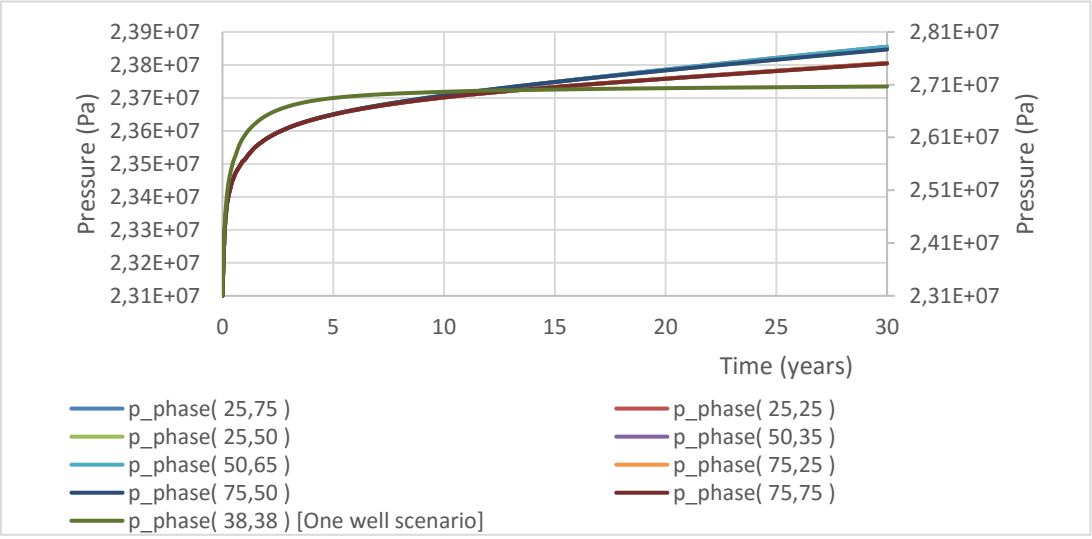

Figure 5.36 – Wellblock pressures for multiwell and one well (right axis) scenarios of Gorgon injection project

A substantial decrease of the wellblock pressure was achieved with the multiwell scenario. The highest pressures were attained at the inner wells, as it can be seen in the pressure distribution (Figure 5.37). For these wells, the pressures were 12% inferior to the one well scenario. In consequence of the scattered well positioning, there is a manifest pressure increase at the boundaries for the multiwell scenario and the extent of the distressed area is far larger in comparison with the one well pressure distribution (Figure 5.38). However, analogously to the one well scenario, conical pressure distributions were shaped around each well and, from the interaction between them, and upsurges are seen at the encompassed zone.

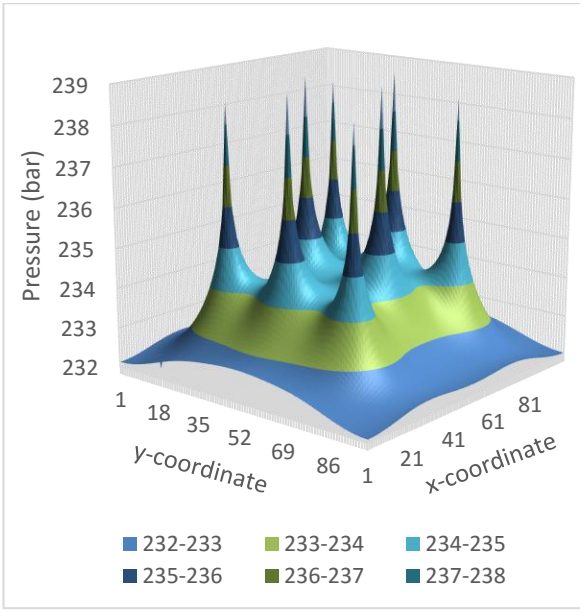

Figure 5.37 – Pressure distribution (t = 30 years) for multiwell scenario of Gorgon project

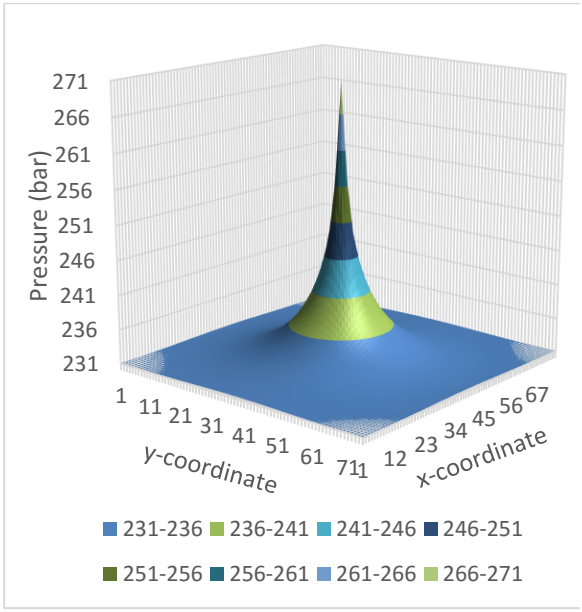

Figure 5.38 – Pressure distribution (t = 30 years) for one well scenario of Gorgon project

The simulations performed for the injection projects were successful in demonstrating the model applicability, being flexible when it comes to number and positioning of wells, range of permeabilities and porosities, giving rise to coherent results. Adversely, the saline aquifer model is not appropriate to simulate the injection into aquifers with small permeabilities and thickness such as the In Salah Project sequestration site, for which the low injectivity (0.145 D.m) requires the injection to be performed from horizontal wells.

6. Modelling a CCS transportation and storage chain

In the present chapter, the injection chain of the Kingsnorth Carbon Capture & Storage Project will be studied, employing the models comprised in the gCCS libraries and the developed model of a saline aquifer. The scope focuses on the confrontation of the planned Full-flow injection flowrate (26400 tonnes/day) against the facility design constraints.

6.1. Kingsnorth case study description

E.ON UK considered a new state of art coal fired power plant at Kingsnorth fitted with CCS for a future investment. Figure 6.1 shows a schematic of the CCS System, where the compressed and cooled carbon dioxide will follow a proposed route comprising a 7.6 km onshore pipeline from the power station to the shoreline and will be connected to an offshore pipeline of approximately 270 km long that leads it to the Hewett offshore platform. From there, the CO_2 will be driven to the well system and to its final destination, the sequestration site.

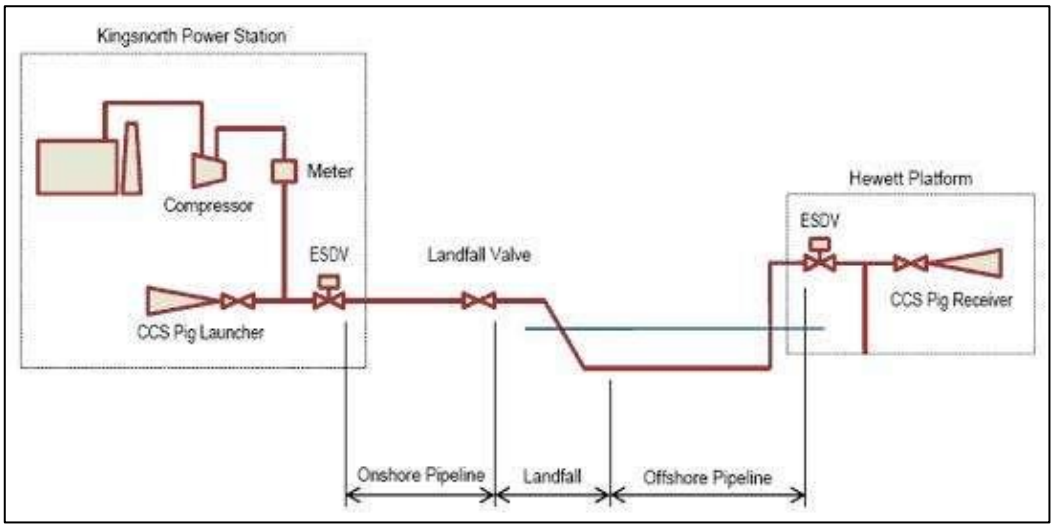

Figure 6.1 – Kingsnorth CCS System Schematic (after [37])

Two main cases were addressed on this project, with a gaseous phase CO_2 being handled at the Demonstration or Base Case scenario and, as a result of the anticipated stepwise growth in transport volumes, a Dense phase operation Case (4 x Demonstration flowrate). The base case encompasses a single platform to handle the gaseous phase CO_2 with a well capacity of 3 wells to handle 6600 tonnes/day, the equivalent flowrate produced onshore when generating 400 MW (gross). For the Full flow dense-phase case, a total of 12 wells are projected to accommodate the 26400 tonnes/day of CO_2. Both cases assume that the flow is to be distributed evenly between the wells so that the flow to a single one amount to 2200 tonnes/day.

The operating conditions must ensure that no 2 phase flow is present in the pipelines, being either gas or dense phase conditions. The base case assume operation in a low pressure (LP – gaseous phase) mode up to a maximum inlet pressure of 39 barg to avoid operating in the two-phase region, switching to high pressure (HP – dense phase) mode with a minimum operating pressure of 79 barg.

The onshore pipeline will run underground and will be uninsulated except for pipeline protection. It will have a design pressure of 150 barg and a design temperature range of minus 85 to 70°C. As for the offshore pipeline, it will be uninsulated except for pipeline protection and weighting purposes and will also have a design pressure of 150 barg. The design temperature ranges of minus 85 to 70°C for the first 20 km from Kingsnorth, then it changes to a design temperature range of minus 85 to 50°C for the remainder of its length.

Once the pipelines are to be upgradeable to cope with both flowrate cases and also, due to the fact that the saline aquifer model was built aiming to simulate the injection of a dense phase CO_2, the HP (dense phase) scenario will be studied here, with special focus on the design constraints of the pipelines.

6.2. Case Study Implementation

The implementation was done in accordance with the Process Flowsheet Diagram (PFD) of the Offshore & Transport System for the Base Case [38] resorting to gCCS Transportation, and gCCS Injection and Storage libraries models. The developed model of a saline aquifer was also included at the flowsheet as the final destination of the captured CO_2. The flowsheet was divided in two sections (Figure 6.2):

i. Transportation, comprising the main onshore and offshore pipelines (Figure 6.3);
ii. Injection/Storage, consisting on the well system and reservoir (Figure 6.4).

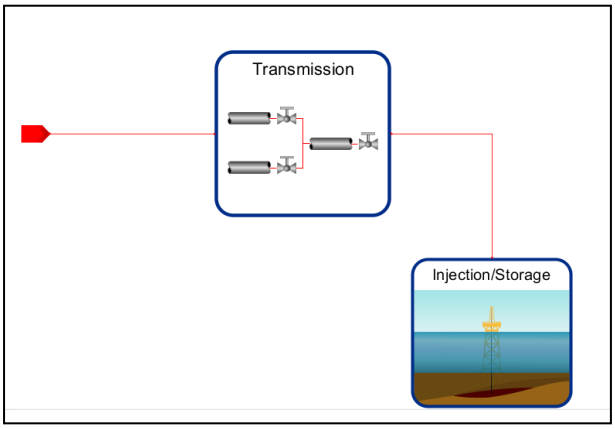

Figure 6.2 – Transmission and Injection/Storage Sections flowsheet

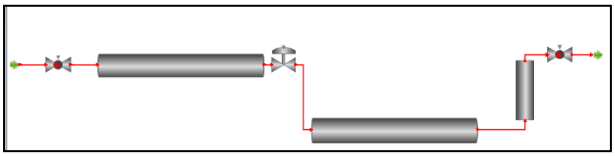

Figure 6.3 – Transmission Section flowsheet

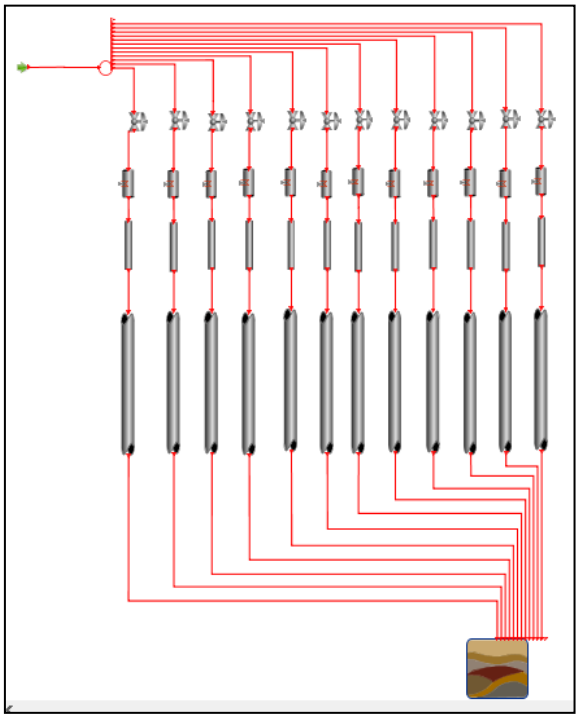

Figure 6.4 – Injection/Storage Section flowsheet

The description of the gCCS libraries models that where employed at the flowsheet implementation and its main assumptions and characteristics can be found at Appendix A. To specify the models, documentation related to the Kingsnorth project was consulted ([38], [39]). The indicative

topographies considered for the pipelines hold a special value, Figure A.1 and Figure A.2., given the fact that they are expected to withhold a strong influence on the properties profiles.

The specifications for the saline aquifer model simulations, were based on injection characteristics of the Kingsnorth project and petrophysical properties of the geological formation intended for sequestration and can be found at Table 6.1. Table 6.2 shows the grid configuration for the aquifer, chosen in order to minimize the interaction between them and the aquifer boundaries.

Table 6.1 – Saline aquifer specifications for the Case Study simulation

Physical properties Calculation	Multiflash	
Injection time	10 years	
Relative permeability correlation ([37], [39])	van Genuchten	
	Irreducible liquid saturation	0.2
	Irreducible gas saturation	0.05
	m	0.46
Media deformability ([37], [39])	Pressure dependant	
	Pore compressibility	4.50E-10 Pa^{-1}

Table 6.2 – Saline aquifer grid configuration for the Case Study

Extension in x and y directions	100 km
Grid dimension: $N_x \times N_y$	$100\ x\ 100$ elements
($x_{well}(1)$, $y_{well}(1)$)	(20, 20)
($x_{well}(2)$, $y_{well}(2)$)	(20, 50)
($x_{well}(3)$, $y_{well}(3)$)	(20, 80)
($x_{well}(4)$, $y_{well}(4)$)	(35, 35)
($x_{well}(5)$, $y_{well}(5)$)	(35, 65)
($x_{well}(6)$, $y_{well}(6)$)	(50, 20)
($x_{well}(7)$, $y_{well}(7)$)	(50, 80)
($x_{well}(8)$, $y_{well}(8)$)	(65, 35)
($x_{well}(9)$, $y_{well}(9)$)	(65, 65)
($x_{well}(10)$, $y_{well}(10)$)	(80,20)
($x_{well}(11)$, $y_{well}(11)$)	(80,50)
($x_{well}(12)$, $y_{well}(12)$)	(80,80)

The simulation time was set to 10 years in order to estimate the dynamic behaviour of the system without compromising the computational time.

6.3. Simulation results

The figures presented henceforth illustrate the initial results and the ones obtained at the 1st, 2nd, 3rd, 5th, 7th and 10th years of simulation, with the objective of illustrating the gradual development of the

properties profiles results, at the equipment that constitute the injection and storage flowsheet studied (Table A.1 and Table A.2). An evaluation of the results obtained for the equipment that present the greatest interest in the Case Study, the pipelines and the aquifer model, is hereby introduced.

6.3.1. Onshore pipeline results

The onshore pipeline pressure profile holds its initial shape throughout the years, with a global increase of pressure taking place over its entire length, Figure 6.5. At the end of the first year of injection, there is a strong upsurge of the pressure and, afterwards, an almost steady rate of growth is observed.

Although there is a large range over which the pressure varies, the design conditions of 150 barg [40] are secured.

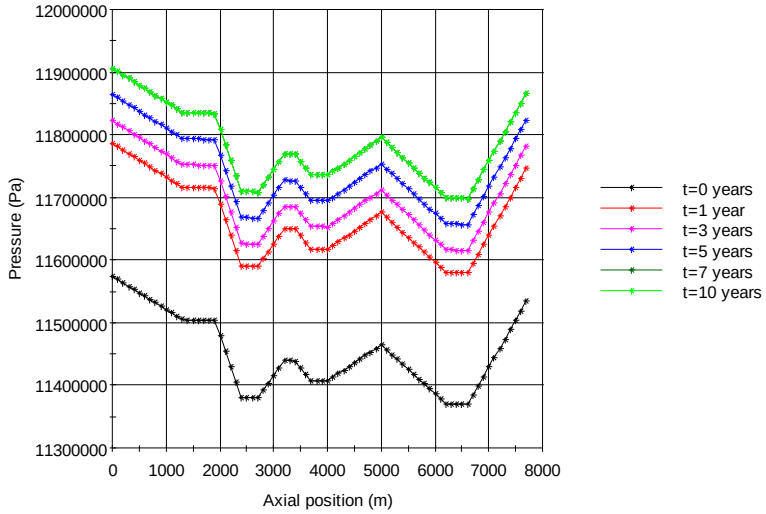

Figure 6.5 – Onshore pipeline pressure distribution

The onshore pipeline temperature distribution shows no major variations, Figure 6.6. Nevertheless, the design conditions of the pipeline, 85 ºC to 70 ºC [40], are fulfilled.

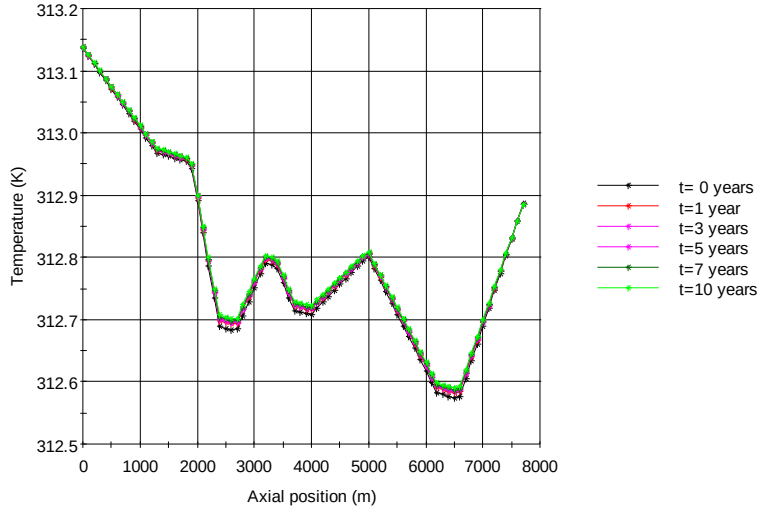

Figure 6.6 – Onshore pipeline temperature distribution

As a result of the system dynamics, the outlet mass flowrate decrease sharply as the simulation begins and the disturbance lasts for about 6 years and a half, Figure 6.7. Nevertheless, the narrow

range of the flowrate variation pinpoints to a minor mass accumulation at the pipeline, with over 305.6 kg/s entering and leaving the equipment.

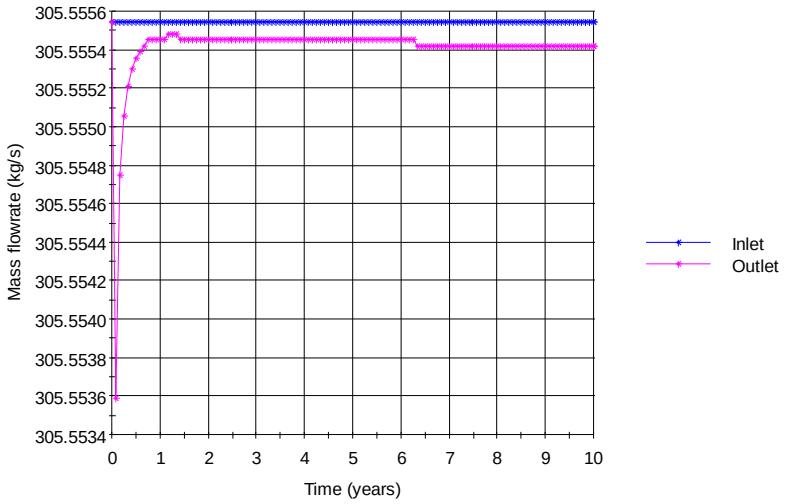

Figure 6.7 – Onshore pipeline inlet and outlet mass flowrate

The fast initial pressure increase seen both upstream and downstream of the pipeline, Figure 6.8, is related to the start-up of the injection and the accompanying reservoir pressure response. This initial response triggers the flowrate behaviour seen at Figure 6.7.

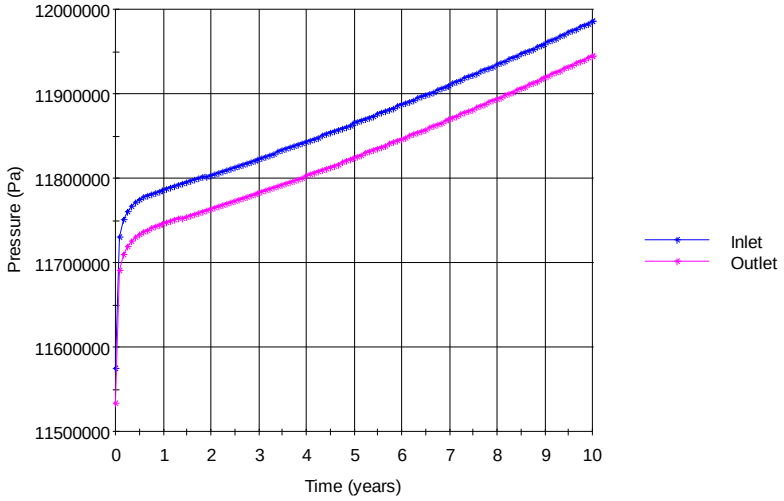

Figure 6.8 – Onshore pipeline inlet and outlet pressure

To finish the onshore pipeline results analysis, the density distribution was accessed, Figure 6.9. It shows that the pipeline meets its operating conditions and the CO_2 flows at a dense-phase as a supercritical fluid. To attain a better understanding of the fluid and flow characteristics studied here, 3D representations of the pressure, density and temperature were created and can be found at A.3.

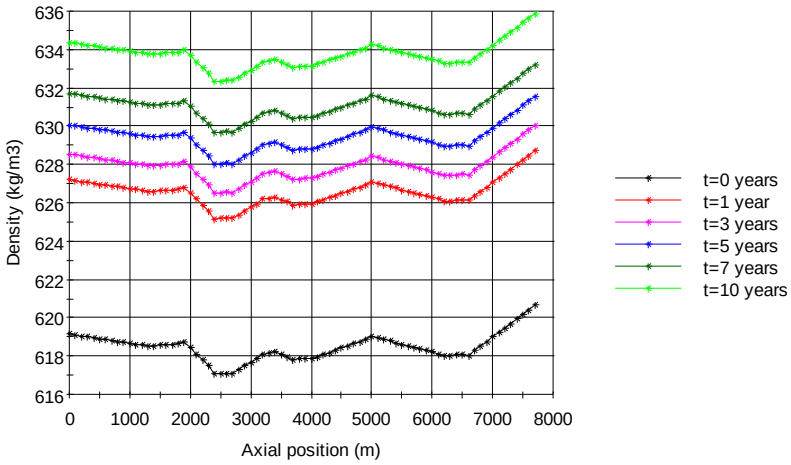

Figure 6.9 – Onshore pipeline density distribution

6.3.2. Offshore pipeline results

The offshore pipeline pressure distribution is showed at Figure 6.10. From its analysis, a similar behaviour to the onshore pipeline is observed, the pressure distribution shape is kept and the pressure increase at different rates. Once again, an abrupt upsurge of the pressure takes place during the first year of injection, and an almost steady rate of increase is recognised for the remaining years.

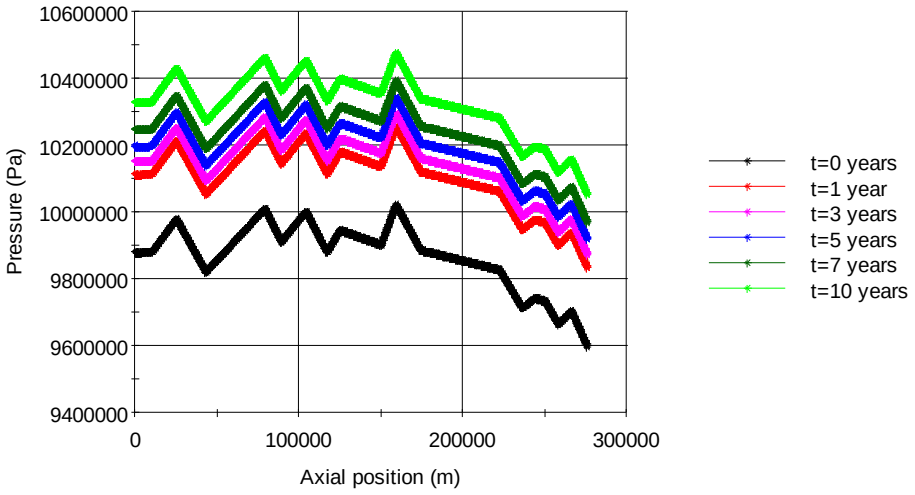

Figure 6.10 – Offshore pipeline pressure distribution

The offshore pipeline temperature distribution does not display major changes throughout the 10 years' simulation, Figure 6.11. Analysing the behaviour lengthwise the pipeline, there is a substantial temperature decline at its entry, Figure 6.12. This happens due to the heat transfer between the flowing CO_2 and the surroundings, the cold seabed water. The heat flux distribution, Figure 6.13, supports this statement by showing a manifest heat loss at the pipeline entry.

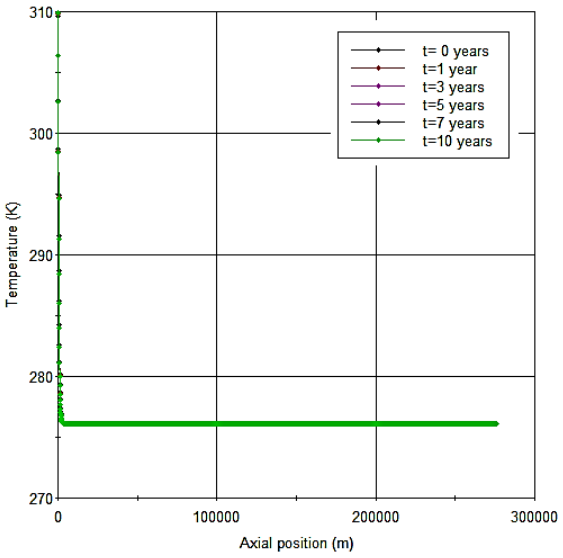

Figure 6.11 – Offshore pipeline temperature distribution

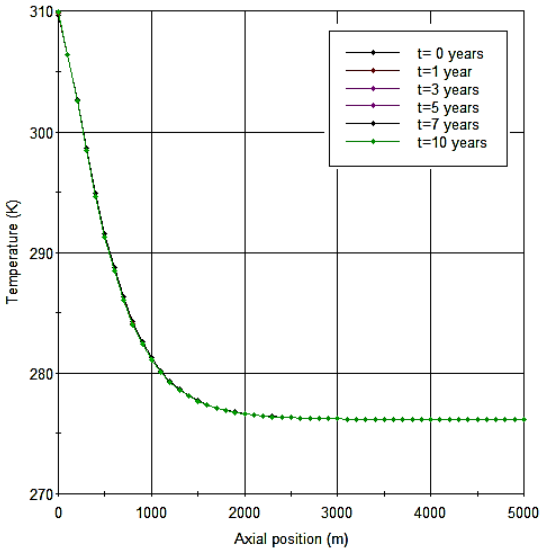

Figure 6.12 – Offshore pipeline entrance temperature distribution

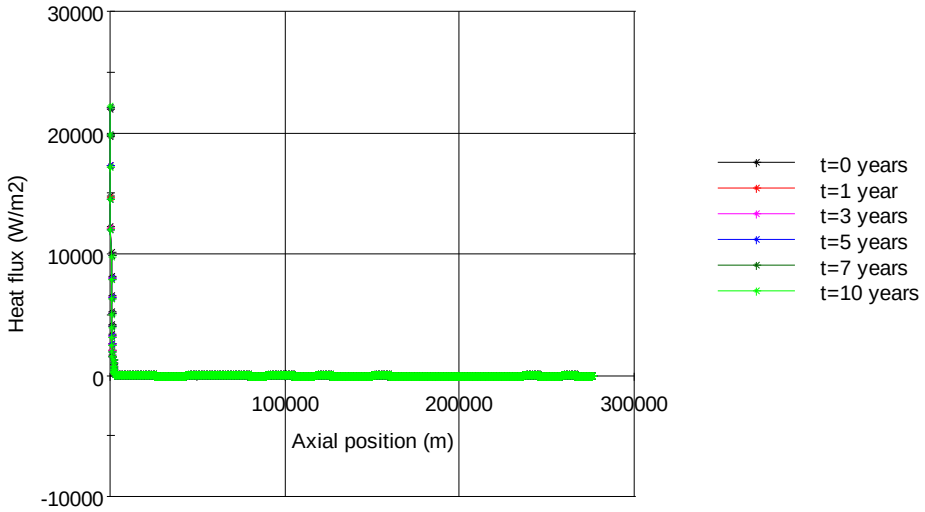

Figure 6.13 - Offshore pipeline heat flux distribution

The offshore pipeline density distribution was accessed, Figure 6.14, showing that the CO_2 arrives at a supercritical state from the onshore section and, due to the considerable temperature decrease at the offshore pipeline entry, Figure 6.12, the CO_2 undergoes a phase change to the liquid state. A study conducted to determine the safe operating conditions of dedicated pipelines for CO_2 transportation implies that while operating under pressurized conditions, no harmful effects are noted on the seal materials of the pipelines [41]. The problem would occur if the system was rapidly depressurized.

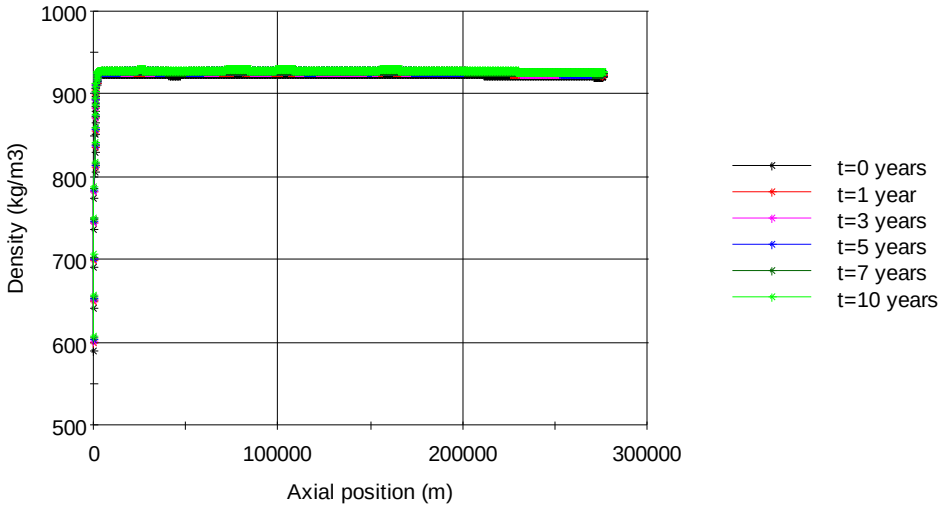

Figure 6.14 – Offshore pipeline density distribution

Finally, the offshore pipeline mass flowrate, Figure 6.15, experiences a similar behaviour to the onshore. The inlet flowrate is not only affected by the upstream but also by the downstream equipment, as it would be expected on a study of a dynamic CCS chain with different injection points. In this case, it is represented by a steep initial decrease at both inlet and outlet mass flow rates. 3D representations of the pressure, density and temperature plots of the offshore pipeline can be found at A.3.

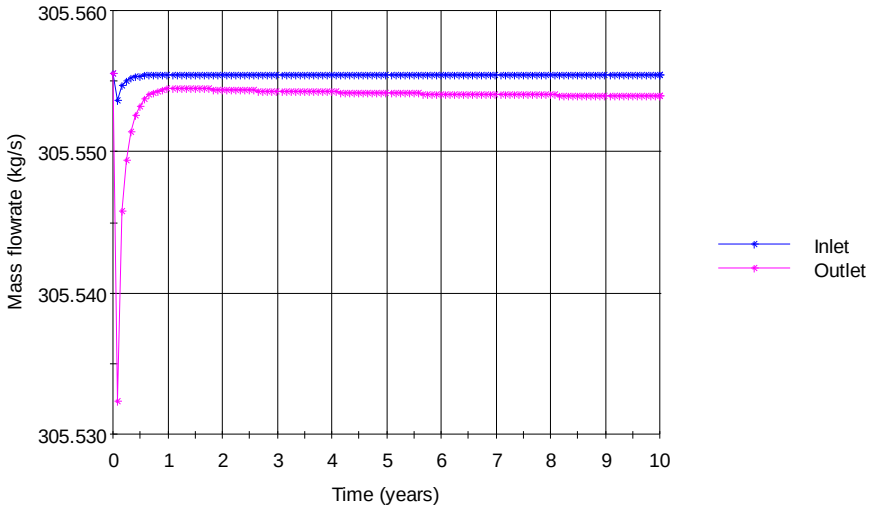

Figure 6.15 – Offshore pipeline inlet and outlet mass flowrate

6.3.3. Saline aquifer results

As referred above, the wells configuration, chosen to minimize their interaction, can be found at Table 6.1. This expected interaction is seen here though, as illustrated by representation of the inlet pressure at each injection point (Figure 6.16).

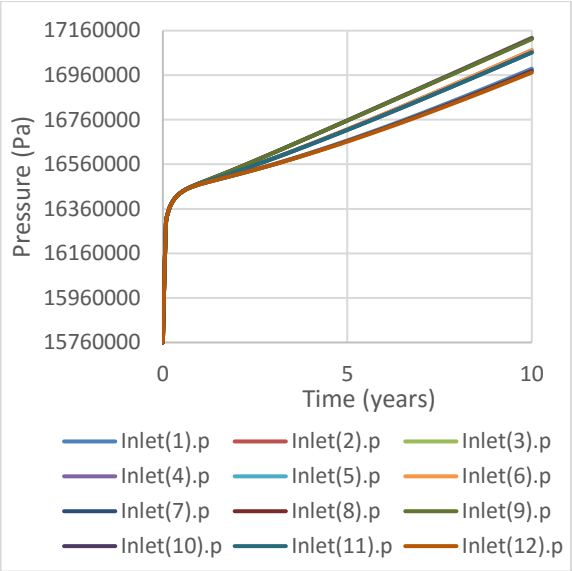

Figure 6.16 – Saline aquifer inlet pressures

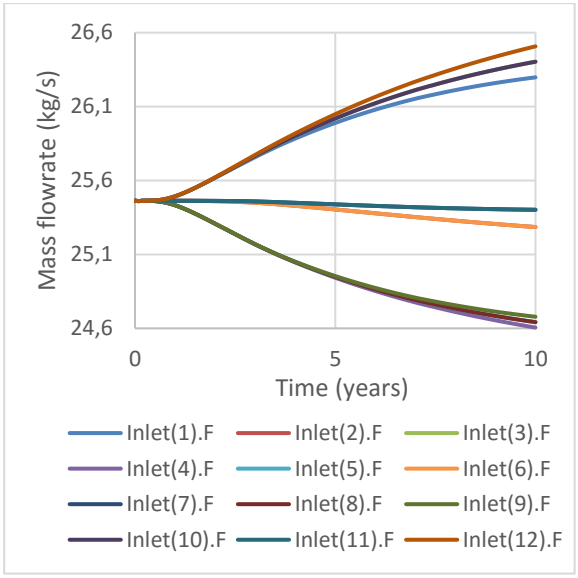

Figure 6.17 – Saline aquifer inlets mass flow rates

In response of the observed difference in pressure development at each wellblock, the inlet mass flow rates diverge, Figure 6.17. For the purpose of monitoring the pressure distribution at the aquifer, its representation after the 1st year of injection is shown on Figure 6.18. Once the initial reservoir pressure was set to 158 bar, at this time, the response to the injection is mainly felt at the well coordinates and surrounding grid elements at first, with a smaller pressure increase being felt at the points further apart from the well coordinates.

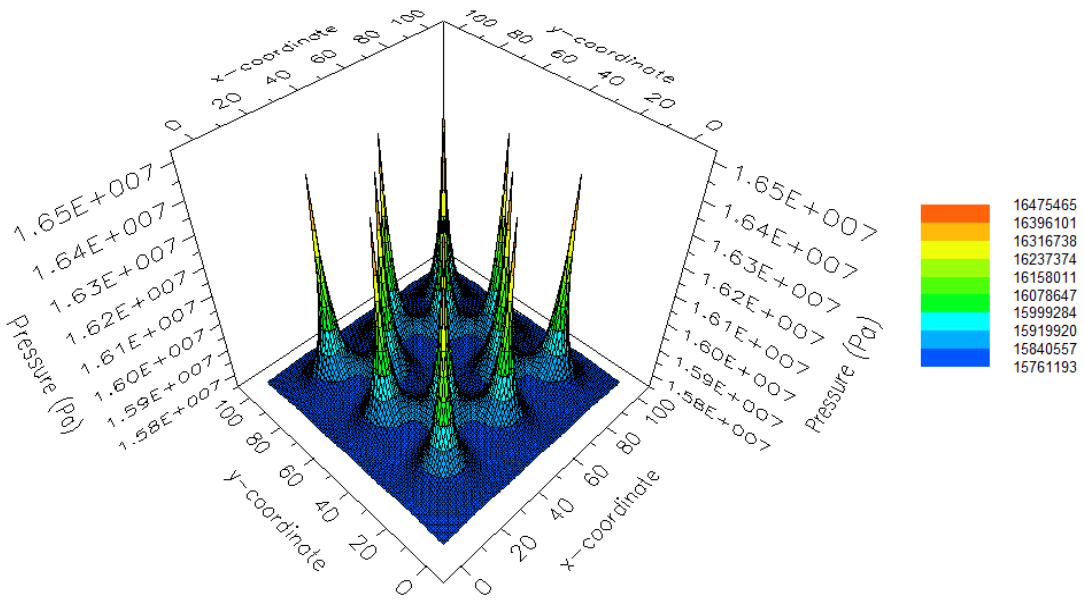

Figure 6.18 – Saline aquifer pressure distribution for t=1 year

By the end of the 10th year, the reservoir pressure already exhibits an increase of about 4 bar at the points far-off removed from the well coordinates, Figure 6.19. Representation of the pressure distribution at the aquifer at the end of the 2nd, 5th, and 8th year can be found at A.3.

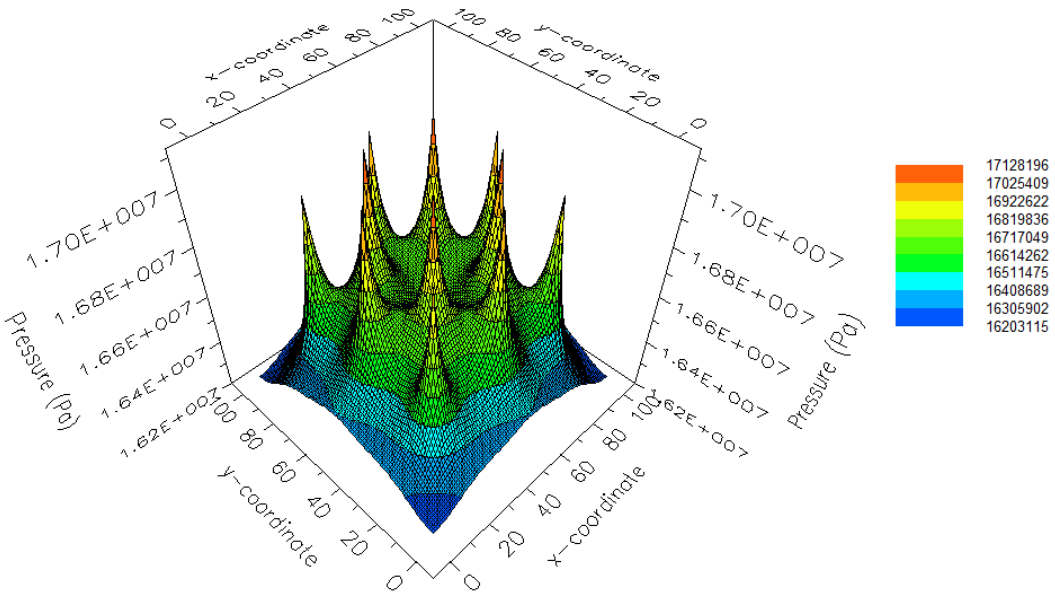

Figure 6.19 – Saline aquifer pressure distribution for t = 10 years

7. Conclusions

On the present work, a model of a Saline aquifer was developed, meeting the objective of foreseeing the effect of the CO_2 sequestration on the existing pressure regimes of these geological formations. A 2D Cartesian x-y model of a saline aquifer was developed in the gPROMS model builder platform, taking advantage of its advanced mathematical capabilities to solve the derived equations of the multiphase flow in porous media. The mathematical formulation of the Aquifer model comprised some assumptions so that a practical tool in answering questions related to the operations of a CCS chain was developed. The assumptions introduced included vertical equilibrium, neglecting non-isothermal and the chemical reactions effects.

With the developed model, injection studies into water saturated aquifers were performed, with the inlet stream of CO_2 being considered pure and at supercritical dense state. The model developed is successful in simulating the continuous injection of large volumes of CO_2 into saline aquifers.

The multiphase flow in the porous media was defined and thoroughly studied by application of the Darcy's law extension to the multiphase flow in porous media. To calculate the ease of movement of the fluid-phases that occupy the porous media simultaneously, namely the CO_2 (gas-phase) and the water (liquid-phase), different sets of relative permeability correlations were implemented. Those included the Corey and van Genuchten correlations, the most popular correlations employed at reservoir simulations.

By studying the Corey and van Genuchten relative permeability curves, it was possible to enlighten various aspects of its influence on the movement of the phases, and the respective changes in the pressure regimes over the whole aquifer extent, supporting their popularity on describing the multiphase flow in several reservoir simulations. The physical properties package Multiflash was used. Also, in order to expand the model applicability, other methods of calculation/estimation of physical properties were implemented, including literature correlations and interpolation of existing data.

A study of the simulations of the CO_2 sequestration, performed with a detailed geological model of the Johansen deep saline aquifer, located at the Norwegian North Sea, was utilized as an evaluation basis for the model. The petrophysical properties of the formation and the characteristics of the injection project were adapted to be used in the saline aquifer model simulations.

For the considered injection scenario of the Johansen formation, a fair degree of consistency was achieved. The pressure development trends were comparable for all cases of relative permeability studied, but the initial transient responses of the aquifer to the injection of CO_2 were less marked than the ones seen at the ECLIPSE results. It is believed that the grid refinement is the key player on the accuracy of the results and capture of the transient response on the first years of injection.

The wellblock pressure obtained at the end of 80 years of CO_2 injection, predicted by the simulations where Corey correlation was used to describe the relative permeability of the liquid phase, is in agreement with the range predicted by the Eclipse simulations. For these simulations (Cases 1 and 4), the final result deviates only 0.14% from the value predicted by the detailed geological model with the no-flow boundaries condition, the same boundary condition utilized in the model mathematical description. When van Genuchten correlation was employed to represent the liquid-phase relative

permeability, the correlation with the poorest fit to the detailed model data, the pressure was overestimated in about 8 bar.

The porosity sensitivity analysis gave rise to wellblock pressures with a rate of growth inversely proportional to the studied porosity values. Also, this study showed that the velocity of propagation of the disturbance set by the injection of CO_2, is as high as the smaller the porosity of an aquifer. As for the permeability sensitivity analysis, differences on the pressure profiles and the expansion of the perturbed area are very substantial. For higher permeabilities, flatter pressure profiles are seen, as a result of the quick perturbation spread and, for higher permeability cases, piercing pressure profiles are attained but no major pressure buildup take place at the aquifer borders.

The saline aquifer model applicability to the CO_2 injection problem was tested, providing a better understanding of the sensitivity of the developed model to the geological parameters: The model allowed effective simulations with several sets of subsurface conditions, reflecting the characteristics of sedimentary basins around the world expected to be CO_2 geological sequestration scenarios.

To finish the study, the aquifer model was successfully evaluated within a test study of the transmission and injection sections of a new state of art coal fire power plant at Kingsnorth, for which Carbon Capture and Storage (CCS) has been considered. The results obtained showed that the model performs well when introduced into a Flowsheet scenario, allowing the dynamic simulation of the chain. Also, the design constraints of the equipment included at the flowsheet, were met.

The model developed at the present thesis showed a good compromise between simplicity and performance, and the results strongly indicate that it can be applied to do preliminary studies on the dynamic behaviour of a CCS Transmission and Injection chain. Challenges associated with modelling the CO_2 injection into saline aquifers were assessed and, not less important, when the developed model is integrated into a Whole Chain Case Study situation, it permits the estimation of the power required in the compression section during a CCS project life, helping in the decision of its viability.

A fair tool to estimate practical quantities associated with CO_2 injection was hereby developed, with focus on the pressure buildup in the aquifer and corresponding decline of the ease of injection. Moreover, the model can help on deciding the viability of an aquifer for CO_2 sequestration and on the well-arrangement to perform the injection process.

7.1. Future work

The model hereby developed, tested and evaluated in a case study scenario already includes in its formulation, options for performing more detailed and accurate simulations of the injection. In the phase of development of the model code, simulations specified under these options, required a lot of computational capacity, time and usually giving rise to uncertain results or numerical errors. Therefore, enhancing the mathematical model and enhancing the code would be the starting point for future work. Moreover, the study of the problem definition complexity on the computational effort and simulation time could also be performed. Model improvements could include the heat flux definition by modelling its conductive and convective components and modelling the fluid and heat transfer in the vertical direction.

By refining the ways of defining the grid dimensions or grid spacing, more detailed studies of the effect of grid refinement on the accuracy of the results of the injection into reservoirs could be conducted.

The model allows for the definition of the petrophysical properties of the aquifer to be specified for each block separately, allowing future studies of the heterogeneity of the formation on the pressure regime and CO_2 plume distribution and spread. Another model improvement would be to include a WELL-INDEX to differentiate the pressure of the perforated grid-block and the pressure inside the well.

Although CO_2 solubility in formation water is recognized to be a long-term process, several authors defend that the dissolution of the injected CO_2 in the formation water represent a significant trapping mechanism once the saturating of the formation water with CO_2 could create even greatest CO_2 storage capacities. Therefore, it would be a great development to model the chemical reactions that take place when water and CO_2 occupy the same porous space, i.e. the thermodynamics and thermophysical properties of H_2O–NaCl–CO_2 mixtures. This would enable studies of the long term fate of the sequestered CO_2, the effect of the formation water composition, CO_2 impurities and the effect of the dissolution on the storage capacity. Another interesting study would be the inclusion of the reactions of the CO_2 with the formation rock and caprock minerals, the production of carbonate minerals, and the accompanying decrease of the porosity and permeability.

Bibliography

[1] IPCC, “Climate Change 2007: Synthesis Report, contribution of Working Groups I, II and III to the fourth assessment report of the Intergovernmental Panel on Climate Change,” IPCC, Geneva, Switzerland, 2007.

[2] M. Ghommem et al., “Influence of natural and anthropogenic carbon dioxide sequestration on global warming,” *Ecological Modelling,* vol. 235–236, p. 1–7, 2012 June 2012.

[3] H. Herzog, E. Drake and E. Adams, “CO2 capture, reuse, and storage technologies for mitigating global climate change,” Massachussets Institute of Technology, Cambridge, MA, 1997.

[4] IEA, “Technology Roadmap: carbon capture and storage,” IEA, 2009.

[5] IEA, “International Energy Outlook 2007,” Energy Information Administration, Washington, DC, 2007.

[6] S. Bachu, “CO2 storage in geological media: Role, means, status and barriers to deployment,” *Progress in Energy and Combustion Science,* vol. 34, no. 2, p. 254–273, April 2008.

[7] Costas Pantelides, Process Systems Enterprise, *CCS System Modelling Tool-kit Project,* 2012.

[8] “Carbon capture & storage,” 20 07 2013. [Online]. Available: http://www.psenterprise.com/power/ccs.html.

[9] Jason Anderson et al., “IPCC Special Report on Carbon dioxide Capture and Storage: Underground Geological Storage,” Cambridge University Press, New York, NY, 2005.

[10] H. Class, A. Ebigbo, R. Helmig, H. K. Dahle and J. M. Nordbotten, “A benchmark study on problems related to CO2 storage in geologic formations,” *Computational Geosciences,* pp. 409-434, 12 August 2008.

[11] http://faculty.jsd.claremont.edu/emorhardt/159/pdfs/2006/Torp.pdf.

[12] K. C. O. a. G. M. Pruess, “TOUGH2 User's Guide, Version 2.0,” Report LBNL-43134, Lawrence Berkeley National Laborator, Berkeley, California, 1999.

[13] Global CCS Institute, “The Global Status of CCS: 2012,” Global CCS Institute, Canberra, Australia, 2012.

[14] Rodney Allam et al., “IPCC Special Report on Carbon dioxide Capture and Storage: Capture of CO2,” Cambridge University Press, New York, NY, 2005.

[15] Global CCS Institute, “Capturing CO2,” 1 March 2013. [Online]. Available: http://cdn.globalccsinstitute.com/sites/default/files/publications/25896/capturing-co2.pdf. [Accessed 17 April 2013].

[16] Global CCS Institute, “Transporting CO2,” 1 March 2013. [Online]. Available: http://www.globalccsinstitute.com/publications/transport-co2. [Accessed 17 April 2013].

[17] G. de Marsily, Quantitative hydrogeology, Orlando, Florida: Academic Press,, 1986.

[18] J. Forrest F. Craig, The Reservoir Aspects of Waterflooding, New York: Millet the printer, 1971.

[19] X. J. a. J. v. Wunnik, “A Capillary Pressure Function for Interpretation of Core Scale Displacement Experiments,” in *International Symposium of the Society of Core Analysts*, the Hague, 1988.

[20] R. H. Brooks and A. T. Corey, “Hydraulic Properties of Porous Media,” *Hydrology Paper,* no. 3, 1964.

[21] R. H. Brooks and A. T. Corey, “Properties of Porous Media Affecting Fluid Flow,” *Journal of the Irrigation and Drainage Division, Proceedings of the American Society of Civil Engineers (ASCE),* vol. 92, no. IR2, pp. 61-88, 1966.

[22] A. Corey, “The interrelationship between gas and oil relative permeabilities,” *Producers Montly,* vol. 19, pp. 38-41, November 1954.

[23] M. T. van Genuchten, “A Closed-form Equation for Predicting the Hydraulic Conductivity of Unsaturated Soils,” *Soil Sci. Soc. Am. J.,* vol. 44, pp. 892-898, September 1980.

[24] Y. Mualem, “A New Model for Predicting the Hydraulic Conductivity of Unsaturated Porous Media,” *Water resources Research,* vol. 12, no. 3, p. 513–522, 1976.

[25] M. T. Burdine, “Relative Permeability Calculations From Pore Size Distribution Data,” *Transactions of the American Institute of Mining and Metallurgical Engineers,* vol. 198, pp. 71-78, 1953.

[26] Parker, “A Parametric Model for Constitutive Properties Govenning Flow in Porous Media,” *Water Resources Research,* vol. 23, p. 618–624, 1987.

[27] F. M. J. Orr, Theory of Gas Injection Processes, Stanford, California: Tie Line Publications, 2005.

[28] K. Prues, “Modeling Carbon Sequestration in Saline Aquifers,” [Online]. Available: http://www.yale.edu/yibs/sequestration-forum-presentations/Pruess_Yale_Apr06.pdf. [Accessed 25 May 2013].

[29] K. J. W. a. Y. T. Pruess, “On Thermohydrological Conditions Near High-LevelNuclear Wastes Emplaced in Partially Saturated Fractured Tuff. Part 2. Effective Continuum,” *Water Resour. Res.,* vol. 26, no. 6, pp. 1249-1261, 1990.

[30] T. N. a. W. P. A. Narasimhan, “An integrated finite difference method for analyzing fluid flow in porous media,” *Water Resour. Res,* vol. 12, no. 1, p. 57–64, February 1976.

[31] K. a. A. S. Aziz, Petroleum Reservoir Simulation, London and New York: Elsevier, 1979.

[32] G. Bacci, “An Experimental and Numerical Investigation into Permeability and Injectivity Changes during CO2 Storage in Saline Aquifers,” London, UK, 2011.

[33] G. Eigestad, H. K. Dahle, B. Hellevang, F. Riis, W. Johansen and Ø. E. Johansen, “Geological modeling and simulation of CO2 injection in the Johansen formation,” *Computational Geosciences,* vol. 13, no. 4, pp. 435-450, December 2009.

[34] Sintef - MatMoRA project, “The Johansen Data Set,” Sintef, 31 March 2009. [Online]. Available: http://www.sintef.no/Projectweb/MatMoRA/Downloads/Johansen/. [Accessed March 2013].

[35] Zhou Q, et al., “A method for quick assessment of CO2 storage capacity in closed and semi-closed saline formations,” 2008. [Online]. Available: http://esd.lbl.gov/files/research/programs/gcs/projects/storage_resources/journal_3_NETL_zhou_etal_IJGGC.pdf.

[36] A. Hosa, M. Esentia, J. Stewart and R. Haszeldine, “Benchmarking worldwide CO2 saline aquifer injections,” Scottish Centre for Carbon Capture and Storage, 2010.

[37] E-ON UK, *Vertical Flow performance,* E.ON UK, 2012.

[38] E.ON UK, Offshore & Transport System CO2 Process System Demo Phase (Base Case) Process Flow Diagram, 2010.

[39] E. UK, Heat & Mass Balance Demo Phase and Full Flow, 2010.

[40] E.ON UK, *Basis of Design for Studies - Phase 1A,* E.ON UK, 2012.

[41] F. Eldevic, “Safe Pipeline Transmission of CO2,” vol. 235, no. 11, November 2008.

[42] B. Hitchon, “Aquifer Disposal of Carbon Dioxide: hydrodynamic and mineral trapping: Proof of concept,” p. 165, 1996.

[43] R. A. Freeze and J. A. Cherry, Groundwater, Englewood Cliffs: Prentice Hall, 1979.

[44] R. D., “Carbon Sequestration Research and Development,” *U. S. Department of Energy,* 1999.

[45] M. Ahmet, “Properties of reservoir rocks,” April 2013. [Online]. Available: http://www.slideshare.net/sedimentology/properties-of-reservoir-rocks.

[46] In Salah Gas Stockage of CO2, “CO2 STORAGE AT IN SALAH - Injection wells,” MMC Digital, May 2013. [Online]. Available: http://www.insalahco2.com/index.php/en/low-co2-gas-production/co2-transport-a-injection.html. [Accessed 23 March 2013].

[47] Jason Anderson et al., “Carbon Dioxide Capture and Storage: Underground Geological Storage,” Cambridge University Press, New York, NY, 2005.

Appendix A

A.1 Case Study Models description and specification

Table A.1 – Characteristics of the pipe models from the gCCS library used at the Transport Section of the Kingsnorth Case Study

Model	**Function**	**Model characteristics**
PipeSegment	The function of this model is to provide a channel for the flow of CO_2. It is used to simulate both onshore and offshore pipelines.	Dynamic model of a pipe with uniform diameter and axial distribution. Mass, energy and momentum balances are used to calculate the pressure, velocity and temperature profiles. The model is able to represent the entire pipeline, with the topography of each pipe segment. The main assumptions of the model are negligible heat transfer resistance between the pipe material and the fluid and small variations in pipe conditions in the radial direction. Also, the transport properties of the surrounding material are time invariant and estimated using the average ambient temperature.
Vertical Riser	Represents the connection between the offshore pipeline segments and the pipe splitter.	It is an axial distributed model similar to the pipe segment model that allows for topography specification and is grounded in the same assumptions. Also, water is assumed to be the surrounding environment.
Wellhead Connection	Model used to represent the wellhead connections between the offshore platforms and the facilities on the seabed.	Like the Well model, it is a dynamic pipe model similar to the PipeSegment model, also grounded by the same assumptions.
Well	The well model provides the last passage for the CO_2 before it is injected into the reservoir.	Model analogous to the PipeSegment, grounded by the same assumptions and relying on mass, energy and momentum balances across the well to calculate the various properties along the pipe.

Table A.2 – Characteristics of the models from the gCCS library used at the Transport Section of the Kingsnorth Case Study

Model	**Function**	**Model characteristics**
ValveGate	Gate valve model that represents the landfall valve placed between the onshore and offshore pipelines.	The model determines the stream flow rates as a function of the pressure difference and the valve stem position. The main assumptions of the model are isenthalpic expansion and irreversible flow. It does not allow phase changes and the maximum flow through the valve is limited by choked flow.
HeaterCO2	Heat exchanger model used to heat the CO_2 that arrives from the transport section.	The model relates the flowrate and pressure drop through the equipment with a flow coefficient and does not take into account the precise mechanism of heating. It also assumes no heat losses.
PipeSplitter	Model used to split the flow of CO_2 that arrives from the transportation section between each well.	It does not account for heat or pressure losses in the equipment so that the outlet stream has the same composition, temperature and pressure as the original stream.

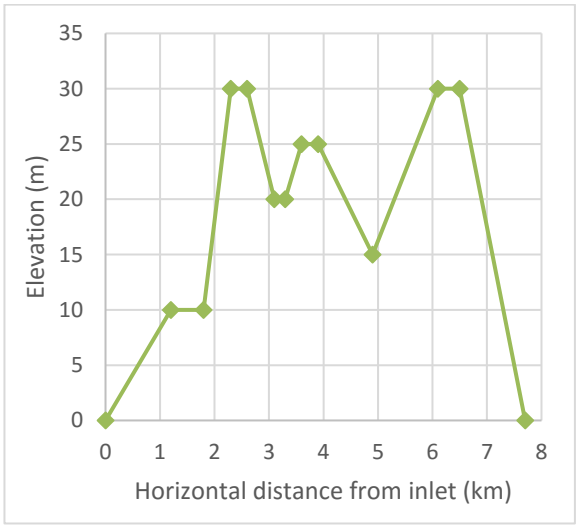

Figure A.1 – Onshore Pipeline Topography (after [40])

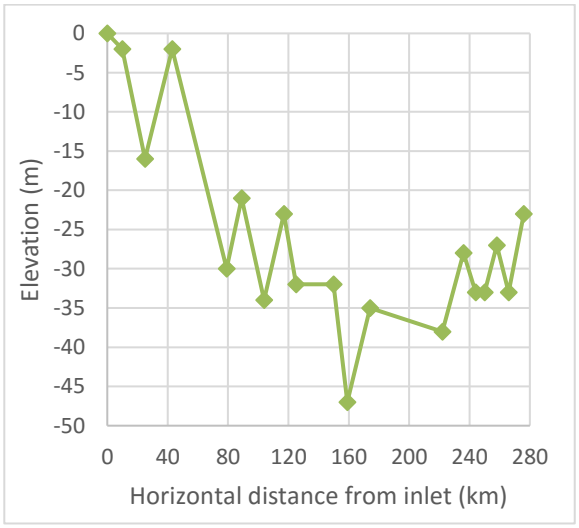

Figure A.2 - Offshore Pipeline Topography (after [40])

A.2 Onshore pipeline 3D plots

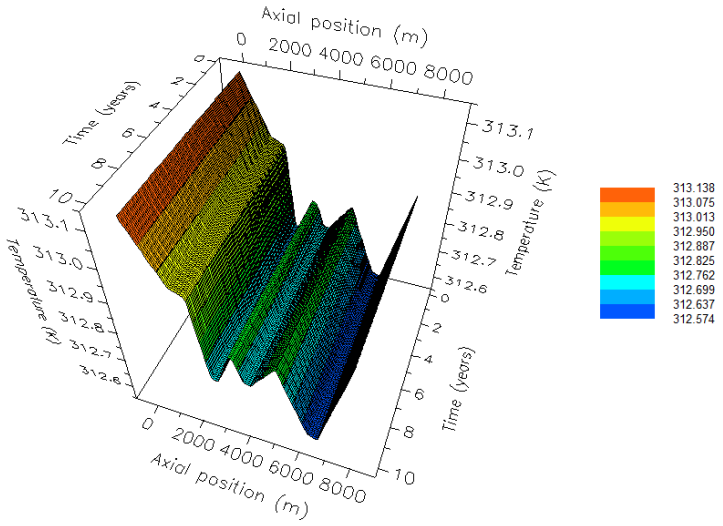

Figure A.3 – Onshore pipeline temperature distribution (3D)

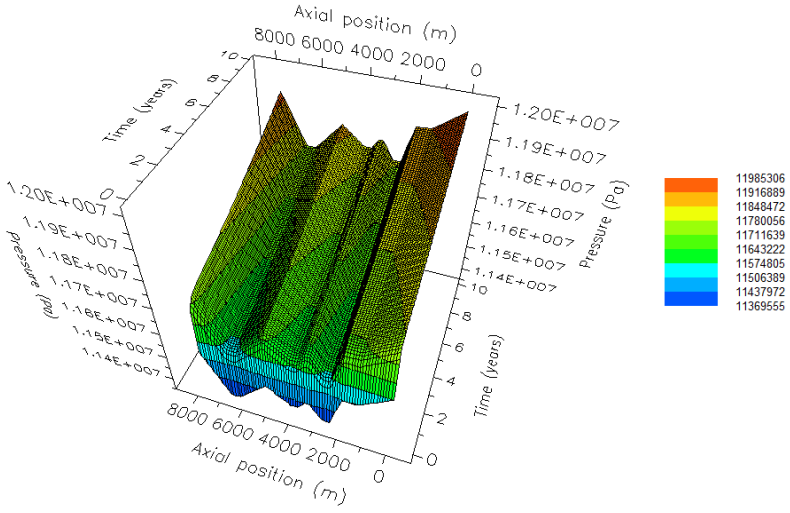

Figure A.4 – Onshore pipeline pressure distribution (3D)

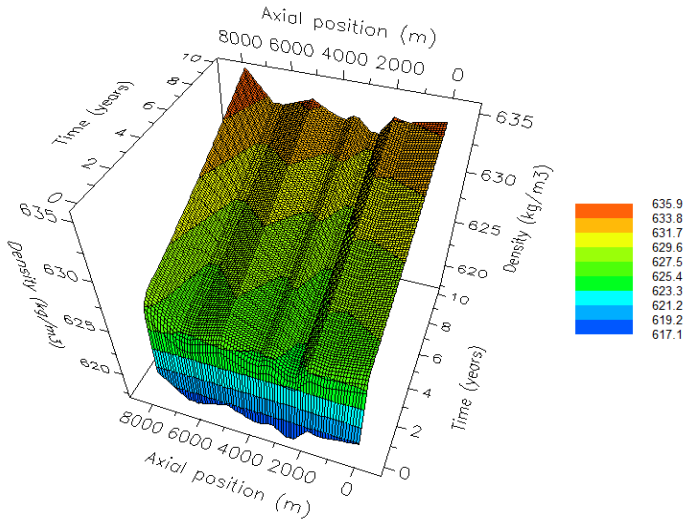

Figure A.5 – Onshore pipeline density distribution (3D)

A.3 Onshore pipeline 3D plots

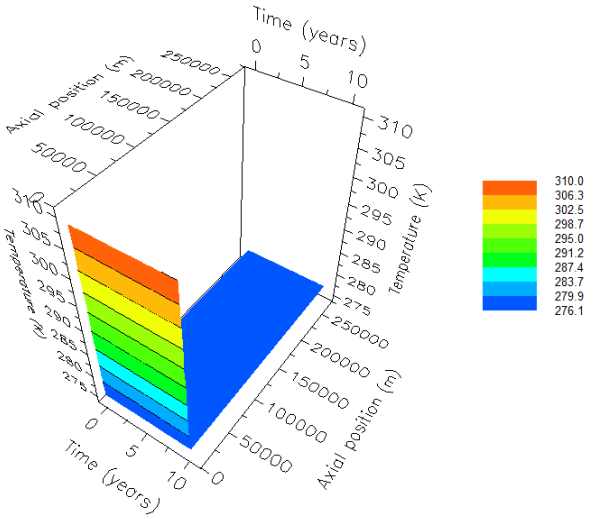

Figure A.6 – Offshore pipeline temperature distribution (3D)

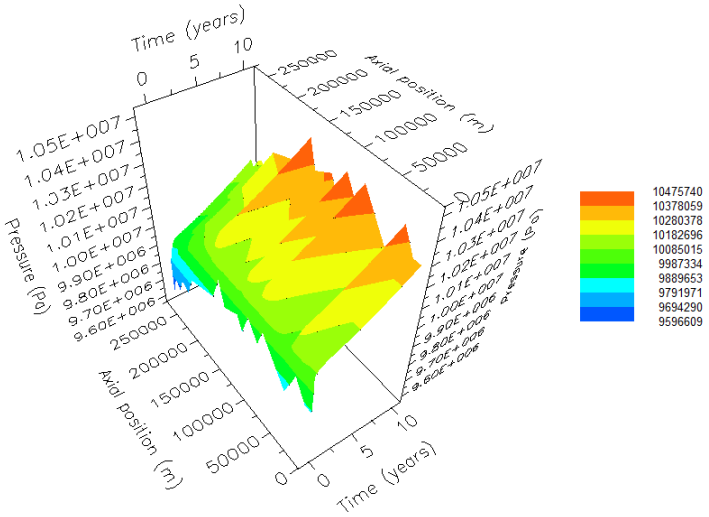

Figure A.7 – Offshore pipeline pressure distribution (3D)

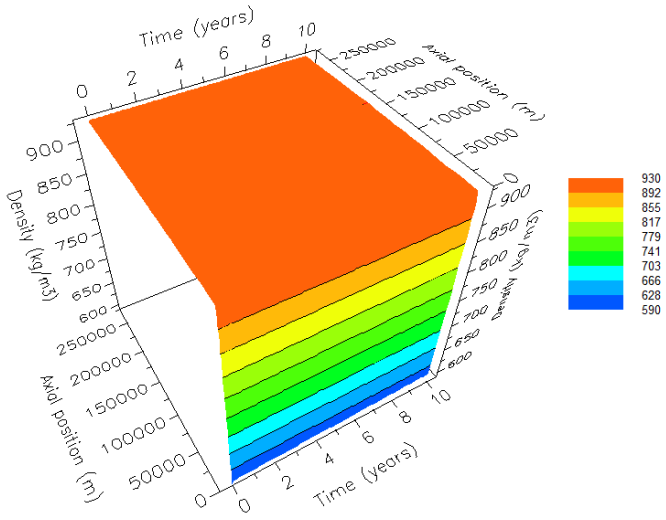

Figure A.8 – Offshore pipeline density distribution (3D)

A.4 Saline aquifer Case Study 3D plots

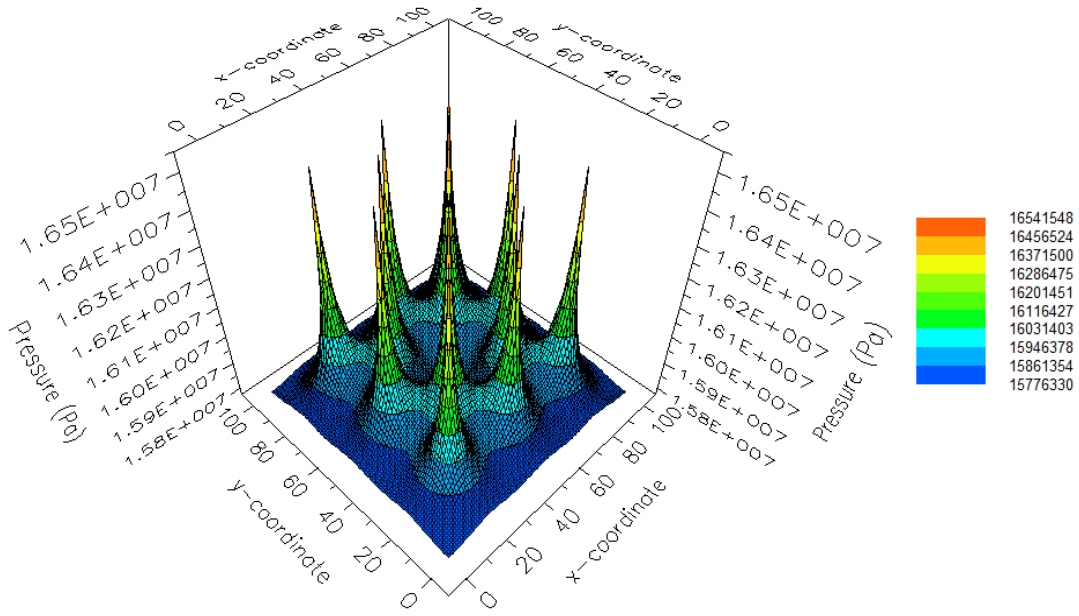

Figure A.9 – Saline Aquifer pressure distribution for t = 2 years

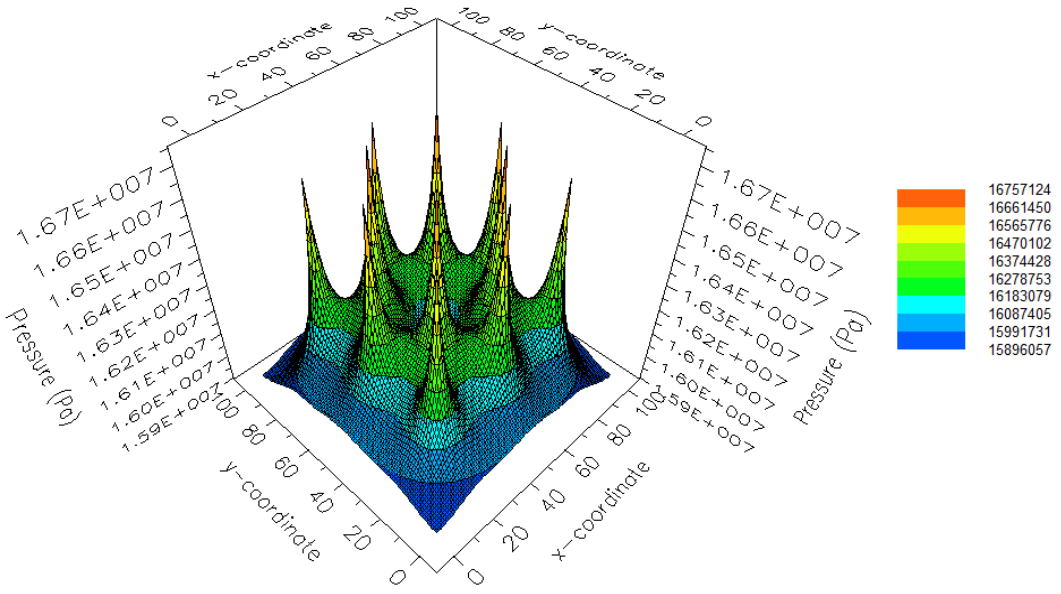

Figure A.10 –Saline aquifer pressure distribution for t = 5 years

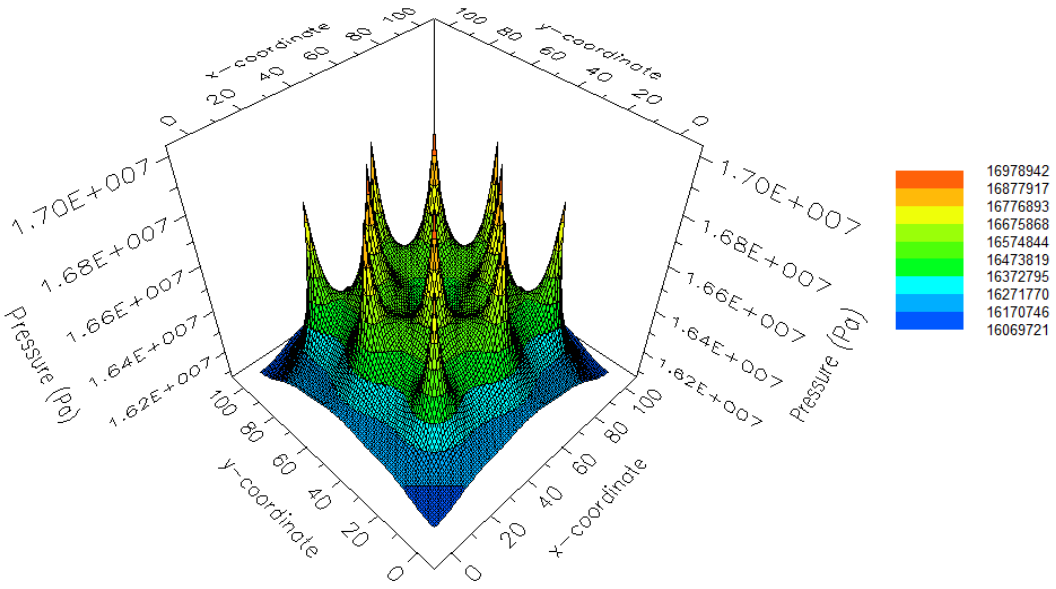

Figure A.11 – Saline aquifer pressure distribution for t = 8 years